Synthesis of α-$Ti(HPO_4)_2 \cdot H_2O$ for the Separation of Radionuclides

Using Barium and Lanthanum as Analogues for Radium and Actinium

J.W. van den Berg

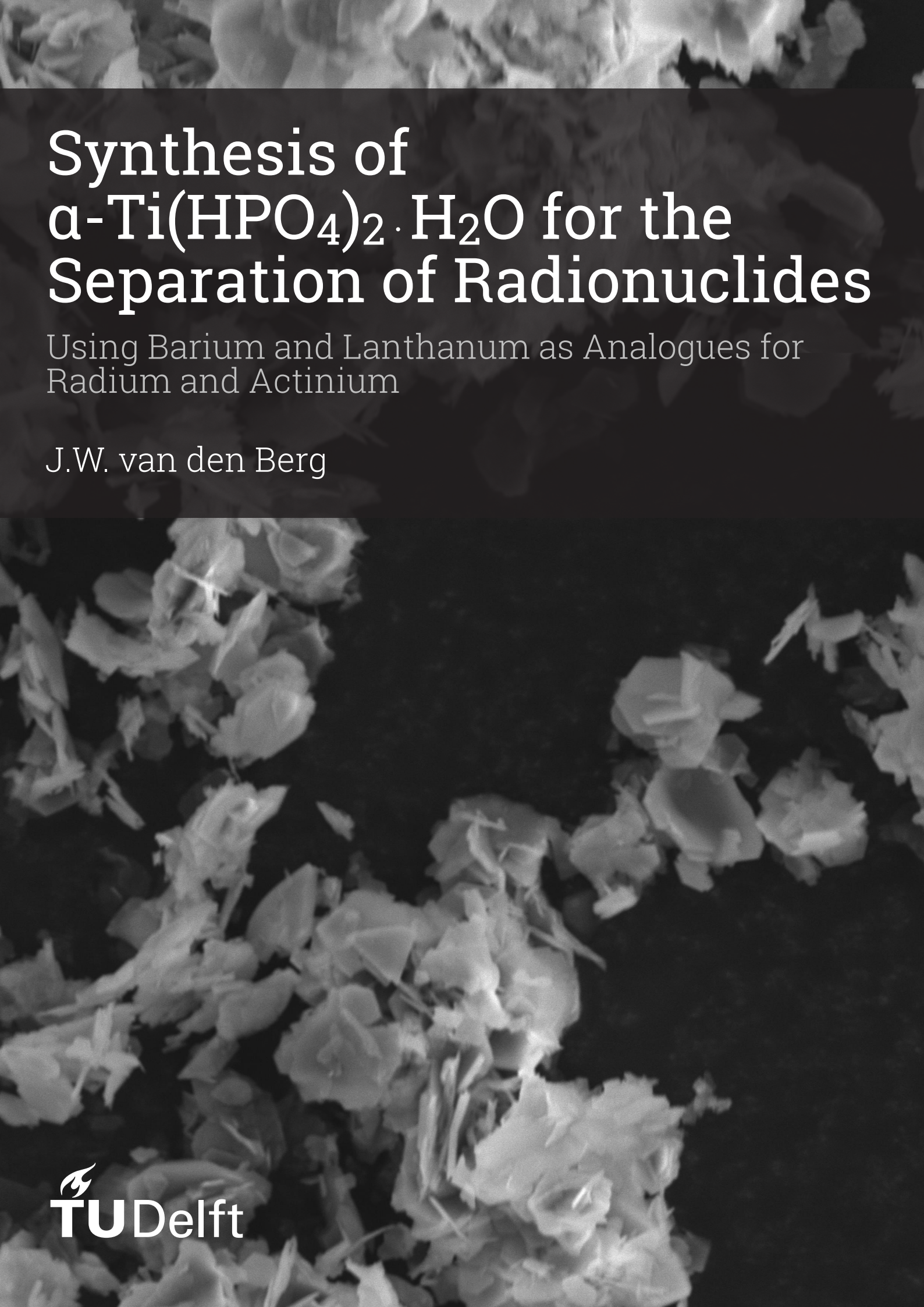

TU Delft

This page has been intentionally left blank.

Synthesis of α-$Ti(HPO_4)_2 \cdot H_2O$ for the Separation of Radionuclides

Using Barium and Lanthanum as Analogues for Radium and Actinium

by

J.W. van den Berg

to obtain the degree of Master of Science
at the Delft University of Technology,
to be defended publicly on Tuesday May 13, 2025 at 10:00 AM.

Master thesis

Author	J.W. (Jaap) van den Berg
Student number	4753801
MSc	Chemical Engineering
Track	Nuclear Chemistry
University	Delft University of Technology
Date defended	May 13, 2025

Thesis committee

	Dr.ir. A.G. Denkova
	Dr.ir. R. Kruijff
	Dr. E. M. Kelder
	Dr.drs.ir. L.J. Bannenberg
Daily supervisor:	PhD candidate E. Spruit

TU Delft

Cover: [**SEM image of synthesised α-$Ti(HPO_4)_2 \cdot H_2O$ crystals.**]

This page has been intentionally left blank.

Preface

This thesis marks the completion of my Master's in Chemical Engineering. Eight years of being a chemistry student have resulted in this project. Years of studying from textbooks and practical days in the lab have come together in this work. Throughout those eight years, it was not always easy, but over the past six months, I have worked on this project with genuine interest and enjoyment.

I would like to sincerely thank Antonia and Robin for their excellent guidance and inspiring insights, which continually challenged me to think deeper. From my bachelor's thesis, to master's courses and now this thesis. You have helped shape my passion for chemistry and given it direction.

I also want to thank Esther for her endless patience during our countless discussions about my ideas and for her way of thinking as a physicist, which has broadened my perspective.

Lastly, I want to thank Boris and Max. We pulled each other through this master's degree.

I had a fantastic time at TU Delft and I could not have wished for a better student experience. Thank you to everyone who made it so memorable.

J.W. van den Berg
Delft, April 2025

Abstract

The medical interest in targeted alpha therapy (TAT) has increased the demand for actinium-225 (^{225}Ac), a promising isotope for cancer treatment. However, the production falls short. One potential route is the generation of ^{225}Ac via proton irradiation of radium-226 (^{226}Ra), introducing the challenge of separating these radionuclides. In this study, lanthanum and barium were used as chemical analogues for actinium and radium, respectively. This study investigates the production and characterisation of α-titanium phosphate (α-$Ti(HPO_4)_2 \cdot H_2O$, α-TiP) and its feasibility for the separation of lanthanum and barium using ion exchange.

Three synthesis methods were used with different titanium precursors: TiO_2, Ti powder and $TiOSO_4$. The resulting α-TiP samples were characterised using X-ray diffraction (XRD), scanning electron microscopy (SEM) and energy-dispersive X-ray spectroscopy (EDS), confirming phase purity but showing morphological differences.

The ion exchange behaviour of α-TiP was found to be closely linked to morphology and exchange site accessibility. Batch adsorption experiments demonstrated that α-TiP exhibits strong selectivity for trivalent lanthanum (La^{3+}) over divalent barium (Ba^{2+}) ions at acidic pH and relevant concentration ([La^{3+}] = 2.5 µM and [Ba^{2+}] = 1.0 mM).

The results support the potential of α-TiP as a viable material for lanthanum–barium separation. However, further studies are required to confirm radiation stability, reversibility of ion uptake and performance in column-based separation systems. Additionally, experiments should validate whether similar separation behaviour will be achieved for actinium and radium separation.

Nomenclature

Abbreviations

Abbreviation	Definition
BET	Brunauer-Emmett-Teller
BSE	Backscattered electrons
CCDC	Cambridge Crystallographic Data Centre
CSD	Cambridge Structural Database
EDS	Energy-dispersive X-ray spectroscopy
FTIR	Fourier Transform Infrared Spectroscopy
ICSD	Inorganic Crystal Structure Database
LET	Linear Energy Transfer
PDF	Powder Diffraction File
RCF	Relative Centrifugal Force
ROI	Region Of Interest
SE	Secondary electrons
SEM	Scanning electron microscope
TAT	Targeted Alpha Therapy
TiP	Titanium phosphate
TRT	Targeted Radionuclide Therapy
XRD	X-ray diffraction
ZrP	Zirconium phosphate

Symbols

Symbol	Definition	Unit
C	Count rate per volume in sample	$\mathrm{CPM/mL}$
C_{stock}	Count rate per volume in stock	$\mathrm{CPM/mL}$
C_{eq}	Equilibrium ion concentration	$\mathrm{mol/L}$
C_0	Initial concentration	$\mathrm{mol/L}$
C_{Ba}	Equilibrium concentration of Ba^{2+}	$\mathrm{mol/L}$
C_{La}	Equilibrium concentration of La^{3+}	$\mathrm{mol/L}$
C_H	Equilibrium concentration of H^+	$\mathrm{mol/L}$
C_M	Equilibrium concentration of ion M	$\mathrm{mol/L}$
d	Interplanar spacing of the crystal lattice	nm or Å
f_b	Back/peak ratio constant for ^{140}La	-
f_t	Tail/peak ratio constant for ^{139}Ba	-
K_D	Partition coefficient	$\mathrm{mL/g}$
K_H	Equilibrium constant for H^+	$\mathrm{L/mol}$
K_{Ba}	Equilibrium constant for Ba^{2+}	$\mathrm{L/mol}$
K_{La}	Equilibrium constant for La^{3+}	$\mathrm{L/mol}$
K_{Lang}	Langmuir equilibrium constant	$\mathrm{L/mol}$
K_M	Equilibrium constant of ion M	$\mathrm{L/mol}$
K_{thermo}	Thermodynamic equilibrium constant	-
m	Mass of the sorbent	g
n	Diffraction order	-
q	Amount of ion adsorbed	$\mathrm{mol/g}$
q_M	Amount of ion M adsorbed	$\mathrm{mol/g}$
q_m	Maximum adsorption capacity / total site capacity	$\mathrm{mol/g}$
R	Gas constant	$8.314\,\mathrm{J/mol\,K}$
R_{Ba}	Detected count rate of ^{139}Ba	CPM
$R_{\mathrm{Ba,\ corrected}}$	Corrected count rate of ^{139}Ba	CPM
R_{La}	Detected count rate of ^{140}La	CPM
$R_{\mathrm{La,\ corrected}}$	Corrected count rate of ^{140}La	CPM
T	Absolute temperature	K
$t_{(1/2)}$	Half-life	time
V	Volume of Ba/La mixture	mL
ΔG	Gibbs free energy change	$\mathrm{J/mol}$
ΔH	Enthalpy change	$\mathrm{J/mol}$
ΔS	Entropy change	$\mathrm{J/mol\,K}$
γ	Detected gamma radiation	-
λ	Wavelength of incident X-rays	nm or Å
θ	Angle of diffraction	$^\circ$ or rad
θ	Fractional coverage	-
θ_M	Fractional coverage of ion M	-

List of Figures

List of Tables

Contents

1 Introduction

Cancer is the second leading cause of death worldwide, with an estimated 19 million new cases and nearly 10 million deaths in 2020, according to the WHO [1]. The global occurrence of cancer continues to rise, driven by population growth, ageing and lifestyle factors [2]. In addition to conventional treatment strategies such as surgery, radiotherapy and chemotherapy, innovative approaches have emerged. While chemotherapy remains an important treatment strategy, its poor selectivity for cancer cells leads to significant side effects [3]. Targeted drug delivery has been developed to improve selectivity, enabling precise drug delivery of therapeutic agents to tumour tissue [4, 5]. This, together with a better understanding of radiobiology and radiation therapy, opens up opportunities for more advanced techniques, including targeted radionuclide therapy (TRT) [6, 7].

TRT is a form of molecular radiation therapy that uses radioactive isotopes bound to tumour-seeking agents. This approach precisely delivers radiation directly to cancer cells and, depending on the agent, can enable prolonged retention of radionuclides at tumour sites. This minimises damage to surrounding healthy tissue [7, 8]. Molecular and functional targets on tumour sites enable radionuclide carriers to deliver alpha, beta and gamma emitters with high specificity towards the tumour site. Gamma emitters are primarily used for imaging purposes and alpha- and beta-emitting radionuclides are used to kill cancer cells [9, 10]. The use of alpha-emitting radionuclides in TRT, known as targeted alpha therapy (TAT), has gained significant attention due to their unique physical properties.

Alpha particles have high linear energy transfer (LET) over a short range (typically 50–100 µm), making them ideal for double-strand DNA breaks within the range of tumour cells while minimising damage to surrounding healthy tissues [11, 12]. Actinium-225 (^{225}Ac) is a promising therapeutic radioisotope for TAT, because of its unique characteristics [13]. First, its emitted alpha particle exhibits a LET of 150 keV per µm and a short range of 40 to 100 µm [11, 14], making it highly effective in killing tumour cells. Second, the half-life of actinium-225 is 9.92 days [15], providing a practical balance between sufficient therapeutic effect and logistical feasibility for manufacturing, transport and clinical applications. Third, its straightforward chelation ability with medical-grade ligands facilitates safe administration to patients. Lastly, its decay chain to stable bismuth-209 includes four more, short-living, alpha-radiating isotopes (^{221}Fr, ^{217}At and ^{213}Po) [14], therefore, actinium-225 is described as a ”nanogenerator” [16]. In addition to its therapeutic potential, using actinium-225 offers imaging possibilities. Gamma energies emitted by ^{221}Fr and ^{213}Bi further in the decay chain can be used for imaging of the biodistribution, further enhancing the suitability of actinium-225 as a good candidate for TAT [13].

Several production routes exist to obtain actinium-225, each with specific advantages and limitations. The most used route in preclinical research and clinical administration is the isolation of actinium-225 from thorium-229 ($t_{(1/2)}$ of 7317 years) sources, generated from the decay of aged uranium-233 ($t_{(1/2)}$ of 160,000 years) [17, 18, 19]. However, the amount of actinium-225 that can be produced from thorium-229 is extremely limited, since the thorium sources are sparse due to the long half-life of uranium-233, confining the yield. As a result, this route can provide treatment for only a few hundred patients annually, creating a need for alternative actinium-225 production methods to meet the worldwide demand [13, 17]. One alternative involves the use of linear electron accelerators, where a radium-226 (^{226}Ra) target is irradiated with high-energy photons to produce radium-225 ($t_{(1/2)}$ of 14.9 days) via the ^{226}Ra(γ, n)^{225}Ra nuclear reaction. The produced radium-225 subsequently decays to actinium-225 [20, 21]. The second alternative method to produce actinium-225 uses cyclotrons to irradiate a radium-226 target with protons, generating actinium-225 through the ^{226}Ra(p, $2n$)^{225}Ac nuclear reaction [18, 22]. Currently,

the latter production method offers distinct advantages, higher production yield efficiency, making it the most promising approach for large-scale actinium-225 production [13, 23].

After actinium-225 is produced according to the ^{226}Ra(p, $2n$)^{225}Ac nuclear reaction or decayed from ^{225}Ra, for clinical use it must be isolated from the radium isotopes. One possible means of separation is using commercially available organic resins in extraction chromatography [22, 24, 25, 26]. Although these resins achieve high recovery yields of over 98% [26], their use is limited in high-radiation environments. Exposure to high-energy alpha radiation from actinium-225 and its daughters degrades the polymeric matrix of organic resins. Consequently, organic resins have limited reusability in high-radiation environments. Furthermore, radiolysis of the organic material leads to organic impurities, affecting the radiolabelling capacity, chelating abilities and decreasing its separation performance [27, 28, 29].

Inorganic metal oxide sorbents, frequently employed in liquid chromatography, offer exceptional radiation stability, thermal resistance and chemical resilience. These properties make them particularly suitable for use in high-radiation environments [27, 30, 31]. In radiochemical applications, inorganic sorbents are valued not only for their robustness but also for their tunable surface properties [32], which enable selective adsorption and ion exchange mechanisms with metal ions. Brown [27] demonstrated that inorganic sorbents such as alumina, titania and zirconia are effective at fractionating barium and lanthanum, which are commonly used as chemical analogues for radium and actinium due to their similar ionic charge and radius [33, 34]. Notably, zirconia was shown to successfully separate radium from actinium under experimental conditions [27].

Building on this foundation, attention has turned to more specialised inorganic sorbents, such as metal phosphates and zirconates. These materials combine the benefits of radiation and chemical stability with strong ion exchange capacities, making them promising candidates for heavy element separations. Among them, titanium phosphates (in this study referred to as TiP) have emerged as a particularly interesting candidate due to its structural versatility and favourable sorption characteristics in aqueous environments [35, 36, 37, 38, 39].

TiP can be synthesised in several forms, amorphous phases, intermediate crystalline phases and fully crystalline structures [40]. While amorphous TiP exhibits high ion exchange capacities, it is less selective for divalent (2+) and trivalent (3+) metal ions and is therefore not of further interest for this study [37, 38, 41, 42]. Crystalline TiP exists in two main phases: $Ti(HPO_4)_2 \cdot H_2O$ (α-TiP) and $Ti(HPO_4)_2 \cdot x\,H_2O$ (where x = 0.8-1.1 [43]), which represents a mixture of $Ti(HPO_4)_2 \cdot 2\,H_2O$ (γ-TiP) and its anhydrous form $Ti(HPO_4)_2$ (β-TiP). The latter phase is quasi-stable and tends to rehydrate when exposed to air [40, 44, 45]. Among these, α-TiP has gained attention due to its structural similarity to α-$Zr(HPO_4)_2 \cdot H_2O$ (zirconium phosphate, α-ZrP) [38, 45]. This structural isomorphism suggests that α-TiP may exhibit comparable adsorptive and ion exchange properties [44, 45]. α-ZrP has been shown to selectively adsorb cations [38, 46] and recent studies indicate similar behaviour for α-TiP [33, 35, 38, 39, 47].

Therefore, the main objective of this research is to investigate if TiP, specifically α-$Ti(HPO_4)_2 \cdot H_2O$ is a suitable material for the separation of radium and actinium.

In fulfilment of the main goal of the research, the first sub-objective is to successfully synthesise and characterise α-$Ti(HPO_4)_2 \cdot H_2O$. To achieve this, three different synthesis methods are employed to prepare α-$Ti(HPO_4)_2 \cdot H_2O$, which is then characterised to evaluate its structural properties. This step is important for understanding its ion exchange behaviour and for evaluating its potential as a selective sorbent for radium and actinium separation.

The second sub-objective of this study is to investigate the separation properties of α-TiP using barium and lanthanum as chemical analogues for radium and actinium. This approach allows for a safe and

practical evaluation of the adsorptive behaviour and separation performance of α-TiP, providing preliminary insight into its potential for the separation of radium and actinium under comparable experimental conditions.

In Chapter 2, the background is provided on the theory used in this research. Furthermore, the principles underlying the apparatuses, analytical techniques and chemical mechanisms are explained. Chapter 3 outlines the methods used to execute the experiments, including the syntheses, chemical preparations and separations. The results obtained from the experiments are presented and discussed in Chapter 4. In Chapter 5, the conclusions are addressed. Finally, the recommendations for further research are outlined in Chapter 6.

2
Theoretical background

The separation and purification of radionuclides is a cornerstone of nuclear science and radiopharmaceutical development [48, 49]. Achieving high-purity separation of radionuclides from complex radiochemical matrices requires a detailed understanding of their chemical behaviour, reaction mechanisms and the properties of suitable sorbents [27, 32].

This study focuses on separating actinium-225 from radium-226 after cyclotron production through the ^{226}Ra$(p, 2n)^{225}$Ac nuclear reaction. Following this reaction, the resulting solution contains both Ac^{3+} and Ra^{2+} ions, which have comparable ionic sizes but differ in charge, hydration and coordination behaviour.

This chapter provides the theoretical foundation for the research presented in this study. Section 2.1 introduces the principles of radionuclide separation, highlighting the challenges posed by chemical similarity of radionuclides, radiolysis and scalability. Elaborating on that, Section 2.2 presents the fundamentals of ion exchange, detailing the mechanisms, kinetics and thermodynamics that dictate binding processes. Furthermore, Section 2.3 focuses on the structural and functional properties of α-TiP. Then, Section 2.4 discusses the use of chemical analogues in this study. Lastly, Section 2.5 describes the analytical techniques used in this study.

2.1. Separation and purification techniques

The separation of analytes from complex matrices enables the isolation of specific radioactive species for various applications. This involves separating activation products from irradiated targets, extracting daughter nuclides in generator systems or removing decay products and other contaminants. Separation can be achieved based on differences in chemical properties, such as ionic charge, size or complexation tendencies of these elements [48, 50, 51].

In medical applications, there is an amplified need for radionuclide purity to ensure safety and therapeutic efficacy. Radionuclides used in diagnostics (imaging) or treatments (targeted therapy) must be free of radiochemical contaminants to avoid unintended radiation exposure or reduced specificity [52, 53]. Impurities, including targets or parent nuclides, can influence targeting mechanisms and lower specific activity by competing with the product radionuclide, influencing patient outcomes. Therefore, purification must meet clinical and regulatory standards [52, 53, 54].

2.1.1. Challenges in radiochemical separation

Radiochemical separation faces challenges due to the similar properties of radionuclides and their processing conditions [48]. These difficulties affect the ability to isolate pure radionuclides, requiring advanced techniques.

One challenge in separating ^{225}Ac from ^{226}Ra is their comparable behaviour in aqueous systems. Both ions preferentially bind to hard oxygen-donor ligands and tend to form high coordination number complexes. This complicates effective separation with conventional ion exchangers. However, differences in charge, charge density and complexation strength between Ac^{3+} and Ra^{2+} can be exploited by specialised materials to achieve successful separation [27, 32, 48].

The short half-life of ^{225}Ac (9.92 days [15]) presents significant logistical and technical challenges for its production and clinical use. Rapid separation following cyclotron irradiation is needed to prevent decay losses, particularly given the trace quantities produced [55]. Delays in processing or transport reduce the final usable activity. Although generator systems can continuously supply short-lived isotopes from long-lived parents and are suitable for on-site deployment, their application to ^{225}Ac is constrained.

Moreover, sorbent stability is critical in the chemical and radiological environments encountered during radionuclide separation. High radiation doses might degrade separation mediums [56]. Organic resins suffer radiolysis, breaking C-C bonds and decreasing separation performance [57]. Inorganic sorbents like metal oxides and phosphates show better resistance to high radiation doses, but crystalline defects from recoil nuclei can decrease selectivity [30, 32, 58]. This degradation demands robust separating materials to maintain efficiency.

Additionally, degradation of the separation medium can release impurities, affecting radiochemical purity. Specific activity can decrease due the release of target material or separation mediums, which dilutes the desired radionuclide [59]. A lower specific activity limits therapeutic efficacy and imaging resolution, as it reduces the number of radioactive atoms per targeting molecule in radiopharmaceuticals [53, 59].

Lastly, scalability in radiochemical separation, such as isolating ^{225}Ac from ^{226}Ra, is constrained by the need for high-throughput systems like continuous-flow chromatography. These require enhanced radiation shielding, efficient radioactive waste management and robust, selective sorbents to maintain purity. Limited infrastructure confines production to specialised facilities, restricting ^{225}Ac availability for radiopharmaceuticals [53, 60].

2.1.2. Overview of separation techniques

Various radiochemical separation techniques exist, each suited to different challenges in isolating radionuclides. The most commonly employed methods include precipitation, liquid–liquid extraction and chromatography [48, 55].

Precipitation and liquid–liquid extraction are widely used in radiochemistry for bulk separations or selective complexation of radionuclides [32, 61]. Precipitation, however, is an inherently batch process that can not be integrated into the compact, shielded, continuous-flow systems required for fast post-irradiation processing of mixed Ac^{3+}/Ra^{2+} solutions. Liquid–liquid extraction, although highly effective with specialised ligands, often suffers from limited radiation stability of the organic phase under high-radiation environments [56, 57]. Consequently, these methods are less suitable for the separation of actinium and radium and are not further discussed in this study.

Instead, this study focuses on chromatographic separation. This method offers high resolution and flexibility, making it suitable for isolating radionuclides with similar chemical characteristics. Chromatographic methods are classified by their separation mechanism: adsorption, partitioning or size exclusion [62]. Ion exchange chromatography, the focus of this study, is an adsorption process in which ions in the mobile phase interact electrostatically with charged functional groups on the stationary phase. Formats such as gravity-fed columns and High-Performance Liquid Chromatography (HPLC) can operate based on ion exchange, depending on the column properties [62, 63].

Size exclusion chromatography separates species by molecular size using porous materials such as gels, zeolites or crystalline frameworks. However, this technique is less effective for separating Ac^{3+} and Ra^{2+} ions, due to their similar ionic and hydrated ionic radii [63]. The overall effectiveness of a chromatographic separation depends on both the chemical selectivity of the separation mechanism and the physical properties of the sorbent.

Given these considerations, the next section explores the principles of ion exchange in more detail, with a focus on the factors influencing selectivity and the suitability of inorganic exchangers for separating multivalent cations.

2.2. Ion exchange

Ion exchange is the driving mechanism of ion exchange chromatography, a specific form of adsorption chromatography. This technique separates radionuclides through reversible electrostatic interactions between dissolved ions and charged functional groups on a solid sorbent [49, 64, 65]. In radiochemical applications, this process is typically implemented in column-based systems using radiation-resistant materials with fixed-charge sites. Ion exchange chromatography is particularly well-suited for separating radionuclides with subtle differences in ionic charge and hydration behaviour, making it relevant for the separation of trivalent actinium from divalent radium ions [27, 32, 57].

This section presents the theoretical basis of ion exchange relevant to this study. In Section 2.2.1, the ion exchange fundamentals are discussed, followed by the mechanisms that govern ion selectivity in Section 2.2.2. Lastly, Section 2.2.3 explores the thermodynamics of the exchange process for describing ion–sorbent interactions.

2.2.1. Fundamentals of ion exchange

Ion exchange involves the reversible exchange of ions between a solid exchanger and a surrounding solution, induced by electrostatic interactions [63, 66]. As introduced in the previous section, the exchanger releases counterions while binding ions of interest based on charge and hydration properties [49, 56, 63]. Selectivity arises from differences in ionic radii, charge density and complexation properties, enabling the separation of radionuclides with similar chemistry [67].

2.2.1.1. Organic ion exchangers

Organic ion exchangers feature covalently bound functional groups that facilitate ion binding [61]. Their high capacity and tunable selectivity make them effective for separating radionuclides, which is also exploited in extraction chromatography [57]. However, their organic backbone is prone to degradation under high radiation environments, reducing its lifespan and potentially introducing impurities [56, 57]. Still, their continued relevance in radiochemical separations is due to their versatility and the relative simplicity of their synthesis.

2.2.1.2. Inorganic ion exchangers

Inorganic ion exchangers, such as metal oxides, phosphates and zeolites, possess crystalline or amorphous structures with defined ion exchange sites [64]. These materials exhibit superior thermal, chemical and radiation stability [27, 30]. This resilience arises from their stable covalent or ionic frameworks, making them ideal for radiochemical applications. The ion exchange behaviour of these materials sometimes exhibits selectivity for specific ions due to their rigid structures and tunable pore sizes [68]. Zeolites feature microporous structures enabling high selectivity for small cations. Metal oxides offer hydroxyl-rich surfaces for exchanging heavy metals. Phosphates, investigated in this study, use acidic hydroxyl (PO – H) groups to form deprotonated PO^- sites, enhancing cation uptake [69]. This structural diversity allows precise control over ion interactions.

2.2.2. Mechanisms of ion exchange

Ion exchange is driven by multiple mechanisms that determine the selectivity and kinetics of ion adsorption. These include electrostatic interactions, coordination bonding and size exclusion, each contributing differently, but often overlapping, depending on the properties of the exchanger [49, 66, 68].

Electrostatic interactions are the primary driving force, where charged ions bind via the Coulomb interaction [49]. Selectivity is largely governed by the charge density of the ions, in which highly charged

and smaller ions interact more strongly due to greater electrostatic forces [67, 69]. In addition to electrostatics, some exchangers allow ions to form coordination bonds with electron-donating groups such as phosphate oxygens or interlayer water [35]. These involve partial electron sharing, stabilising the bound ion and increasing the activation energy for exchange. Strong coordination, especially with trivalent ions, may result in slower kinetics due to more stable complexes, whereas weaker coordination with divalent ions enables faster exchange [70]. Size exclusion limits ion access based on size and hydration. Porous and layered materials such as zeolites and phosphates introduce steric constraints that favour smaller or less-hydrated ions [35, 39, 64]. This effect enhances selectivity by physically excluding larger ion species.

2.2.2.1. Kinetics of ion exchange

Ion exchange kinetics govern the rate of ion uptake, influenced by binding mechanisms and exchanger properties [66]. Electrostatic interactions drive rapid initial exchange, while coordination bonding can slow rates by forming stable complexes, particularly in crystalline materials [49]. For the separation purposes in this study, rapid exchange kinetics are needed, with factors such as exchanger site accessibility and pH affecting adsorption rates [60]. Since slow exchange can significantly reduce separation yields in column-based systems, optimising kinetics is a critical design consideration.

2.2.3. Thermodynamics of ion exchange

The thermodynamics of ion exchange determines the equilibrium and spontaneity of cation uptake on sorbents [66, 71]. Ion exchange is thermodynamically driven by the balance between enthalpy (ΔH), entropy (ΔS) and Gibbs free energy (ΔG) [50, 66, 71]. Since the experiments in this study are conducted under isothermal conditions, Equation 2.1 can be applied directly to describe the equilibrium of the ion exchange reaction:

$$\Delta G = \Delta H - T\Delta S = -RT \ln K_{thermo} \tag{2.1}$$

Where:

- ΔG is the Gibbs free energy change [J/mol],
- ΔH is the enthalpy change [J/mol],
- T is the absolute temperature [K],
- ΔS is the entropy change [J/mol K],
- R is the gas constant (8.314 J/mol K),
- K_{thermo} is the thermodynamic equilibrium constant [-].

The signs of ΔG, ΔH and ΔS provide insight into the spontaneity and driving forces thermodynamic systems [71]. A negative ΔG indicates spontaneous exchange, meaning the exchange of cations is thermodynamically favourable under the given conditions. A positive ΔG, conversely, suggests a non-spontaneous process requiring external energy input [72].

ΔH represents the enthalpy change associated with the ion exchange process and reflects the strength of interactions between the ions and the sorbent. A negative ΔH indicates exothermic binding, typically due to strong electrostatic or coordination interactions. In contrast, a positive ΔH suggests an endothermic process, which stems from breaking hydration shells and deprotonating surface sites. While a positive ΔH implies energy input is required, overall spontaneity depends on the balance of enthalpy and entropy contributions [72].

ΔS represents entropy and measures disorder. A positive ΔS occurs when the system becomes more disordered, such as when hydrated ions release water molecules upon binding [72, 73]. Negative ΔS reflects a more ordered state, reducing spontaneity [71].

The thermodynamic equilibrium constant K_{thermo} quantifies the ratio of product to reactant activities at equilibrium. In ion exchange, it reflects the relative affinity of the sorbent for competing ions. A larger K_{thermo} indicates a greater preference for the sorbent to retain the incoming ion, resulting in a more effective exchange. Thermodynamically, K_{thermo} is linked to ΔG, since a high K_{thermo} corresponds to a more negative ΔG, indicating a more spontaneous and thermodynamically favourable ion exchange process.

2.3. α-TiP

Titanium phosphates are a well-known class of inorganic ion exchangers, valued for their radiochemical and thermal stability and selective adsorption capabilities [35, 37, 64, 69]. Among them, α-TiP has attracted particular interest due to its crystalline layered structure, described in Section 2.3.1 and associated ion exchange mechanism, explained in Section 2.3.2.

2.3.1. Crystal structure of α-TiP

α-TiP is a layered tetravalent metal phosphate that has been extensively studied for its structural properties and potential applications [40, 44, 45]. These publications include a detailed structural characterisation using X-ray powder diffraction and establish that α-TiP is isostructural with α-ZrP, as summarised in Table 2.1.

α-TiP has a P_{2_1}/c space group, in which titanium atoms are octahedrally coordinated by six oxygen atoms. These oxygen atoms are sourced from distinct tetrahedral phosphate groups. The octahedra form a two-dimensional network, creating an ab-plane that stacks along the crystallographic c-axis. The phosphate groups are tetrahedral units, with three oxygen atoms bridging to titanium atoms and one oxygen bonded to a hydrogen atom, forming a hydroxyl group. This arrangement results in a layered structure where the titanium-oxygen octahedra and phosphate tetrahedra are linked within the plane, stabilised by a combination of ionic and covalent interactions [40, 44, 45].

Table 2.1: Unit cell parameters and space group for α-TiP and α-ZrP [39, 44, 45].

Material	**a** (Å)	**b** (Å)	**c** (Å)	β (°)	**Space group**	**Interlayer distance** (Å)
α-TiP	8.630(2)	5.006(1)	16.189(3)	110.20(1)	P_{2_1}/c	7.58
α-ZrP	9.062(1)	5.288(1)	16.255(2)	111.38(1)	P_{2_1}/c	7.6

The orientation of these molecular units within the layers is highly ordered [45]. The TiO_6 octahedra are positioned such that their equatorial planes lie approximately parallel to the ab-plane. At the same time, the axial oxygen atoms connect to adjacent phosphate groups, reinforcing the planar framework. The hydrogen atoms of the hydroxyl groups project outward from the layers, contributing to the ion exchange capabilities of α-TiP on the surface and in the interlayers [44, 45, 69].

The layered nature of α-TiP results in interlayer spaces between the planes, a feature influencing its physical and chemical properties. Titanium phosphate sheets along the crystallographic c-axis, are stabilised by water molecules (one per formula unit), occupying the region between the layers. Additionally, these water molecules maintain the interlayer distance between adjacent layers [40, 45, 74]. The structure is illustrated by Amghouz et al. [44] along the a-axis and b-axis in Figure 2.1 and Figure 2.2 respectively.

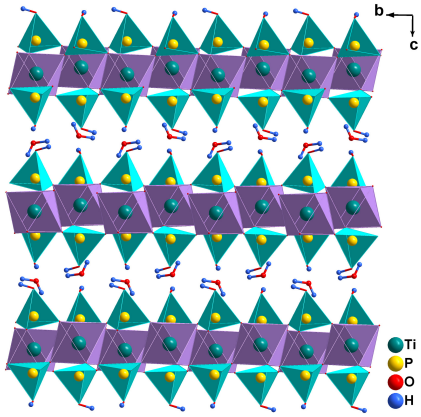

Figure 2.1: Projection of the structure of α-TiP along the a-axis [44].

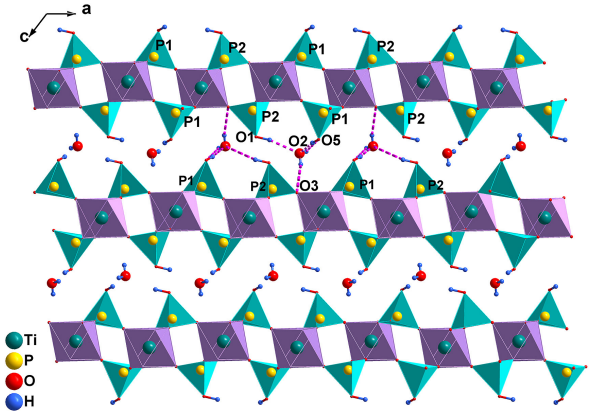

Figure 2.2: Projection of the structure of α-TiP along the b-axis [44].

2.3.2. Ion exchange mechanism of α-TiP

The competitive adsorptive behaviour of α-TiP for divalent, trivalent and tetravalent ions is comprehensively studied in literature [35, 39, 40]. The selective adsorption behaviour arises from its capacity to bind cations in aqueous solutions through deprotonated hydroxyl groups on its layered crystalline structure. In contrast to the amorphous titanium phosphates [37], the crystallinity of α-TiP provides a consistent structural basis for selective adsorption. As introduced in Section 2.2.2, this section delves into the ion exchange mechanism of α-TiP, as electrostatic interactions, coordination bonding and size exclusion facilitate selective cation uptake.

2.3.2.1. Electrostatic interactions

The adsorption behaviour of α-TiP relies on electrostatic interactions, a mechanism driven by the deprotonation of its hydroxyl groups, releasing H^+ ions and generating PO^- sites. These negatively charged oxygen atoms attract cations through electrostatic forces. The degree of deprotonation, however, is pH-dependent, with increased formation of deprotonated hydroxyl groups at higher pH values, enhancing the negative charge density of the material. The adsorption follows the law of chemical equilibrium, with uptake increasing as metal ion concentration rises. This behaviour reflects a typical mass-action driven equilibrium, where increased cation concentration favours displacement of protons and enhances site occupation [35]. The process is inherently linked to ion exchange, where incoming cations displace the protons initially bound to the phosphate groups, effectively swapping positions in a stoichiometric balanced substitution, as shown in Equation 2.2:

$$\mathrm{RH}_n + \mathrm{M}^{n+} \longrightarrow \mathrm{RM} + \mathrm{nH}^+ \tag{2.2}$$

The selectivity sequences reported by several studies [35, 37, 69] reflect the increasing affinity of ions with higher charge-to-radius ratios. Higher-charge trivalent ions exhibit stronger electrostatic affinity due to their intensified attraction to PO^- over divalent ions. This mechanism provides α-TiP with relevant selective ion exchange capacities for the separation of Ra^{2+} and Ac^{3+}.

2.3.2.2. Size exclusion

In α-TiP, size exclusion imposes an additional layer of control over adsorption, dictated by the fixed interlayer spacing of approximately 7.6 Å [44]. This structural constraint regulates which cations can access the interlayer region, influencing both the efficiency and selectivity of uptake. Smaller or less hydrated ions more readily penetrate the space, whereas larger ions or those with larger hydration shells encounter resistance, reducing their adsorption.

The selectivity order of α-TiP, reflect trends in ionic radii and hydration energies. As cations enter the interlayer to replace H^+, their size and hydration shell determine accessibility to the PO^- sites, but experience steric hindrance that reduces accessibility. This mechanism complements electrostatic and coordination interactions [35, 39, 40]. In contrast, the amorphous TiP lacks such defined spacing, resulting in less consistent size-based selectivity [37]. For α-TiP, size exclusion ensures that adsorption is not solely a function of charge or coordination but also of spatial compatibility with the crystalline lattice.

2.4. Chemical analogues

Studying the separation behaviour of radionuclides such as actinium (Ac^{3+}) and radium (Ra^{2+}) presents considerable challenges due to their limited availability, high cost and the radiological precautions required for handling. Therefore, lanthanum (La^{3+}) and barium (Ba^{2+}) are used as chemical analogues. These analogues possess similar ionic charges, comparable ionic radii and closely related coordination chemistries to actinium and radium, respectively (Table 2.2) [27, 38]. Additionally, they are safer to handle, more readily available at the reactor facility where the experiments were conducted and more cost-effective. This section explores these analogues, focusing on their relevance to ion exchange mechanisms in α-TiP and their chemical properties that facilitate the study of Ra/Ac separations.

2.4.1. Lanthanides and actinides

Lanthanides and actinides are elements with unfilled f-orbitals, characterised by high charge densities and a strong preference for coordination with hard donor atoms such as oxygen. La^{3+}, is commonly used as an analogue for Ac^{3+} due to their identical oxidation state and similar ionic radii and hydration behaviour in aqueous media (Table 2.2). These similarities make La^{3+} a practical and accessible substitute for evaluating ion exchange behaviour of α-TiP.

Although both ions are trivalent hard acids, Ac^{3+} and La^{3+} exhibit subtle structural differences. Relativistic contractions of the 6s/6p and 6d orbitals of actinium slightly decreases its ionic radius. In aqueous solution, this contraction is balanced by hydration, so the effective hydrated radius of Ac^{3+} is similar to that of La^{3+} (Table 2.2). Consequently, both cations should access surface hydroxyl groups on TiP without steric discrimination. Any variations in adsorption kinetics or affinity will therefore stem from small differences charge density and water-exchange dynamics.

2.4.2. Alkaline earth metals

Alkaline earth metals, such as barium and radium, are divalent cations in solution with relatively large ionic radii and low charge densities compared to trivalent lanthanides and actinides. Ba^{2+} is widely used as a chemical analogue for Ra^{2+} due to their similar charge and coordination chemistry, as well as their comparable ionic radii, as shown in Table 2.2. This similarity enables Ba^{2+} to replicate many of the interactions that radium would exhibit in ion exchange.

Despite these similarities, the position of radium lower in Group 2 leads to a slightly larger ionic radius and lower charge density, which can marginally reduce its binding affinity to hard oxygen donor ligands in aqueous systems [50]. These subtle differences influence the thermodynamics and kinetics of adsorption, particularly under conditions of competition or saturation. Nevertheless, in neutral to mildly acidic environments Ba^{2+} has been shown to exhibit aqueous behaviour closely resembling that of Ra^{2+}. As such, it serves as a valid and practical surrogate for initial experimental optimisation.

Table 2.2: Ionic and hydrated ionic radii and coordination numbers of Ba^{2+}, Ra^{2+}, La^{3+} and Ac^{3+} [70, 73, 75, 76, 77, 78].

Ion	**Ionic radius** (Å)	**Hydrated ionic radius** (Å)	**Coordination number**
Ba^{2+}	1.38	4.0 - 4.4	7 - 9
Ra^{2+}	1.48 (estimated)	4.3 – 4.6 (estimated)	8 - 9
La^{3+}	1.16	4.1 – 4.3	8 - 9
Ac^{3+}	1.12 (estimated)	4.3 - 4.5 (estimated)	9 - 10

While La^{3+} and Ba^{2+} serve as practical and chemically justified analogues for Ac^{3+} and Ra^{2+}, respectively, their use does not fully replicate the chemical behaviour of the radionuclides they represent. Therefore, complementary experiments using ^{226}Ra and trace quantities of ^{225}Ac remain essential.

2.5. Measurement devices

The characterisation of α-TiP and its ion exchange properties relies on specialised measurement devices to assess structural, compositional and adsorptive behaviour. This section introduces three key devices used in this study: the Wallac Wizard2 Gamma Counter (Wallac gamma counter, Wallac) for quantifying radionuclide adsorption, Scanning Electron Microscopy (SEM) for examining crystal morphology, Energy-dispersive X-ray spectroscopy (EDS) for elemental distribution and X-ray Diffraction (XRD) for determining crystallographic structure.

2.5.1. Wallac gamma counter

The Wallac is a well-type scintillation detector designed to measure the decay of gamma-emitting nuclides in a sample. It uses a sodium iodide (NaI(Tl)) scintillation detector, which converts absorbed gamma radiation into visible light. When a gamma photon interacts with the scintillator, it excites atoms within the crystal. As these atoms return to their ground state, they emit photons of visible light, which are detected by a photomultiplier tube (PMT). The PMT amplifies the signal and converts it into an electrical pulse, where the voltage is proportional to the energy of the absorbed gamma photon. The gamma spectrum is then constructed by counting individual pulses.

The Wallac gamma counter presents measurements in counts per minute (CPM), integrated over a predefined region of interest (ROI) that corresponds to the peak energy range of a specific nuclide. Due to its poor spectral resolution, the Wallac is mostly used for quantitative rather than qualitative analysis. When multiple nuclides are present, their gamma photon energies must be sufficiently different to avoid overlap.

The well-type geometry of the detector provides high counting efficiency by ensuring that the sample is surrounded by the scintillator, maximising detection probability. This geometry reduces variations caused by sample positioning, making measurements more reliable. However, variations in sample volume can influence the count rate, as changes in geometry affect the distance between radioactive material and the detector. Research by Spruit [38] showed that increasing the sample volume slightly decreases the count rate, but the effect is minimal for small variations.

2.5.2. Scanning electron microscope

Scanning Electron Microscopy (SEM) is a technique used to obtain high-resolution images of the surface of a sample, providing information about its morphology and size [44]. It operates by directing a highly focused electron beam, generated by an electron gun at the top of the microscope column, onto the sample. The beam is attracted by a positive anode and condensed through a series of electromagnetic lenses to regulate its size and intensity. The scanning coils deflect the beam along the x- and y-axes in a raster pattern, enabling a detailed surface scan.

When the electron beam interacts with the sample, various signals are generated, including secondary electrons (SE), backscattered electrons (BSE) and X-rays. SEs originate from shallow depths and are mostly used for surface imaging, offering high-resolution information on surface topography and morphology. BSEs, on the other hand, are high-energy electrons reflected from deeper within the sample and are primarily used to distinguish compositional differences. Because the yield of BSEs increases with atomic number, regions containing heavier elements appear brighter, providing contrast based on elemental composition. These electron signals are detected by specialised detectors and converted into detailed greyscale images of the sample surface.

In addition to imaging, SEM can be coupled with Energy-Dispersive X-ray Spectroscopy (EDS) to analyse the elemental composition of a sample. EDS uses the characteristic X-rays emitted when incident electrons eject inner-shell electrons from atoms in the sample. As the atoms return to their ground state, they release photons with element-specific energies. By detecting and analysing these X-ray emissions, EDS provides an elemental mapping of the sample, providing data for compositional analysis.

2.5.3. X-ray Diffraction

X-ray diffraction (XRD) is a widely used analytical technique to study the crystallographic structure of materials. It relies on the interaction between incident X-rays and the periodic atomic arrangement within a crystalline sample. When X-rays strike a material, they are scattered by the electrons in the atoms, producing constructive and destructive interference patterns. This phenomenon follows Bragg's law, given by:

$$n\lambda = 2d\sin\theta \tag{2.3}$$

Where:

- n is the diffraction order [-],
- λ is the wavelength of the incident X-rays [nm or Å],
- d is the interplanar spacing of the crystal lattice [nm or Å],
- θ is the angle of diffraction [° or rad].

By analysing the diffraction pattern, the distance between atomic planes can be determined, allowing for phase identification and structural characterisation.

A schematic of this principle is shown in Figure 2.3, showing how an incident X-ray beam interacts with a crystalline material, leading to diffraction at specific angles.

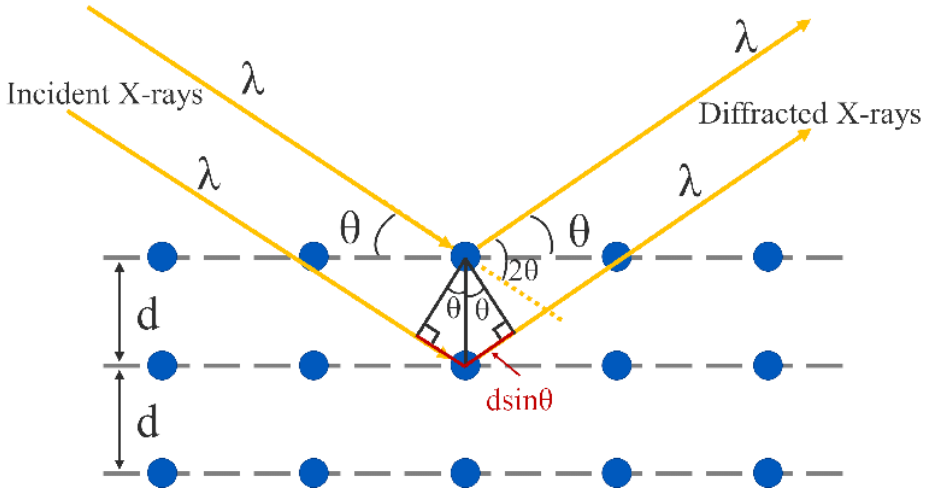

Figure 2.3: Principle of X-ray diffraction: schematic geometry illustrating Bragg's law (λ, θ, d) [79].

2.5.3.1. Diffraction patters

The diffraction pattern of a material consists of a series of peaks that correspond to the diffraction angles where constructive interference occurs. These peaks represent the specific atomic planes within the crystal structure and therefore serve as a crystallographic fingerprint. The relative intensities of these peaks are influenced by factors such as the arrangement of atoms, the electron density and the presence of defects within the lattice. In powder XRD, the sample consists of many crystallites in random orientations, so the resulting pattern captures reflections from all crystallographic planes present in the material [80].

The width of the diffraction peaks is also significant. As described by the Scherrer equation, nanosized crystallites exhibit peak broadening due to their reduced repeating length. This broadening is a result of the limited number of atomic planes contributing to diffraction at any given angle. Moreover, nanoscale materials often have a high surface-to-volume ratio and lattice imperfections, which further contribute to peak broadening [80].

3 Methods

This chapter outlines the experimental procedures used for the synthesis and characterisation of α-TiP, the adsorption experiment and the associated equilibrium and competition experiments. In Section 3.2, the applied three syntheses of α-TiP are explained, together with the product characterisation in Section 3.3. Additionally, Section 3.4 describes the adsorption experiments and all the experiments to substantiate these.

3.1. Materials

In Table 3.1, the chemicals used in this study are presented with their chemical formula and the supplier from which they were purchased. Similarly, in Table 3.2, the apparatus and their manufacturer used in this study are presented.

Table 3.1: Specification of the used chemicals in this study.

Product name	**Chemical formula**	**Supplier**
Barium nitrate	$Ba(NO_3)_2$	Thermo Fisher Scientific
Hydrochloric acid, $\geq$ 37%	HCl	Merck Sigma
Lanthanum nitrate hexahydrate	$La(NO_3)_3 \cdot 6\,H_2O$	Merck Sigma
MilliQ water	H_2O	Ultrapure water system, Advantage A10, Merck
Nitric acid, 65%	HNO_3	Honeywell
Phosphoric acid, 85%	H_3PO_4	Technic
Titanium, 325 mesh, $\geq$ 99%	Ti	Alfa
Titanium(IV)oxide, anastase, 325 mesh, 99%	TiO_2	Merck Sigma
Titanium(IV) oxide sulfate sulfuric acid hydrate	$TiOSO_4xH_2SO_4yH_2O$	VWR (Avantor) International BV
Sulfuric acid, 95-98%	H_2SO_4	Merck Sigma

Table 3.2: Specification of the used apparatus in this study.

Device	Product name	Manufacturer
Ballance	Semi-Micro Analytical balance GR-202	A&D instruments LTD.
Carousel	-	-
Centrifuge	Mega Star 600R	VWR
Centrifuge	Micro Star 17R microcentrifuge	VWR
pH electrode	LE422 Micro	VWR
pH meter	F20/FiveEasy	VWR
Pipette	Physocare concept Pipette 100–1000 µL	Eppendorf
Pipette	Pipette 100–5000 µL	Gilson
Pipette	Proline Single Channel Pipette 2–20 µL	BIOHIT
Pipette	Proline Single Channel Pipette 100–1000 µL	BIOHIT
Rotor centrifuge	TX-150 swing-out	VWR
Scanning electron microscope	JSM-IT1000	JEOL
Vacuum oven	VT 6025 VACUtherm vacuum oven	Thermo scientific
Vortex shaker	Vibrofix VF1	Janke & Kunkel GmbH
Wallac gamma counter	2480 Wallac Wizard2 Automatic Gamma Counter	PerkinElmer
X-ray diffractometer	X'Pert Pro MPD TTK-450	Malvern PANalytical

3.2. TiP syntheses

TiP was synthesised using three different titanium precursors. TiO_2, Ti powder and $TiOSO_4$ were used in Section 3.2.1, Section 3.2.2 and Section 3.2.3 respectively.

3.2.1. Method I: Titanium oxide source

Titanium oxide was used as the precursor for titanium to synthesise TiP in method I. First, 2 g of TiO_2 was added to 50 mL phosphoric acid (85%) in a conical flask at room temperature. The mixture was then heated to 100°C and refluxed for 24 hours, with continuous stirring at 200 revolutions per minute (rpm). After 24 hours, an additional 30 mL of MilliQ water was added to the mixture, which was refluxed for 72 hours more at 100°C. After this reflux, the mixture was naturally cooled to ambient temperature. The product was filtered using a vacuum filter with pore size 4 (10-16 µm) and washed with MilliQ water until the filtrate had a neutral pH (6-7). The product was dried in an oven of 50°C for 5 hours [81]. The material synthesised according to this method are referred to as TiP-I.

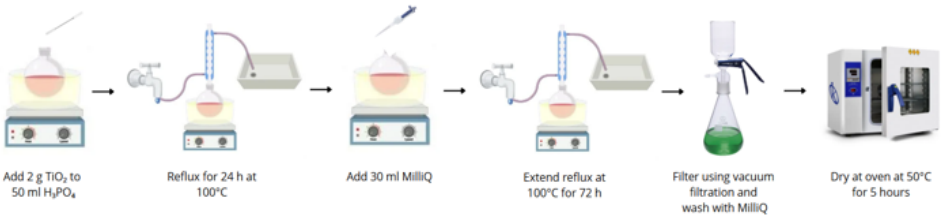

Figure 3.1: Stepwise preparation schemes for method I.

3.2.2. Method II: Titanium metal source

Method II used titanium metal powder as a titanium precursor for the synthesis of TiP. First, 20 mL of phosphoric acid (85%) was preheated in a reflux setup of 100°C, with continuous stirring at 200 rpm in a conical flask. Upon adding 0.5 g of titanium metal to the phosphoric acid, the solution turned purple within 30 minutes. After the solution turned purple, it was refluxed at 100°C for 24 hours. After this reflux, the mixture was naturally cooled to ambient temperature. The obtained product was separated using a vacuum filter with filtration paper (pore size 20-25 µm). The material was washed with MilliQ water until the filtrate had a neutral pH (6-7) and dried in an oven at 50°C for 5 hours [82, 83]. Additionally, some of the product was left to air dry overnight to evaluate the feasibility of air drying as an alternative to oven drying. The material synthesised according to this method is referred to as TiP-II.

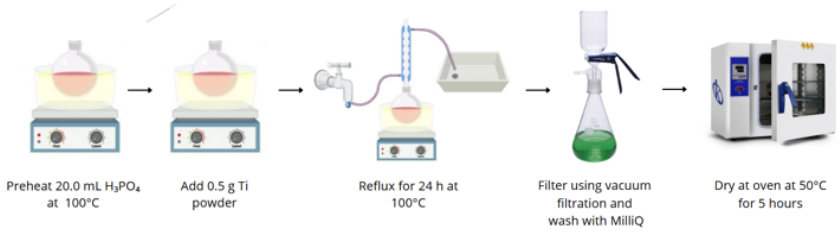

Figure 3.2: Stepwise preparation schemes for method II.

This experiment was also conducted under varying conditions, including different concentrations, temperatures and reflux durations, in order to investigate their influence on the final material properties.

3.2.3. Method III: Titanyl sulfate source

In method III, titanyl sulfate (Titanium oxide sulfate, $TiOSO_4$) was used as the titanium precursor, containing 79.3% titanium(IV) oxide sulfate (sulfuric acid hydrate), 9.7% sulfuric acid and 11.0% moisture. 5.2 g of this powder was dissolved in 5 mL of, at 80°C preheated, concentrated H_2SO_4, with continuous stirring at 200 rpm. This mixture was refluxed for 60 minutes at 80°C in a conical flask, until the powder was fully dissolved. After this, 25 mL of MilliQ water was added. Then, 0.74, 0.88, 4.20, or 17.45 mL of phosphoric acid (85%) was gradually added dropwise to achieve 1:0.42, 1:0.5, 1:2.4 or 1:10 Ti to H_2PO_4 ratio. The mixtures were stirred for 60 minutes at 80°C, followed by 5 hours of stirring at ambient temperature. The product was left to mature for at least 12 more hours and separated using a vacuum filter with pore size 4. Subsequently, the product was washed with 50 mL of 0.5 M HCl, followed by five washes of 50 mL 0.1 M HCl to remove residual sulfuric acid. MilliQ water was then used to wash until the pH of the filtrate reached neutral pH (6-7) [84, 85, 86]. The material synthesised according to this method are referred to as TiP-III-[ratio], e.g., TiP-III-1:10.

For the TiP-III-1:2.4 and TiP-III-1:10 material, an alternative washing protocol was employed to speed up the washing process. The mixture containing the product was divided into 50 mL sample vials and centrifuged using a swing-out rotor at a relative centrifugal force (RCF) of 3000 g for 30 minutes at ambient temperature. The supernatant was pipetted off after each centrifugation cycle, replaced with MilliQ water (30 mL) and mixed using a vortex shaker (2500 rpm for 10 seconds) before being centrifuged again. This process was repeated until the supernatant reached a neutral pH. Finally, the obtained white product was dried in an oven at 50°C for 10 hours.

The TiP-III material (except for the TiP-III-1:0.5) was, after characterisation, reprocessed similar to the reflux of method I (Section 3.2.1) by refluxing 3 g with an excess of 50 mL of phosphoric acid (85%) for 24 hours at 100°C. Thereafter, 30 mL of MilliQ water was added and refluxed for an additional 72 hours. All these products were washed using the alternative washing protocol using the centrifuge. Subsequently, the products were dried in an oven of 50°C for 10 hours. The materials synthesised using this extended reflux method are further referred to as TiP-III-[ratio]-ex.

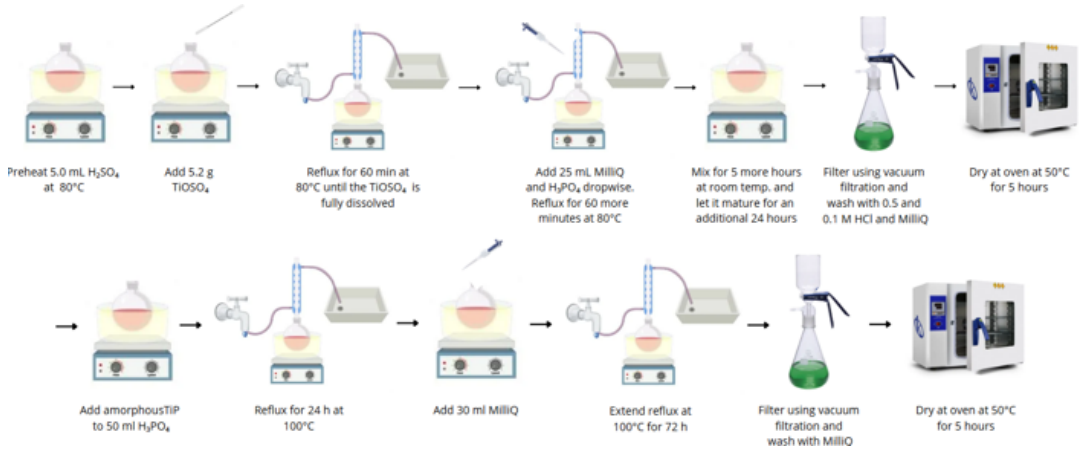

Figure 3.3: Stepwise preparation schemes for method III.

3.3. Characterisation

The synthesised titanium phosphate materials were characterised using several techniques to assess their crystallinity, phase purity, morphology and elemental composition.

3.3.1. XRD analysis

An XRD pattern of all samples was recorded on an X'Pert diffractometer with Cu-Kα radiation (λ = 1.5406 Å) at room temperature. The analysis was done over an angular 2θ range of 5–75° with a scan speed of 1.16° per minute at a voltage of 45 kV and a current of 40 mA. The sample was rotated at 15 rpm (4 seconds per full revolution) to ensure uniform exposure.

The obtained diffractograms were compared without offset to reference data from Amghouz [44], sourced from the Cambridge Structural Database (CSD) and the Inorganic Crystal Structure Database (ICSD) provided by CCDC [87]. The database identifier is ICSD 127963 with deposition number 2124760.

Using X'Pert HighScore [88] software, the results are compared to the powder diffraction file (PDF) of Bruque (PDF: 04-010-3375) [81], stored in the ICDD 2025 database [89]. The peaks reported by Bruque were removed from the diffractogram and the leftover peaks are once more compared to the ICDD 2025 database to determine contaminating substances.

3.3.2. SEM analysis and EDS mapping

Scanning electron microscopy (SEM) micrographs and energy-dispersive X-ray spectroscopy (EDS) were recorded using a JSM-IT1000 scanning electron microscope.

A small amount of each sample was mounted on double-sided carbon tape and imaged at an accelerating voltage of 10 kV. SEM imaging was used to analyse the morphology of the synthesised materials. From the micrographs, the crystallite shape was examined to identify whether the structure was well-structured (plate-like) or amorphous. Additionally, the SEM images were used to assess the size distribution of the particles, allowing for the distinction between a homogeneous and a heterogeneous size distribution. Based on visual inspection and image scaling, a rough estimate of the average particle size was made.

Elemental analysis was performed via EDS to qualitatively and quantitatively assess the elemental composition and distribution throughout the sample. This technique was used to confirm the uniformity and purity of the element. The quantitative results are compared against the calculated values of TiP_2O_9, since hydrogen atoms are not detected by the apparatus.

3.4. Adsorption experiments

Adsorption experiments were conducted to determine the adsorption behaviour and partition coefficients of TiP materials across a pH range of 1 to 7. The materials used in these experiments included TiP-I, TiP-II, TiP-III-1:0.42-ex, TiP-III-1:2.4, TiP-III-1:2.4-ex and TiP-III-1:10-ex. All adsorption experiments were conducted in triplicate.

First, 0.05 g of each material was placed into 1.5 mL vials. To each vial, 1 mL of the Ba/La mixture, as prepared according to Section 3.4.1, was added. The mixture was vortexed for 5 seconds to ensure the dispersion of the sorbent. Subsequently, the vials were placed in a carousel shaker for approximately 5 hours, promoting the ion exchange process. After the reaction time, the activity in the individual vials was measured for 1 minute using a Wallac gamma counter. The time between vortexing and this moment was considered as exchange time, including the measurement time in the Wallac. Thereafter, the vials were centrifuged at 17,000 RCF for 5 minutes to separate the solid and liquid phases. The supernatant was pipetted off and transferred to a second vial. This second vial was centrifuged again to ensure any residual sorbent in the supernatant was sedimented. A final fraction of 0.75 mL of supernatant was pipetted into a third vial for analysis using the Wallac, according to Section 3.4.3. One month after the experiments, when the radioactive isotopes had decayed, the pH of the stock and the samples were measured with a pH electrode, which was calibrated with standardised pH buffers of pH 2, 4 and 7.

3.4.1. Preparing Ba and La mixture

To simulate the radiochemical conditions of a ^{226}Ra/^{225}Ac generator system, a surrogate mixture of Ba^{2+} and La^{3+} was prepared for use in the adsorption experiments. ^{139}Ba and ^{140}La were used to represent ^{226}Ra and ^{225}Ac, respectively.

The concentration of barium was based on the theoretical dissolution of 10 mg ^{226}Ra in a 30 mL solution, corresponding to approximately 1.5 mM. The weighed $Ba(NO_3)_2$, irradiated as described in Section 3.4.2, was dissolved in MilliQ water adjusted to the target pH (1–7) using nitric acid.

The lanthanum concentration was calculated to reflect a ^{225}Ac activity of 1 Ci in 30 mL, equivalent to 2.5 µM. A separate La^{3+} solution was prepared by dissolving 1–2 mg of $La(NO_3)_3 \cdot 6\,H_2O$ in MilliQ water to reach this concentration. An aliquot of this solution was then added to the Ba^{2+} stock to achieve the final Ba/La mixture used in the experiments [27, 38].

3.4.2. Irradiation experiments

Two different irradiation procedures were carried out to make the Ba/La mixture. The irradiation experiments were carried out at the Reactor Institute Delft (RID) in the pneumatic irradiation facility BP3. The facility typically operates at 2.3 MW. At this power, the neutron fluxes presented in Table 3.3 are generated. $Ba(NO_3)_2$ was irradiated for 30 minutes and $La(NO_3)_3 \cdot 6\,H_2O$ was irradiated for 3 hours [38].

Table 3.3: Neutron fluxes of the BP3 pneumatic system of the RID operating at 2.3 MW [90]

Neutron type	Neutron flux
Thermal neutrons (0-0.5 eV)	5 * $10^{12}\mathrm{cm}^{-2}\mathrm{s}^{-1}$
Epithermal neutrons (0.5 eV-1 keV)	1 * $10^{12}\mathrm{cm}^{-2}\mathrm{s}^{-1}$
Fast neutrons (1 keV-20 MeV)	3 * $10^{11}\mathrm{cm}^{-2}\mathrm{s}^{-1}$

The irradiation of the lanthanum and barium corresponding to the experiment conducted at pH ≈ 2 was done in BP2 of the RID. The irradiation times were adjusted accordingly for the $Ba(NO_3)_2$ to 39 min and for $La(NO_3)_3 \cdot 6\,H_2O$ to 230 min. To obtain similar specific activities for ^{139}Ba and ^{140}La.

3.4.3. Wallac measurements

The activity of all samples was measured using a Wallac Wizard2 Automatic Gamma Counter by PerkinElmer with an acquisition time of 1 minute per vial for the ^{139}Ba measurement. γ-rays in the region of interest (ROI) of ^{139}Ba were recorded within the energy range of 135 to 195 keV and the γ-rays in the ROI of ^{140}La were measured within the energy range of 410 to 580 keV. After 24 hours, when most of the ^{139}Ba had decayed, the measurement was repeated to detect ^{140}La with a 5-minute acquisition time per vial, while minimising the interference from overlapping γ-rays of the ^{139}Ba [38, 91]. The count rate was corrected using Equation 3.2 and Equation 3.3, taking into account overlapping γ-rays. Activities were decay-corrected over time.

3.4.4. Calculations

The partition coefficient was calculated by:

$$K_D = \left(\frac{C_{stock}}{C} - 1\right)\frac{V}{m} \tag{3.1}$$

Where:

- K_D is the partition coefficient [mL/g],
- C_{stock} is the gamma-ray count rate per volume of solution detected in the ROI for the stock solution [CPM/mL],
- C is the gamma-ray count rate per volume of solution detected in the ROI for the sample [CPM/mL],
- V is the volume of the added Ba/La mixture [mL],
- m is the mass of the sorbent [g].

The Ba^{2+} and La^{3+} counts were corrected by equations Equation 3.2 and Equation 3.3 respectively [38, 91]:

$$R_{\text{Ba, corrected}} = \frac{R_{\text{Ba}} - R_{\text{La}} * f_b}{1 - f_b * f_t} \tag{3.2}$$

$$R_{\text{La, corrected}} = \frac{R_{\text{La}} - R_{\text{Ba}} * f_t}{1 - f_b * f_t} \tag{3.3}$$

Where:

- $R_{\text{Ba, corrected}}$ is the corrected count rate of ^{139}Ba [CPM],
- $R_{\text{La, corrected}}$ is the corrected count rate of ^{140}La [CPM],
- R_{Ba} is the detected count rate of ^{139}Ba [CPM],
- R_{La} is the detected count rate of ^{140}La [CPM],
- f_b is the back/peak ratio constant for ^{140}La [-],
- f_t is the tail/peak ratio constant for ^{139}Ba [-].

The back/peak ratio constant for ^{140}La was determined by Spruit [38] to be 0.257 for R_{La} < 20,000 and 0.270 for R_{La} > 20,000 CPM. Swartjes [91] determined the tail/peak ratio of ^{139}Ba to be 0.0427.

3.4.5. Equilibrium experiment

To determine the time required to reach equilibrium for the adsorption of Ba^{2+} and La^{3+} onto the synthesised material, an experiment using TiP-I was conducted. First, 0.05 g of TiP-I was weighed and placed into individual 1.5 mL vials. A stock solution was prepared according to Section 3.4.1, using a pH of 7. The adsorption experiment followed the standard procedure described in Section 3.4, however, samples were collected after an exchange time of 30, 60, 90, 120, 180, 240, 360 minutes and 24 and 48 hours to determine equilibrium time. At each time point, a triplicate set of samples was reprocessed and measured to track the progression of ion adsorption.

3.4.6. Surface saturation experiment

In the standard adsorption experiments, the Ba/La mixture contained 1.5 mM Ba^{2+} and 2.5 µM La^{3+}. To evaluate whether saturation of available binding sites was a limiting factor for the adsorption, an experiment was conducted with elevated La^{3+} concentration. Specifically, adsorption experiments were performed using TiP-I and TiP-III-1:10-ex at pH 7, following the standard procedure described in Section 3.4 except for the La^{3+} concentration, which was increased to 1.0 mM using cold La. Ba^{2+} concentration was kept at 1.5 mM.

3.4.7. Ion competition experiment

Following the surface saturation experiments, an ion competition experiment was conducted to evaluate the influence of sequential ion addition on adsorption behaviour. Similarly to the previous adsorption experiments (Section 3.4), 0.050 g of TiP-I and TiP-III-1:10-ex were added to individual 1.5 mL vials. Initially, 0.9 mL of a MilliQ solution containing only Ba^{2+} ions was added. The mixtures were vortexed and placed in a carousel shaker for 1 hour. Thereafter, 0.1 mL of a MilliQ solution containing only La^{3+} ions was added, resulting in final concentrations of 1.5 mM Ba^{2+} and 1.0 mM La^{3+}. The samples were vortexed again and returned to the carousel shaker for an additional 5 hours before being processed according to the standard procedure.

To quantify how much Ba^{2+} was adsorbed prior to La^{3+} addition, a control experiment was conducted using TiP-I in which 0.9 mL of Ba^{2+} solution was added. After 1 hour 0.1 mL of MilliQ water, without La^{3+} ions, was added. This provided insight into the amount of Ba^{2+} initially adsorbed from a 1.5 mM solution, without subsequent competition.

3.4.8. Deprotonation experiment

To determine the change of pH induced by deprotonation of the TiP materials in an aqueous solution, an experiment using all sorbents (except TiP-III-1:0.5) was carried out. To replicate the same conditions as in the adsorption experiments, 0.05 g of each sorbent was added to individual 1.5 mL vials. Following, 1.0 mL of MilliQ water was added to each vail and the mixtures were vortexed for 5 seconds. Then the mixtures were put in a carousel for 5 hours before being centrifuged at 17,000 RCF, consistent with the adsorption procedure in Section 3.4. 0.5 mL of the supernatant was pipetted off and put in separate vials for pH measurements using a calibrated pH electrode.

4
Results and discussion

This chapter discusses the results from the experiments described in Chapter 3. In Section 4.1, the results of the synthesis are presented. Section 4.2 discusses the results of the adsorption experiments. Thereafter Section 4.3 explains the observation based on the theory discussed in Chapter 2. The results are then compared with similar experiments in literature in Section 4.4. Lastly, the practical applications are discussed in Section 4.5.

4.1. TiP Synthesis

This section discusses the results of the syntheses according to methods I, II and III in Section 4.1.1, Section 4.1.2 and Section 4.1.3, respectively.

4.1.1. Method I

The synthesis of the TiP-I material proceeded without noticeable changes in the visual appearance of the mixture during the process. Initially, the addition of TiO_2 to phosphoric acid resulted in a white, cloudy suspension at room temperature. Upon heating and continuous refluxing, the mixture retained its cloudy white appearance. Additionally, after the addition of MilliQ water and subsequent refluxing, the appearance of the mixture remained unchanged. Upon completing the reflux process and cooling to ambient temperature, TiP gradually sedimented at the bottom of the flasks, clarifying the upper layer. After the filtration, washing and drying, 5.56 g (87% molar yield of Ti, uncorrected for residual impurities) of uniform fine white product was obtained. Further structural and compositional characterisation was conducted to confirm product identity and purity.

4.1.1.1. XRD analysis

In Figure 4.1, the diffractogram of the TiP-I material is presented. The pattern closely aligned with the reference material of Amghouz et al. [44]. The peak at 11.5°, corresponding to the interlayer spacing of 7.58 Å [44, 85], was observed but with lower relative intensity than reported. This peak is the main structural marker of α-TiP. Notably, the diffractogram reported by Bruque [81], who performed a similar synthesis, shows relative intensities comparable to those observed in this study.

This variation may result from differences in preferred crystallographic orientation, which influence peak intensities in crystalline samples. For example, the study by Amghouz et al. [44] specifically aimed to crystallise single α-TiP crystals with suitable dimensions (>50 µm) for single-crystal X-ray diffraction. As a result, the XRD performed on these crystals likely reflects a dominant lattice orientation, enhancing the prominence of the interlayer distance of 7.58 Å in its diffractogram.

Secondly, sharper peaks were obtained in the reference material. This difference can be attributed to variations in crystallite size [80]. Amghouz et al. [44] state that the reference crystals have an average size of 50–100 µm, while, observed in Figure 4.2, TiP-I crystallites fall within the range of 1-5 µm. Their relatively small size likely increased surface-to-volume ratio and induced surface effects, which are known to cause peak broadening [80].

After excluding the peaks reported by Bruque [81], the remaining peaks aligned with the powder diffraction file (PDF) of TiO_2 (PDF: 01-083-2243) as reported by Khitrova [92]. Analysis using Highscore, based on relative intensity, indicated that the product consists of 94% α-TiP and 6% TiO_2. This quantification was limited by the fact that only a small portion of the total product was analysed during XRD

measurement. If this subsample was not fully representative of the entire batch, the relative peak intensities may not accurately reflect the overall composition. Although XRD is a bulk analysis method and the calculated percentages may lack high accuracy due to peak overlap [80], the presence of unreacted reactants in the product was evident, as indicated by the TiO_2 peak at 2θ = 25.3. The incomplete dissolution of TiO_2 in the first stage of the synthesis is a plausible explanation for the contamination, as no other substances were detected in the product.

To achieve complete dissolution of TiO_2, optimising the reaction conditions could be explored. Increasing the reaction temperature of the initial reflux may enhance the dissolution of TiO_2. Additionally, extending the duration of the reflux or increasing the concentration of phosphoric acid could promote more efficient interaction with TiO_2. These modifications could minimise contamination and improve the purity of the product.

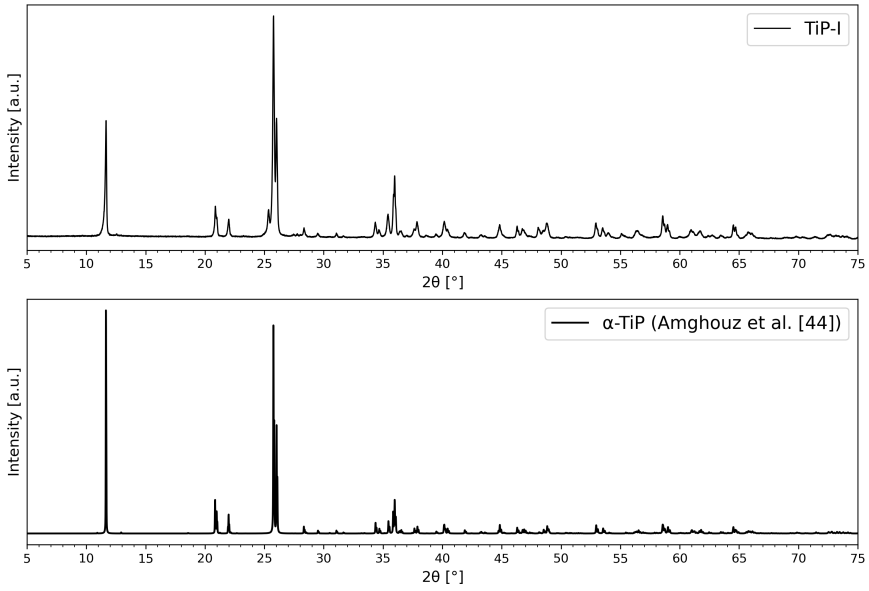

Figure 4.1: Powder XRD pattern of TiP-I material using a variable slit (top) compared the α-TiP synthesised by Amghouz et al. [44] (bottom) for comparison.

4.1.1.2. SEM analysis

Figure 4.2 shows SEM images of TiP-I crystallites, revealing their morphology and microstructure. The crystallite size was polydisperse, ranging from 1 to 5 µm with an average of around 3 µm, which exceeded the typical size reported in literature for comparable syntheses (500 nm) [81, 82, 93, 94]. However, the thickness of the crystallites can not be determined using SEM. The observed hexagonal morphology was consistent with the typical structure of α-TiP crystallites reported in previous research. This suggested that the synthesis conditions promoted well-defined crystallite growth [44, 81]. Fractured or deformed crystallites were present. This could result from mechanical stress during synthesis or inherent brittleness of the material [95]. Further investigation could determine whether synthesis conditions, such as stirring intensity or cooling rate, contribute to these deformations.

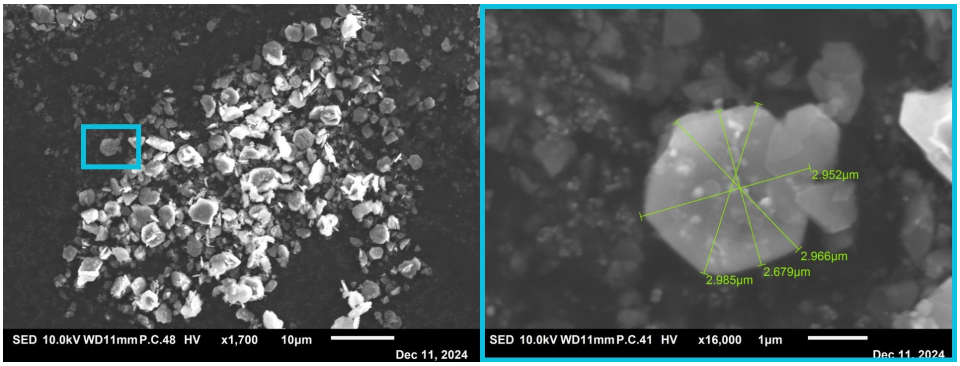

Figure 4.2: SEM images of the TiP-I crystallites, imaged at magnifications of 1,700x (left) and 16,000x (right).

4.1.1.3. EDS mapping

EDS mapping results, as shown in Figure 4.3, indicated that all atoms were homogeneously distributed across the surface of the crystallites. Given that the electron beam penetration depth (2 µm) exceeds the thickness of the crystallites, the apparent surface homogeneity may reflect bulk homogeneity, although this can not be confirmed definitively due to EDS resolution limitations [96]. The homogeneous distribution suggested that the synthesis method effectively prevented phase segregation or clustering of elements in the dried product.

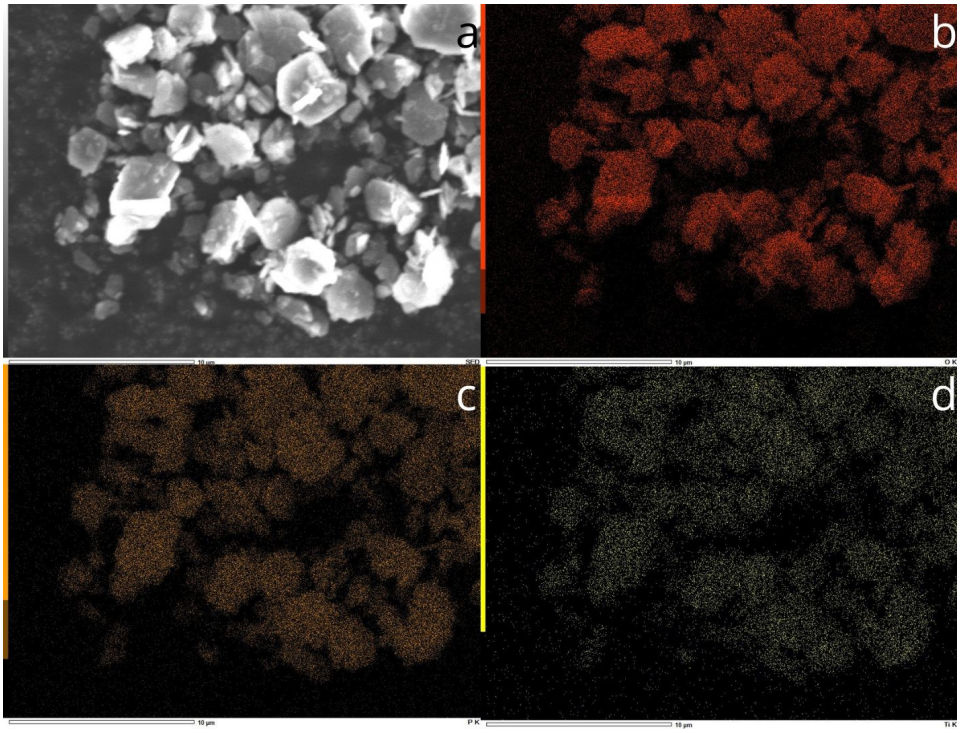

Figure 4.3: EDS mapping of the spatial distribution of O (b), P (c) and Ti (d) atoms across the imaged (a) TiP-I crystallites (5,000x).

Quantitative EDS analysis (Table 4.1) aligned well with the expected stoichiometry of α-TiP. Because EDS can not detect hydrogen, results were compared to the calculated values for TiP_2O_9, a hydrogen-free empirical approximation (Table A.1). Minor deviations of up to 5% are expected due to surface orientation effects and the 2D projection of 3D structures [97]. The results fell within this margin of error, further supporting the successful synthesis and compositional purity of α-TiP. Notably, the 6%

TiO_2 contamination was not detected using EDS, presumably because it fell within the uncertainty range of the EDS.

Table 4.1: Quantitative elemental composition of TiP-I material.

	TiP-I	
Element	Mass (%)	Atom (%)
O	58	76
P	24	16
Ti	18	8

To summarise, α-TiP was successfully synthesised using method I. The crystallites had a size of approximately 3 µm, exhibited high crystallinity and showed compositional homogeneity confirmed by EDS. Combined SEM, XRD, and EDS results support that method I yields α-TiP with uniform morphology, crystallinity and composition. However, XRD analysis revealed the presence of a minor impurity of TiO_2, likely due to incomplete precursor dissolution, indicating an opportunity for process optimisation through adjusted reaction conditions.

4.1.2. Method II

The synthesis of TiP-II material exhibited distinct visual and physical changes throughout the process. Upon the initial addition of titanium metal to phosphoric acid, the solution turned light grey, gradually transitioning to purple within approximately 30 minutes, as shown in Figure A.1, Appendix A. This colour change is linked to the formation of Ti^{3+} ions, which was consistent with findings in previous literature [82].

After an hour of refluxing, the solution turned translucent. Three hours later, white precipitate began to form, suggesting the initial crystallisation of TiP. By the end of the 24-hour reflux period, white product had sedimented at the bottom of the flask. This visual shift suggested that titanium metal was oxidised in solution and subsequently precipitated as TiP during the reflux process.

Filtration, washing and oven drying yielded 2.03 g of fine white product, corresponding to 76% molar yield of Ti. The product left to air dry overnight in the fume hood at ambient temperature were visually indistinguishable from oven-dried samples.

4.1.2.1. XRD analysis

The XRD diffractogram of the TiP-II material is presented in Figure 4.4 and exhibited reduced relative intensity of the interlayer peak and broader diffraction peaks, similar to those observed for TiP-I (Section 4.1.1). This peak broadening may arise from the smaller crystallite sizes of TiP-II, which enhanced surface effects and lattice distortions [80].

All observed peaks in the diffractogram aligned with the PDF for α-TiP reported by Bruque [81], as confirmed using Highscore analysis. This suggested that pure α-TiP was successfully synthesised. No secondary phases or impurities were detected in the measured sample, indicating that method II likely produced a single-phase material. This conclusion assumes that the analysed subsample is representative of the entire batch.

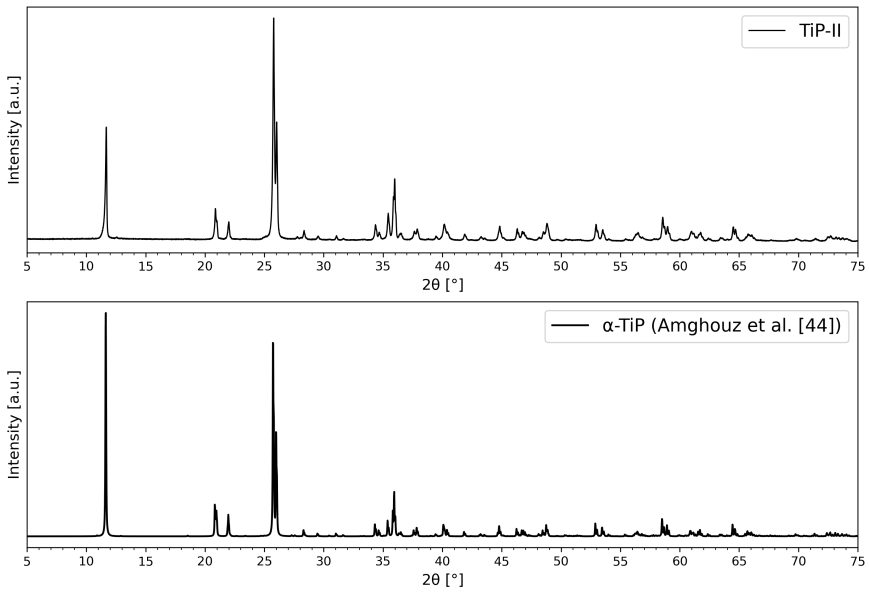

Figure 4.4: Powder XRD pattern of TiP-II material using a variable slit (top) compared the α-TiP synthesised by Amghouz et al. [44] (bottom) for comparison.

For the air-dried product, an identical XRD diffractogram was obtained (Figure A.2, Appendix A), suggesting that air drying does not significantly affect crystallinity under the conditions tested. However, oven drying was faster and therefore used consistently throughout this study.

4.1.2.2. SEM analysis

SEM images of the TiP-II crystallites, shown in Figure 4.5, revealed a polydisperse size distribution ranging from 1 to 5 µm, with an average size around 3 µm. The thickness of the crystallites could not be determined using SEM. The crystallites formed flat, hexagonal plates, consistent with those observed for TiP-I. Fractured and deformed crystallites were visible in the TiP-II samples, suggesting potential mechanical stress during synthesis [95]. Despite these deformations, the hexagonal morphology remained well-defined and was consistently observed across the majority of the imaged crystallites.

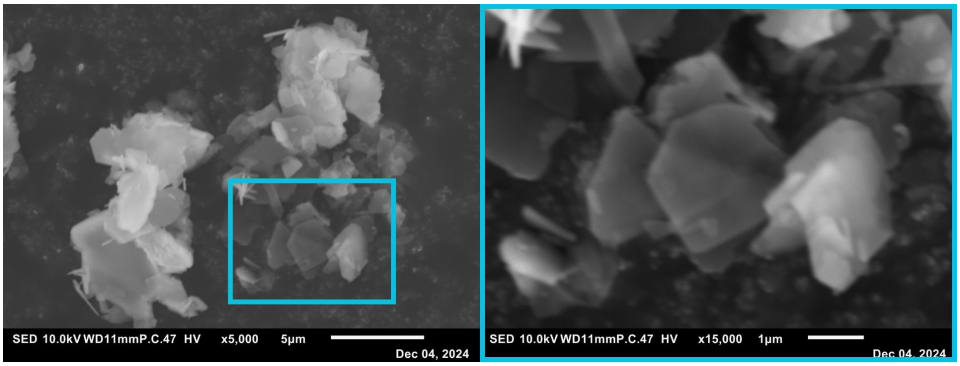

Figure 4.5: SEM images of TiP-II crystallites, imaged at magnifications of 5,000x (left) and 15,000x (right).

4.1.2.3. EDS mapping

EDS analysis revealed both qualitative element distribution and quantitative composition comparable to those observed for TiP-I. The EDS mapping, shown in Figure 4.6, confirmed a homogeneous distribution of the elements O, P and Ti across the surface of the crystallites. This supports the conclusion that the synthesis procedure yielded chemically homogeneous crystallites without significant elemental segregation.

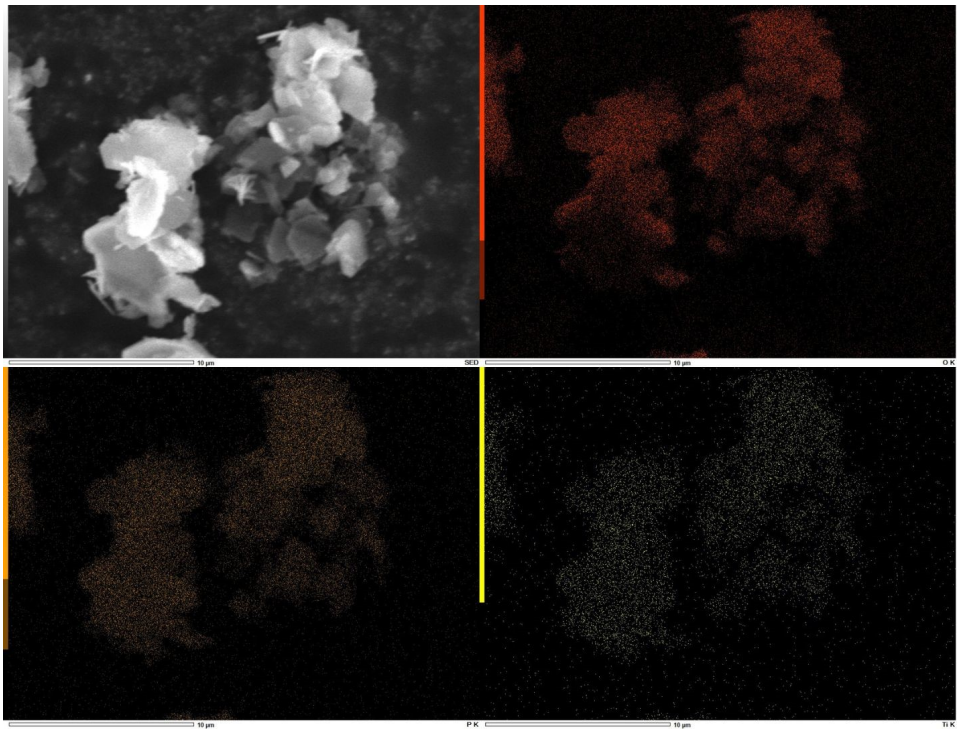

Figure 4.6: EDS mapping of the spatial distribution of O (b), P (c) and Ti (d) atoms across the imaged (a) TiP-II crystallites (5,000x).

The quantitative elemental composition of the TiP-II material, summarised in Table 4.2, also aligned with the values obtained for TiP-I material. As with TiP-I, hydrogen is not detected by EDS, so the composition was compared to the hydrogen-free empirical formula TiP_2O_9 (Table A.1).

Table 4.2: Quantitative elemental composition of TiP-II material.

	TiP-II	
Element	Mass (%)	Atom (%)
O	58	77
P	23	15
Ti	19	8

In summary, α-TiP was successfully synthesised using method II. XRD analyses confirmed no detectable impurities or secondary phases. The XRD results demonstrated that the obtained product matched the reference pattern for pure α-TiP. Additionally, SEM and EDS analyses revealed a uniform hexagonal morphology, with crystallites ranging from 1 to 5 µm and a modal size of approximately 3 µm, as well as a homogeneous elemental distribution across the observed surface.

Compared to method I, method II yielded α-TiP without detectable TiO_2 contamination, likely due to the more efficient reaction of titanium metal with phosphoric acid, promoting more complete precursor

dissolution. Method II required fewer synthesis steps and a shorter total reaction time, facilitating more time-efficient experimentation. A shorter synthesis time could reduce energy input costs in large-scale production, making method II potentially more practical for industrial applications.

To synthesise bigger crystallites, various conditions such as reflux time (72 hours and 14 days) and reflux temperature (100 and 170 °C) were varied. A brief overview of the results of these experiments according to method II is summarised in Appendix A in Table A.2. Key conclusions are, first, that repeated syntheses under identical conditions yielded comparable crystallite distributions and morphology. Second, no significantly enhanced crystallite growth (beyond 5 µm) was achieved under any of the tested conditions.

4.1.3. Method III

The synthesis of TiP-III material involved distinct visual and physical changes in the reaction mixture, indicating different stages of the dissolution and precipitation process. Initially, dissolving titanyl sulfate in preheated sulphuric acid produced a cloudy, syrupy liquid, which indicated incomplete dissolution. Upon continued reflux, the solution turned clear, suggesting the complete dissolution of the titanyl sulfate powder.

Following the addition of MilliQ water, the solution became less viscous but remained clear. Upon gradual, dropwise, addition of phosphoric acid, a gelatinous precipitate was immediately formed, while the solution turned white and milky. The rapid gel formation upon the phosphoric acid introduction highlighted the reactivity between titanium and phosphoric acid, suggesting the initial precipitation of titanium phosphate. After stirring for 5 more hours, the product turned into a denser precipitate.

Synthesis of TiP-III-1:0.42 and TiP-III-1:0.5 only yielded 0.9 g (13% molar Ti yield) and 1.7 g (26% molar Ti yield) respectively. Product loss during the washing step contributed to the low overall yields.

Washing using centrifugation offered an efficient alternative to vacuum filtration, as vacuum filtration required several days to complete. During vacuum filtration, densely packed product prevented water from passing through the filters, severely limiting throughput. In contrast, centrifugation enabled rapid and effective separation of the supernatant from the precipitate. The TiP-III-1:2.4 and TiP-III-1:10 material subjected to this alternative washing protocol, however, showed deviation from those processed with standard vacuum filtration. The resulting material appeared agglomerated. This could be explained by insufficient drying, suggesting the need for a longer drying protocol (10 hours at 50°C). The molar yields of Ti for the TiP-III-1:2.4 and TiP-III-1:10 materials were 61% and 89%, respectively.

The extended reflux process, according to method I, resulted in TiP-III material exhibiting similar visual characteristics and suspension behaviour to TiP-I. Upon the addition of phosphoric acid to the TiP-III material, a white cloudy mixture formed. Despite heating and continuous refluxing, the mixture retained its cloudy white appearance. Likewise, after adding MilliQ, no changes were observed, similar to method I. The molar yield of Ti in TiP-III-1:0.42-ex, TiP-III-1:2.4-ex and TiP-III-1:10-ex were 81, 55 and 63% respectively.

4.1.3.1. XRD analysis

XRD analysis (Figure 4.7) shows that the synthesis using method III primarily produces amorphous material. The diffractogram showed no distinct peaks in samples without extended reflux treatment, indicating that the structure of the material lacked order to provide clear information about the phases present or whether a reaction had occurred [98]. Consequently, conclusions about phase formation and material identity in these samples required complementary techniques like SEM and EDS.

After the extended reflux, the material partially crystallised into crystalline α-TiP, as indicated by the presence of identifiable peaks in the diffractogram. However, compared to the reference material and the results of TiP-I and TiP-II, relatively broad peaks were observed. This broadening could suggest

that the crystalline regions are combined with amorphous components [98].

Moreover, the peak broadening could be due to the small size of the TiP-III material [80]. The size of the crystallites was 500 nm for TiP-III-1:0.5-ex and TiP-III-1:2.4-ex and 200 nm for TiP-III-1:10-ex, as presented in Section 4.1.3.2. Despite this, the characteristic peaks of α-TiP could be identified, confirming its presence in the synthesised material.

Additionally, unexpected low-angle scattering was observed, which may stem from structural irregularities or instrumental artefacts rather than solely from amorphous phases [99]. This hypothesis was further explored using SEM analysis in Section 4.1.3.2, to assess whether clustering or surface irregularities contributed to the low-angle scattering.

Instrumental effects were found to increase air scattering at low angles. In particular, the use of a fixed anti-scatter slit used during the XRD analysis. For the TiP-I and TiP-II samples, a variable anti-scatter slit was employed, which dynamically adjusts to maintain consistent beam divergence and minimises background noise. In contrast, a fixed anti-scatter slit was used for the TiP-III materials, which does not adjust and may have introduced air scattering at low angles [100]. To investigate this hypothesis, a slit experiment was conducted, as described in Section A.1 in Appendix A. The results confirmed that the use of a fixed slit increases the detection of X-rays at low angles, indicating that these low-angle X-rays were caused by air scattering. For future studies, it is important to standardise slit configurations across all sample analyses to ensure consistent data quality and minimise the introduction of instrumental errors.

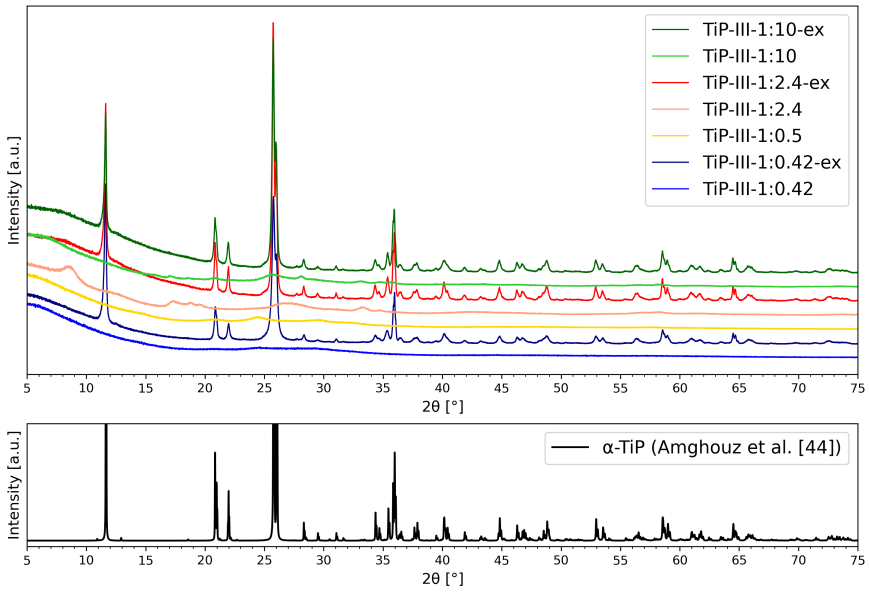

Figure 4.7: Powder XRD pattern of TiP-III materials using a variable slit (top) compared the α-TiP synthesised by Amghouz et al. [44] (bottom) for comparison. Individual diffractograms are provided in Appendix A.

All observed peaks in the diffractograms of the TiP-III-[ratio]-ex materials aligned with the PDF for α-TiP reported by Bruque [81], as confirmed by Highscore analysis. This supported the successful synthesis of α-TiP without detectable secondary phases. These results demonstrated the effectiveness of synthesis method III, combined with an extended reflux. However, as XRD is a bulk technique,

small impurities or amorphous components may remain undetected. If the analysed subsample is not fully representative of the entire batch, the recorded diffractogram may not fully reflect the overall composition of the bulk material [80].

4.1.3.2. SEM analysis and EDS mapping - Amorphous material

The results of SEM analysis and EDS mapping for the TiP-III material are presented in Appendix B. Similar morphological features were observed across the TiP-III-1:0.42, TiP-III-1:0.5, TiP-III-1:2.4 and TiP-III-1:10 material. The SEM images revealed two dominant morphologies in the 1:0.42, 1:0.5 and 1:2.4 samples, angular, rough-surfaced particles ('edgy', marked in blue) and irregular, filament-like clusters ('woolly', marked in green) as shown in Figure 4.8. In contrast, the TiP-III-1:10 material exhibited exclusively woolly morphologies, which appeared morphologically distinct from the other TiP-III samples, as visible in Figure 4.9. This difference suggests that lower Ti:H_3PO_4 ratios may promote the formation of amorphous, filamentous structures over crystalline angular morphologies. However, literature [84] suggested that lower Ti:H_3PO_4 ratios enhance crystallinity. This discrepancy may have arisen from differences in precursor solutions, as the literature used a $TiOSO_4 \cdot (H_2SO_4)x$ solution, whereas this study employed $TiOSO_4$ dissolved in sulfuric acid, which may alter the concentrations and availability of reactive titanium species or change the rate of hydrolysis, thereby influencing nucleation and crystallite growth.

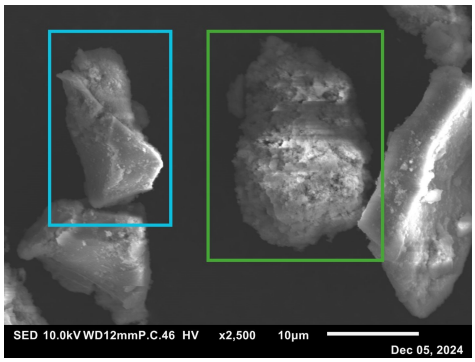

Figure 4.8: SEM image of the TiP-III-1:0.42 material, imaged at magnifications of 2,500x. An 'edgy' piece (blue) and a 'woolly' piece (green) are highlighted.

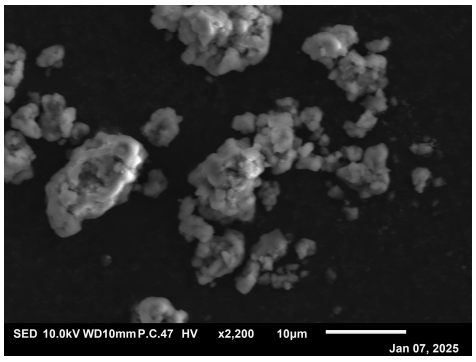

Figure 4.9: SEM image of the TiP-III-1:10 material, imaged at magnifications of 2,200x.

EDS mapping revealed that O, P and Ti were evenly distributed on the surface of all materials. However, unlike TiP-I and TiP-II, the greater thickness of the chunks exceeded the EDS electron beam penetration depth, preventing verification of compositional homogeneity beyond the surface. Nevertheless, the observed uniform surface distribution indicated that reactive sites are likely evenly accessible, which could favour efficient surface-based ion exchange or adsorption. Additionally, the quantitative analysis, summarised in Table 4.3 (and for TiP-III-1:0.5 in Table B.1) showed a deviation from the theoretical stoichiometry of TiP_2O_9, with elevated titanium and reduced phosphorus content. Nonetheless, these results supported the formation of titanium phosphate, despite its amorphous structure.

Table 4.3: Quantitative elemental composition of TiP-III-[ratio] materials.

	TiP-III-1:0.42		**TiP-III-1:2.4**		**TiP-III-1:10**	
Element	Mass (%)	Atom (%)	Mass (%)	Atom (%)	Mass (%)	Atom (%)
O	57	77	59	78	56	75
P	17	12	16	11	22	15
S	-	-	0.00	0.00	0.05	0.03
Ti	26	11	25	11	22	10

It should be noted that the results for TiP-III-1:0.42 presented in Table 4.3 and Figure B.2 are based on a revised measurement. The initial analysis, shown in Section B.8, revealed inconsistencies in the detection of elements O and P. Specifically, Figure B.15 (b) and (c) indicated the non-homogeneous elemental distribution across the surface of the material for O and P atoms, supported by the quantitative data in Table B.2. These values deviated from the expected stoichiometry of TiP_2O_9 shown in Table A.1.

A possible explanation for these inconsistencies is the 3D orientation of the material. During EDS analysis, characteristic X-rays may have been partially shielded by overlapping layers or specific orientations of the chunks, which may have caused localised detection errors [101]. To address this issue and validate the hypothesis, a revised measurement was performed, of which the results are shown in Figure B.2 and Table 4.3. The revised data closely aligned with the expected values, supporting that the observed inconsistencies in the initial measurement were likely due to X-ray shielding effects. This highlighted the inherent limitations of EDS for quantitative analysis in materials with complex morphology, as previously discussed in Section 4.1.1 [97].

Lastly, as shown in Table 4.3 and Table B.1, minor but detectable quantities of sulphur atoms were detected in the TiP-III-1:0.5 and TiP-III-1:10 materials. This suggested that the washing process did not fully remove residual sulphuric acid. This residual sulphuric acid could affect the adsorption behaviour by competing with the sorbent for ions [102].

4.1.3.3. SEM analysis and EDS mapping - Extended reflux

The SEM images and EDS mappings of the TiP-III materials subjected to extended reflux are presented in Appendix B, Section B.5, Section B.6 and Section B.7. In the SEM images of TiP-III-1:0.42-ex and TiP-III-1:2.4-ex crystallites, monodisperse, hexagonal crystallites of approximately 500 nm were observed. The thickness of the crystallites could not be determined using SEM. This size was consistent with previous studies on α-TiP [81, 82, 93, 94]. However, moderate clustering of the crystallites was observed, as illustrated in Figure 4.10.

Similarly to the amorphous TiP-III-1:10 material, TiP-III-1:10-ex also exhibited distinct morphology compared to the other crystalline samples. Due to limited resolution, the crystallite size of TiP-III-1:10-ex could not accurately be determined. Therefore, Transmission Electron Microscopy (TEM) was used to analyse this sample, revealing well-defined, hexagonal crystallites with a diameter of approximately 200 nm in Figure 4.11.

The combined SEM and TEM observations support the interpretation that the peak broadening in Figure 4.7 is partially caused by the reduced crystallite size. Such broadening is characteristic of nanoscale materials, where smaller crystallite domains contributed to peak broadening in XRD diffractograms [80].

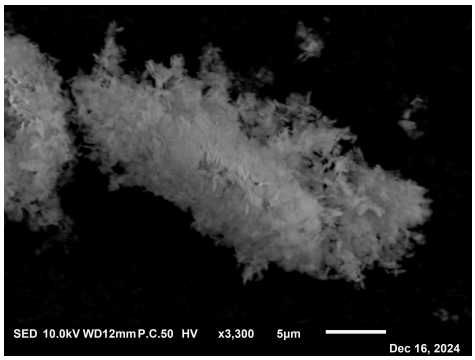

Figure 4.10: SEM image of the clustered TiP-III-1:0.42-ex crystallites, imaged at magnifications of 3,300x.

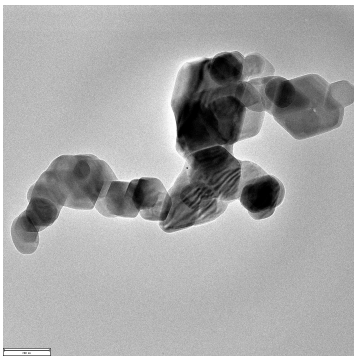

Figure 4.11: TEM image of the TiP-III-1:10-ex crystallites, scale bar represents 200 nm.

The results of quantitative EDS measurements, presented in Table 4.4, aligned with the expected stoichiometry of TiP_2O_9, as shown in Table A.1. Qualitative EDS mapping confirmed that O, P and Ti were evenly distributed across the surface of all crystallites. Given the small thickness of the crystallites, it was interpenetrated that the elemental distribution was homogenous throughout the material, as exemplified by Figure B.12.

Table 4.4: Quantitative elemental composition of TiP-III-[ratio]-ex materials.

	TiP-III-1:0.42-ex		**TiP-III-1:2.4-ex**		**TiP-III-1:10-ex**	
Element	Mass (%)	Atom (%)	Mass (%)	Atom (%)	Mass (%)	Atom (%)
O	60	78	58	76	60	78
P	21	14	22	15	21	14
S	0.03	0.02	0.00	0.00	0.04	0.03
Ti	18	8	20	9	19	8

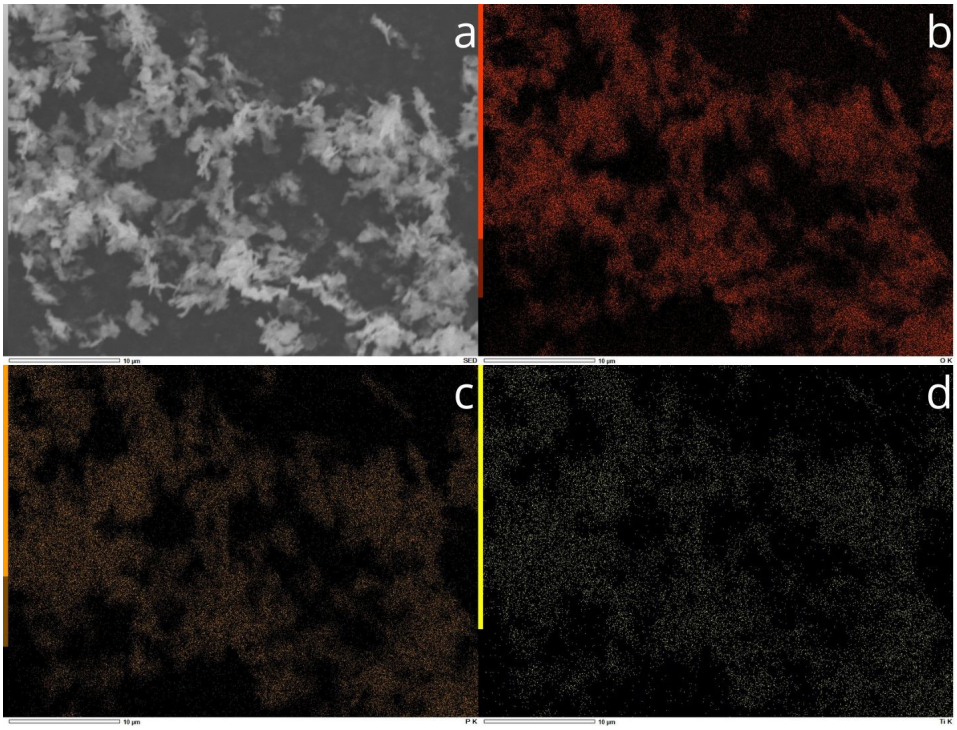

Figure 4.12: EDS mapping of the spatial distribution of O (b), P (c) and Ti (d) atoms across the imaged (a) TiP-III-1:2.4-ex crystallites (3,000x).

Although literature [84] suggests that varying Ti:H_3PO_4 ratios affect crystallinity, method III initially produced amorphous titanium phosphate for all tested ratios, with variations in morphology including differences in particle shape and surface texture. Lower ratios exhibited a mix of angular, rough-surfaced particles and irregular, woolly clusters, whereas higher ratios (TiP-III-1:10) favoured exclusively woolly, irregular structures. This outcome was expected, as rapid precipitation typically limits crystal lattice formation, leading to an amorphous phase. Only upon extended reflux (slow re-crystallisation) did ordered crystallites form [37].

After extended reflux, method III successfully synthesised α-TiP, suggesting that the Ti:H_3PO_4 ratio may have influenced crystallite morphology. XRD analysis confirmed the presence of α-TiP, with peak broadening likely resulting from nanoscale crystallite sizes and potential amorphous components. SEM

imaging revealed well-defined, occasionally clustered hexagonal crystallites (500 nm) in TiP-III-1:0.42-ex and TiP-III-1:2.4-ex, while TiP-III-1:10-ex exhibited smaller, well-defined hexagonal crystallites (200 nm), as confirmed using TEM imaging. Both qualitative and quantitative EDS analyses confirmed the homogeneous elemental distribution throughout the crystallites, supporting the conclusion that extended reflux facilitates the formation of compositionally uniform crystalline α-TiP.

4.1.4. Conclusions synthesis

Comparing the three synthesis methods in terms of crystallinity, particle size, and purity, method I yielded relatively large (1 to 5 µm), well-formed α-TiP crystallites with minor TiO_2 contamination, likely resulting from incomplete precursor dissolution, as suggested by XRD analysis. Method II produced equally crystalline α-TiP with comparable morphology but higher purity, attributed to the more complete reaction of titanium metal. In contrast, method III required extended reflux to achieve crystallinity and resulted in much smaller, nanoscale crystallites (200–500 nm).

The structural characteristics of all synthesised TiP materials are presented in Table 4.5. It summarises key outcomes of synthesis and characterisation procedures, including crystallinity, phase composition and estimated particle size. These parameters are essential for understanding the surface reactivity, ion exchange capacity and separation performance of the synthesised materials.

Table 4.5: Summary of structural characteristics of the synthesised TiP materials.

Sorbent	Crystallinity	Phase Composition	Particle Size
TiP-I	Crystalline	Heterogeneous	1 - 5 µm
TiP-II	Crystalline	Homogeneous	1 - 5 µm
TiP-III-1:0.42	Amorphous	-	-
TiP-III-1:0.5	Amorphous	-	-
TiP-III-1:2.4	Amorphous	-	-
TiP-III-1:10	Amorphous	-	-
TiP-III-1:0.42-ex	Crystalline	Homogeneous	500 nm
TiP-III-1:2.4-ex	Crystalline	Homogeneous	500 nm
TiP-III-1:10-ex	Crystalline	Homogeneous	200 nm

It should be noted that all samples were measured from a single batch. Future experiments should include repeated syntheses under identical conditions to ensure reproducibility and validate the robustness of the results.

4.2. Adsorption experiments

The pH-dependent adsorption behaviour of Ba^{2+} and La^{3+} on six synthesised TiP materials is shown in Figure 4.13 (individual plots in Figure C.1, Appendix C). These data illustrated how structural differences, detailed in Section 4.1 and summarised in Table 4.5, affect ion adsorption under acidic conditions.

In this study, all adsorption experiments were conducted under nearly identical conditions, including equal initial ion concentrations, consistent sorbent mass and fixed solution volume. This allowed for a valid comparison between the different TiP materials within this study. Observed differences in adsorption can therefore be attributed to material properties rather than experimental variation. While adsorption percentages offered a useful initial indication of sorbent performance, they were inherently influenced by experimental parameters such as ion concentration, volume-to-liquid ratio and sorbent mass. Consequently, the adsorption percentage values reflected only the apparent affinity of the sorbent under the specific test conditions. For broader comparison with varying experiments in literature, as discussed in Section 4.4, adsorption behaviour is expressed using the partition coefficient (K_D),

shown for all TiP materials in Figure 4.14 (individual plots in Figure C.2, Appendix C). Unlike percentage values, K_D reflects the ion distribution between solid and liquid phases [27].

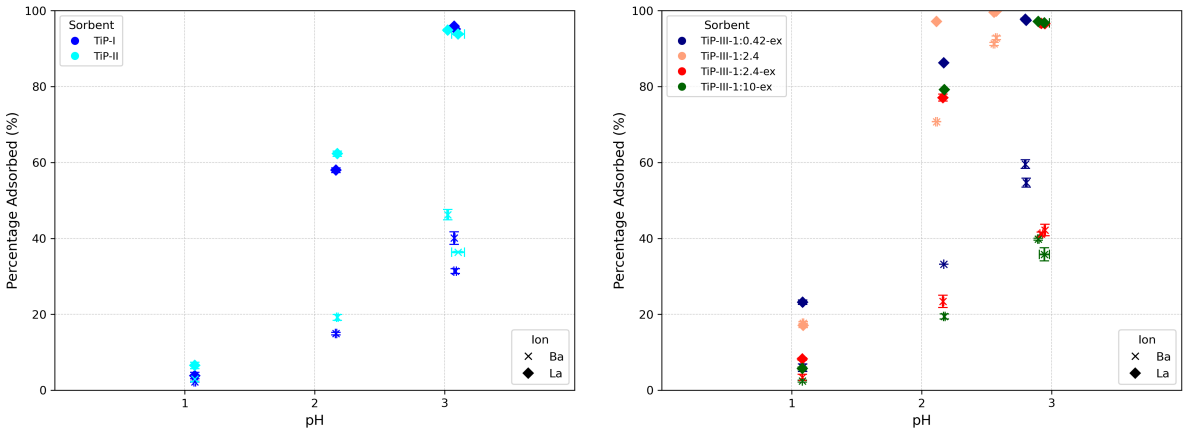

(a) TiP-I and TiP-II

(b) TiP-III

Figure 4.13: Effect of equilibrium pH on Ba^{2+} (C_0 = 1.5 mM) and La^{3+} (C_0 = 2.5 µM) uptake by TiP-I, TiP-II and TiP-III materials (batch tests, 0.05 g sorbent, 20 °C).

For all materials, the adsorption of trivalent La^{3+} was consistently higher than that of divalent Ba^{2+}. This selectivity aligns with findings for other phosphate and oxide sorbents [27, 38], as discussed in Section 4.4. At pH 1, all crystalline materials showed poor adsorption of both ions, with uptake below 10%. This low uptake may be due to significant proton competition at low pH, as discussed in Section 2.3.2, which explains this reduced ion exchange capacity under strongly acidic conditions [103]. As the pH increased, the difference in uptake between Ba^{2+} and La^{3+} became more distinct, with La^{3+} adsorption increasing more steeply. This consistent preference for La^{3+} over Ba^{2+} demonstrates that all materials can differentiate between ions of different charge. However, the magnitude of this selectivity varied across the materials, suggesting that structural differences influenced their ion exchange behaviour.

TiP-I and TiP-II exhibited nearly identical adsorption behaviour across the entire pH range, with TiP-II showing slightly higher adsorption of both Ba^{2+} and La^{3+} at pH 1 and 2 (Figure 4.13a). Similarly, the adsorption profiles of TiP-III-1:2.4-ex and TiP-III-1:10-ex were closely aligned (Figure 4.13b). Although these materials differ in particle size (500 nm and 200 nm, respectively, Table 4.5), this distinction appeared insufficient to affect ion uptake, possibly because both materials exhibited similarly high surface accessibility and reached comparable saturation levels under the tested conditions. This may suggest that, within the submicron range explored, particle size differences alone did not strongly influence ion uptake.

In contrast, the adsorption trends presented in Figure 4.13 suggested that the smaller particle sizes of TiP-III-1:2.4-ex and TiP-III-1:10-ex (200–500 nm) led to different adsorption behaviour compared to the larger crystallites of TiP-I and TiP-II (3 µm). This is particularly evident at pH ≈ 2 and supported by the consistently higher partition coefficients across the pH range (Figure 4.14). Further investigation is needed to clarify whether the observed differences stem primarily from particle size, affecting the surface-to-volume ratio and thus site accessibility or from structural factors such as crystallinity, which could influence the density or accessibility of reactive phosphate groups.

The consistent behaviour observed between TiP-I and TiP-II and among TiP-III-1:2.4-ex and TiP-III-1:10-ex, suggested that these materials share similar levels of crystallinity, surface characteristics and phosphate site accessibility. Minor variations in performance may result from batch-dependent factors such as small differences in crystallinity or residual moisture. For TiP-III-1:2.4-ex and TiP-III-1:10-ex,

variations in particle size may also contribute to differences in adsorption. Given the limited variation and overlapping adsorption trends, the performance of TiP-I and TiP-II can be considered functionally equivalent within the error margins of the adsorption measurements.

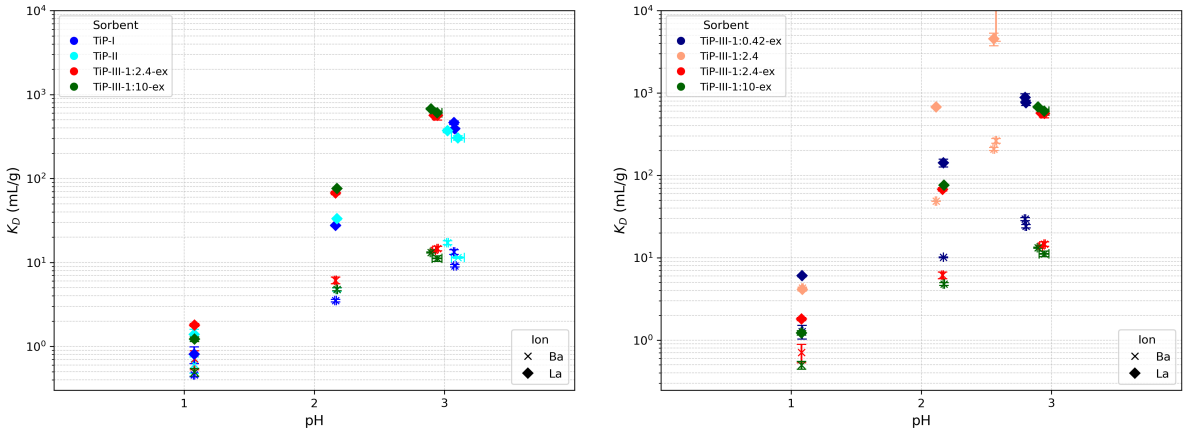

(a) TiP-I TiP-II, TiP-III-1:2.4-ex and TiP-III-1:10-ex

(b) TiP-III

Figure 4.14: Partition coefficients (K_D) for Ba^{2+} (C_0 = 1.5 mM) and La^{3+} (C_0 = 2.5 µM) on TiP-I, TiP-II and TiP-III materials (batch tests, 0.05 g sorbent, 20 °C).

The amorphous TiP-III-1:2.4 material showed high overall adsorption of both Ba^{2+} and La^{3+} (Figure 4.13). This broad uptake is consistent with its disordered morphology observed in SEM and lack of crystalline features in XRD, which suggested a high density of accessible binding sites, as also reported in previous studies [38, 41, 42, 69]. Furthermore, the material showed poor ion discrimination, likely due to the absence of well-defined binding sites. The material showed high uptake, with a low selectivity ratio for Ba^{2+} and La^{3+} ions, making it unsuitable for separation applications. As a result, TiP-III-1:2.4 was excluded from further analysis in this study due to its lack of selectivity.

The adsorption behaviour of TiP-III-1:0.42-ex for Ba^{2+} deviated from that of the other crystalline TiP-III materials. Although XRD (Figure 4.7) indicated a predominantly crystalline phase, the adsorption profile showed a similar trend to the amorphous TiP-III-1:2.4 material, with reduced selectivity and elevated Ba^{2+} uptake at low pH. (Figure 4.14b). This observation may indicate residual amorphous domains or structural disorder, which would also explain the peak broadening observed in the XRD. These findings underlined the limitations of XRD in characterising nanocrystalline materials. Like TiP-III-1:2.4, the reduced selectivity of TiP-III-1:0.42-ex between Ba^{2+} and La^{3+} made it unsuitable for further investigation in this study.

The results highlighted three key trends for the investigated conditions. First, adsorption efficiency increased with pH across all materials. This trend is consistent with proton competition mechanisms, where fewer protons at higher pH reduce site occupation, enabling more cation adsorption [103]. Second, although smaller crystallites generally have higher surface area and better accessibility of functional groups, this did not consistently lead to improved adsorption or selectivity. TiP materials with different particle sizes exhibited small differences in performance under the tested conditions. Third, crystallinity played a central role in ion adsorption. Crystalline TiP materials consistently showed greater selectivity for La^{3+} over Ba^{2+}, whereas the amorphous TiP-III-1:2.4 showed reduced specificity, suggesting that structural order enhanced selective binding.

4.2.1. Limitations

This section outlines the practical constraints and uncontrolled variables that may have influenced the adsorption results in Section 4.2.1.1 and Section 4.2.1.2, respectively. This provides context for

interpreting experimental reliability, reproducibility and deviations from intended test conditions.

4.2.1.1. Practical considerations

The adsorption experiments were time-limited due to the short half-life of ^{139}Ba (83.06 minutes [104]), requiring all measurements to be completed within one day. Although the standard protocol prescribes a five-hour contact time for ion exchange (Section 3.4), equilibrium experiments (Section 4.2.2) confirmed that equilibrium was reached within 30 minutes for the tested concentration ($C_{0,Ba}$ = 1.5 mM and $C_{0,La}$ = 2.5 µM). Therefore, despite shorter contact times, conditions were assumed to be sufficient for an equilibrium to be established. Exact contact times are listed in Appendix C, Section C.1.

Secondly, the adsorption experiments were carried out at ambient temperature. However, during this study, the ambient temperature in the labs was not constant. Minor variations in temperature between the experiments occurred, which have influenced results, as adsorption capacity is temperature-dependent. Still, based on literature data, the observed ambient temperature variations of 17–21 °C are expected to cause only a minor impact on the adsorption results, likely within 1–2% variation in adsorption capacity [39, 69].

All experiments were performed in triplicate to reduce sources of experimental error, such as pipetting and weighing errors. However, the triplicates were not based on separate syntheses and thus are not independent. Therefore, the triplicates account for measurement uncertainty rather than sample-to-sample variability. Moreover, measurement uncertainties from the Wallac gamma counter could not be fully accounted for due to constraints in Equation 3.1. This may have led to consistent overestimation or underestimation of C and C_{stock}, thereby affecting reported adsorption percentages and partition coefficients. The standard deviation calculated from the triplicate measurements accounts for variations between experiments but does not capture the inherent counting error in the individual measurements of C_{stock} and C in Equation 3.1. These follow Poisson statistics and affect the partition coefficient non-linearly. Full uncertainty quantification would require formal error propagation [105].

The pH numbers shown in this study include only the standard deviation observed between the triplicates (σ). They do not include the extra error introduced from electrode calibration (three-point calibration), electrode drift or small temperature shifts. Additional uncertainties of ± 0.02 pH lead to a K_D shift of less than 3%. This is small compared to the overall experimental variation and had minor impact the conclusions regarding adsorption behaviour.

4.2.1.2. Uncontrolled variables

Post-experimental pH measurements revealed that, regardless of initial pH targets of pH 7, 5, and 3, the actual equilibrium pH in all cases converged to approximately 3. The measured pH values are listed in Section C.1, Appendix C. Several factors may have contributed to this unintended acidification, as discussed below.

First, spontaneous deprotonation of surface hydroxyl groups is a well-documented behaviour of TiP materials, particularly those with high surface area [35, 69]. As demonstrated in the deprotonation experiment (Section 4.2.5), all sorbents acidified MilliQ water to some extent, with pH values as low as 2.95. This indicated that proton release from the surface occurred even in the absence of added ions.

Second, incomplete neutralisation during washing may have left trace amounts of phosphoric or sulphuric acid on or between particles, as suggested by sulphur detection in EDS analysis in Table 4.3. While pH paper tests of eluents during washing suggested near-neutral pH (6), such methods may not detect weakly adsorbed or slowly released acid residues.

Third, ion exchange itself contributed to acidification. When Ba^{2+} and La^{3+} occupied exchange sites (Equation 2.2). Protons were exchanged and released into the solution. This process is inherent to cation exchange and may further amplify acidification during exchange. Together, these mechanisms

likely explain why experiments intended at pH 5 and 7 were conducted around pH 3.

For TiP-III-1:2.4, the experiment intended at pH 3, was performed in duplicate due to a handling error that resulted in the loss of sample C34Y. The final values and standard deviations were calculated accordingly based on the remaining two replicates.

The partition coefficient for Ba^{2+} in the experiment intended at pH 3 for TiP-III-1:10-ex was negative. Negative K_D results were obtained when in Equation 3.1, the count rate per volume (C) after equilibration exceeded the initial stock count rate per volume (C_{stock}), so. $C_{stock}/C < 1$. A likely explanation was a non-homogeneous stock solution. This was supported by the control measurements. As a result, the adsorption for Ba^{2+} in this experiment likely overestimated the true ion uptake. A lower actual Ba^{2+} concentration in the stock solution would make relative uptake appear higher than it was, artificially increasing the adsorption percentages and partition coefficients. This was consistent with the overall higher apparent uptake of both Ba^{2+} and La^{3+} compared to experiments conducted at similar equilibrium pH. Given the inconsistency and likely overestimation, the results from this experiment were excluded from the graphical representation and further analysis.

The experiment at pH ≈ 2 for TiP-III-1:0.42-ex was carried out in duplicate and using less sorbent mass, due to the limited yield of the sorbent. The deviating sorbent weights used in this experiment are listed in Appendix C, Table C.6. Although the lower solid-to-liquid ratio limited the comparability of adsorption percentages, the data remained valid for calculating partition coefficients, which accounted for the sorbent mass.

4.2.2. Equilibrium experiment

An experiment with varying exchange time was conducted to determine the time required to reach an adsorption equilibrium for Ba^{2+} and La^{3+} under the experimental conditions in this study. The results of the experiments are presented in Figure 4.15 and the data plateau indicates that equilibrium was effectively reached within 30 minutes. This rapid equilibration is consistent with literature reports of α-TiP, reaching equilibrium uptake within tens of minutes [39, 69].

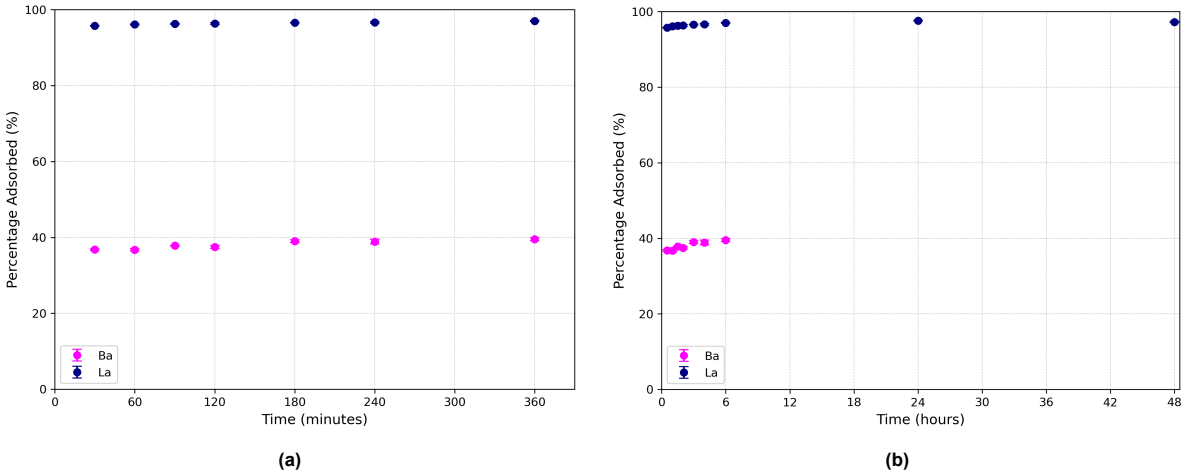

Figure 4.15: Time-dependent adsorption of Ba^{2+} (C_0 = 1.5 mM) and La^{3+} (C_0 = 2.5 µM) on TiP-I (batch tests, 0.05 g sorbent, 20 °C, pH = 3.23 ± 0.03.

Ba^{2+} adsorption data was only available for the first 6 hours. This limitation arose due to the short half-life (83.06 minutes [104]) of the barium-139 isotope, which decayed rapidly and became undetectable beyond this period. Despite this constraint, the data clearly showed that both Ba^{2+} and La^{3+} adsorption reached equilibrium within the first 30 minutes, with plateau values of approximately 40% and >95%,

respectively. For La^{3+}, this equilibrium was maintained over 48 hours (Figure 4.15b), indicating that no desorption occurred over time and that La^{3+} remained stably bound under these conditions.

The results for Ba^{2+} in Figure 4.15a showed adsorption levels between 35% and 40%, which were consistent with the values reported in the batch adsorption experiments for TiP-I, where uptake ranged between 30% and 40% at pH ≈ 3. Similarly, La^{3+} adsorption matched batch experiments, with uptake remaining >95% at pH ≈ 3.

It should be noted that these findings are specific to TiP-I at pH ≈ 3.2 and do not necessarily apply to other TiP materials or pH conditions. However, given the comparable size and crystallinity of other synthesised TiP materials, similar equilibration times are likely, although not experimentally confirmed.

The observed equilibration within 30 minutes was consistent with literature on α-TiP. Shao et al. [69] reported rapid uptake of La^{3+} within this timeframe, though at higher concentrations (1 mM) and pH 4.86. Although ion exchange kinetics are concentration-dependent, the consistent rapid equilibration observed for La^{3+} in this study suggested that the fast kinetics of α-TiP are maintained across a broad concentration range, as further discussed in Section 4.3.1.2.

4.2.3. Surface saturation experiment

The surface saturation experiment was designed to investigate the adsorption behaviour of TiP-I and TiP-III-1:10-ex under elevated La^{3+} concentration. The initial La^{3+} concentration was increased from 2.5 µM to 1.0 mM, while maintaining the Ba^{2+} concentration at 1.5 mM. Adsorption percentages at pH ≈ 3 are shown in Table 4.6.

Table 4.6: Ba^{2+} and La^{3+} adsorption on TiP-I and TiP-III-1:10-ex at different initial La^{3+} concentrations (batch tests, 0.05 g sorbent, 20 °C, C_0 Ba^{2+} = 1.5 mM).

C_0 **La^{3+}**	**Sorbent**	**La^{3+} adsorption** (%)	**Ba^{2+} adsorption** (%)	**pH** ± σ (n = 3)
1.0 mM	TiP-I	54 ± 2	22 ± 1	3.07 ± 0.01
1.0 mM	TiP-III-1:10-ex	67.9 ± 0.2	21.8 ± 0.2	2.92 ± 0.02
2.5 µM	TiP-I	95.2 ± 0.1	31.4 ± 0.6	3.08 ± 0.01
2.5 µM	TiP-III-1:10-ex	97.1 ± 0.1	39.8 ± 0.3	2.90 ± 0.01

At the higher La^{3+} concentration, the adsorption percentage of La^{3+} decreased substantially for both materials from >95% to 54 ± 2% for TiP-I and to 67.9 ± 0.2% for TiP-III-1:10-ex. This reduction likely resulted from surface site saturation at higher concentrations, which shifted the equilibrium toward lower relative uptake. The consistently higher La^{3+} uptake of TiP-III-1:10-ex compared to TiP-I was likely attributed to its smaller particle size (200 nm vs. 3 µm), resulting in a larger surface area and potentially improving accessibility of reactive sites. At lower La^{3+} concentrations, this difference was not detectable within experimental uncertainty. However, slightly elevated La^{3+} uptake at pH ≈ 2 and higher partition coefficients observed in prior experiments support this interpretation (Section 4.2). These findings support the conclusion that adsorption behaviour is influenced by surface accessibility, as smaller particles provide more accessible sites for ion exchange [69]. Moreover, at elevated ion concentrations, the higher La^{3+} uptake by nano-sized TiP-III, despite similar Ba^{2+} uptake, indicated higher selectivity towards La^{3+} relative to TiP-I.

Ba^{2+} was adsorbed under elevated La^{3+} conditions, although adsorption decreased for both materials. For TiP-I, it dropped from 31.4 ± 0.6% to 22 ± 1% and for TiP-III-1:10-ex, from 39.8 ± 0.3% to 21.8 ± 0.2%. This decrease reflects competition for binding sites, with the higher-affinity trivalent La^{3+} displacing Ba^{2+} from available exchange sites. Partial retention of Ba^{2+} indicates that co-adsorption occurred.

4.2.4. Ion competition experiment

The ion competition experiment was conducted to investigate whether sequential ion addition affects the adsorption behaviour of TiP-I and TiP-III-1:10-ex and examine the competitive exchange scenario further. Specifically, Ba^{2+} was introduced first and allowed to exchange with the sorbent before adding La^{3+}. A control experiment with only Ba^{2+} present was also included to quantify the Ba^{2+} uptake in the absence of La^{3+}. The final ion concentrations in all experiments were 1.5 mM for Ba^{2+} and, if added, 1.0 mM for La^{3+} and adsorption percentages are presented in Table 4.7.

Table 4.7: Ba^{2+} and La^{3+} adsorption on TiP-I and TiP-III-1:10-ex after subsequent ion addition (batch tests, 0.05 g sorbent, 20 °C, C_0 Ba^{2+} = 1.5 mM).

Sorbent	$C_{0,La}$ (mM)	**La^{3+} adsorption** (%)	**Ba^{2+} adsorption** (%)	**pH** ± σ (n = 3)
TiP-I	1.0	53.9 ± 0.6	17.7 ± 0.8	3.06 ± 0.01
TiP-I	-	-	29.2 ± 0.5	3.18 ± 0.01
TiP-III-1:10-ex	1.0	64.1 ± 0.5	20.0 ± 0.2	2.90 ± 0.01

In the control experiment (Ba^{2+} only), TiP-I showed a Ba^{2+} uptake of 29.2 ± 0.5%, closely matching the value obtained in the adsorption experiments under low La^{3+} conditions (31.4 ± 0.6%, see Table 4.6). This consistency confirmed that, in the absence of significant competition, Ba^{2+} reaches a stable and reproducible adsorption level. Moreover, the reduction in adsorbed Ba^{2+} after La^{3+} introduction, showed that La^{3+} effectively competed for binding sites and partially displaced previously adsorbed Ba^{2+}. Given that displacement occurred even after Ba^{2+} was pre-adsorbed, this suggested that the stronger affinity of La^{3+}, rather than site availability alone, dominated competition.

When La^{3+} was added to a system pre-equilibrated with Ba^{2+}, the adsorption pattern shifted to closely match the results of the experiment where both ions were introduced simultaneously (Table 4.6). This indicated that the system reached a dynamic equilibrium regardless of the ion addition sequence.

4.2.5. Deprotonation experiment

The adsorption experiments that were intended at pH 5 and 7 resulted in an equilibrium pH of 3, as discussed in Section 4.2.1. To assess the influence of deprotonation and residual acids in the acidification of the solution, the pH of water equilibrated with different sorbents was measured without ion exchange. The results are presented in Table 4.8. Deprotonation of surface hydroxyl groups led to acidification of the surrounding solution. A lower pH, therefore, indicated more extensive deprotonation, typically associated with higher surface area and greater surface reactivity. According to literature [39, 69], only the hydroxyl groups at the outer surface deprotonate, while those located between crystal layers remain stabilised by water, making only the outer hydroxyl groups reactive.

Table 4.8: Average pH and standard deviation of measured samples.

Sorbent	**pH** ± σ (n = 3)
TiP-I	3.51 ± 0.01
TiP-II	3.61 ± 0.02
TiP-III-1:2.4	2.95 ± 0.01
TiP-III-1:2.4-ex	3.28 ± 0.01
TiP-III-1:10-ex	3.27 ± 0.01
MilliQ water	5.78 ± 0.06

The amorphous material TiP-III-1:2.4 showed the lowest pH value, indicating the highest degree of deprotonation. This result was consistent with its disordered structure, which likely resulted in a higher accessible surface area compared to the more crystalline samples. In contrast, the crystalline TiP-III

forms (TiP-III-1:2.4-ex and TiP-III-1:10-ex) exhibited higher pH values, suggesting reduced deprotonation. Given that pH is a logarithmic scale, this difference implied a substantially lower proton release, supporting the hypothesis that deprotonation is restricted to accessible surface hydroxyl groups.

These observations aligned with the behaviour of TiP-I and TiP-II, both of which had larger crystallites and consequently lower surface areas. As expected, they induced less acidification of the surrounding solution. The overall trend confirmed that the extent of deprotonation was strongly surface-area dependent and therefore influenced by crystallinity and particle size. This highlighted the role of surface accessibility in controlling the ion exchange capacity and reactivity of the sorbents.

Residual acid from synthesis likely also contributed to the acidification of the system. While surface deprotonation is expected to be the dominant cause of pH reduction, trace amounts of phosphoric or sulphuric acid trapped within the sorbent structure could lower the measured pH, as discussed in Section 4.2.1 [106].

Notably, the higher pH values in Table 4.8 compared to those in Section C.1 suggested that an additional factor contributed to acidification beyond surface deprotonation and residual acids. This was likely induced by the adsorption of Ba^{2+} and La^{3+}, consistent with proton displacement during ion exchange as discussed in Section 2.3.2 and Section 4.3.1.

4.2.6. Conclusion adsorption experiments

The adsorption experiments demonstrated that ion exchange on α-TiP is dominated by surface adsorption, fast kinetics and ion competition effects. The sorbents consistently exhibited a preference for La^{3+} over Ba^{2+}. Adsorption capacity and selectivity depended on the morphology of the synthesised α-TiP, highlighting the importance of structural optimisation. To further interpret these findings, the following section explores the underlying ion exchange mechanisms, thermodynamics and adsorption modelling using the competitive Langmuir model.

4.3. Ion exchange of α-TiP

To understand the experimentally observed differences in adsorption behaviour between Ba^{2+} and La^{3+}, this section uses the mechanistic framework provided in Section 2.3.2 that supports and explains the results presented in Section 4.2. Section 4.3.1 outlines the surface chemistry of α-TiP and the proton–cation exchange mechanism that supports the selective uptake of multivalent cations. In Section 4.3.2, thermodynamic parameters from literature are used to further substantiate the observed trends. These analyses revealed that the ion exchange process is surface-controlled, selective and strongly influenced by cation concentration, ionic charge, ionic radius and hydration energy.

4.3.1. Mechanism

The adsorption behaviour of Ba^{2+} and La^{3+} on α-TiP was primarily governed by a surface-controlled proton–cation exchange mechanism. Experimental data presented in Section 4.2.5 revealed that the acidification observed in the equilibrium solutions could not be fully attributed to either surface deprotonation or residual acid contamination, indicating the presence of an additional proton source. This pointed to an additional source of proton release, which aligned with the proton displacement mechanism proposed by Sahu et al. [35]. In this mechanism, cations displace protons from phosphate groups exposed at the sorbent surface.

Sahu et al. [35] proposed for divalent Ba^{2+} a straightforward cation exchange mechanism where two protons are displaced from a single TiP unit, yielding a neutral framework and contributing two H^+ ions to the solution:

$$\mathrm{Ti(HPO_4)_2 \cdot H_2O + Ba^{2+}_{(aq)} \longrightarrow TiBa(PO_4)_2 \cdot H_2O + 2\,H^{+}_{(aq)}} \tag{4.1}$$

In contrast, for trivalent La^{3+}, a mechanism containing partial hydrolysis in solution due to its high charge density was proposed [35, 107], forming $LaOH^{2+}$ (Equation 4.2). This species then binds to phosphate groups on the TiP surface, displacing two protons (Equation 4.3). Because the hydrolysis step contributes an additional H^+ ion, the overall reaction results in a release of three protons per La^{3+} ion:

$$\mathrm{[La(H_2O)_9]^{3+} \longrightarrow [La(OH)(H_2O)_8]^{2+} + H^{+}} \tag{4.2}$$

$$\mathrm{Ti(HPO_4)_2 \cdot H_2O + [La(OH)(H_2O)_8]^{2+} \longrightarrow TiLa(OH)(PO_4)_2 \cdot 8\,H_2O + 2\,H^{+}} \tag{4.3}$$

$$\mathrm{Ti(HPO_4)_2 \cdot H_2O + La^{3+}_{(aq)} \longrightarrow TiLa(OH)(PO_4)_2 \cdot 8\,H_2O + 3\,H_{(aq)}{}^{+}} \tag{4.4}$$

However, in contrast to the mechanism proposed by Sahu et al. [35], bulk hydrolysis of La^{3+} is thermodynamically limited at pH < 4 [73], which reflects the entire equilibrium pH range in this study. Observations in Section 4.2.3, where increased La^{3+} concentrations did not decrease the pH of the equilibrium solution, suggested no further release of protons. Moreover, subsequential addition of La^{3+} in Section 4.2.4, resulted in a small pH drop of 0.12 units, which can be attributed to the intrinsic acidity of the $La(NO_3)_3$ stock solution and the larger number of occupied sites. A hydrolysis step would have pushed the pH more than 0.4 units lower. As a result, the three-proton release proposed by Sahu et al. [35] was not observed below pH 3 in this work.

Although the present data demonstrate that La^{3+} does not hydrolyse below pH 3, the exact surface complex that forms on TiP has not been resolved. A plausible interpretation, consistent with the observed pH and fast kinetics observed, is that La^{3+} binds bidentately to two PO^{-} groups [39, 64, 69]:

$$\mathrm{Ti(HPO_4)_2 \cdot H_2O + La^{3+}_{(aq)} \longrightarrow TiLa(PO_4)_2{}^{+} \cdot H_2O + 2\,H^{+}_{(aq)}} \tag{4.5}$$

In this proposed mechanism, the residual +1 charge is externally balanced by a Stern layer. Future spectroscopic work is required to confirm this mechanism. Both Ba^{2+} and La^{3+} interacted with TiP in a theoretical 1:1 molar ratio, with one cation binding per $Ti(HPO_4)_2 \cdot H_2O$ unit. However, the number of protons released into solution did not correspond directly to the charge of the adsorbed ion, as Sahu et al. [35] proposed.

4.3.1.1. Size exclusion

The experimental results in Section 4.2 supported a surface-dominated ion exchange process. As shown in Figure 4.13, the amorphous material exhibited consistently higher uptake of both La^{3+} and Ba^{2+} at pH > 2, compared to the crystalline material. In particular, the crystalline sorbents showed notably lower Ba^{2+} adsorption. This may suggested limited accessibility of binding sites. Furthermore, the deprotonation and surface saturation experiments confirmed that larger exposed surfaces in amorphous material facilitated greater proton release. These findings were consistent with the interpretation that larger surface area and unstructured structural morphology strongly enhance exchange capacity. This surface-limited behaviour suggested that internal ion exchange sites located in interlayer regions were not readily accessible to hydrated ions. To understand this restriction, structural insights from the literature are necessary.

Clearfield [108] and Chakraborty et al. [109] indicated that hydrated Ba^{2+}, due to its large ionic radius (Table 2.2), is too big to diffuse into the interlayer spaces of layered phosphates. Similarly, studies on α-ZrP, using Fourier Transform Infrared Spectroscopy (FTIR) by Zhang [39] and later on α-TiP by Shao et al. [69], demonstrate that La^{3+} adsorption occurs predominantly on the surface and not in the interlayer spaces

This surface-dominated exchange is attributed to the restricted access to the interlayer spaces. Llavona [40] determined that the effective interlayer spacing in α-ZrP allows only cations with diameters up to 2.61 Å to diffuse into the structure, considering the space occupied by interlayer water molecules. Given the structural similarities between α-ZrP and α-TiP, a comparable, or even narrower, size constraint is expected for α-TiP. This excludes hydrated Ba^{2+} (4.04 Å) and La^{3+} (4.52 Å) from intercalating, restricting their exchange to accessible surface hydroxyl groups. This interpretation aligned with the findings of Shao et al. [69], which report that crystalline α-TiP has the lowest ion exchange capacity for La^{3+} among the tested titanium phosphate phases.

To summarise, the ion exchange process in crystalline α-TiP was surface-dominated, as limited interlayer accessibility restricted ion exchange to external hydroxyl groups. As a result, the ion exchange capacity was strongly influenced by the surface area of the material. Smaller crystallites with a higher surface-to-volume ratio exposed more reactive sites, leading to a higher exchange capacity. These morphological differences may have affected equilibrium behaviour and increased apparent selectivity, as a larger fraction of the material actively participated in ion exchange. Moreover, because only surface sites were accessible, more than one TiP unit was effectively required per adsorbed ion, reducing the number of available protons per unit and lowering the practical exchange capacity relative to the theoretical stoichiometry.

4.3.1.2. Kinetics

The kinetics of ion exchange in α-TiP determined the rate at which Ba^{2+} and La^{3+} are adsorbed, which is a key parameter for practical separation applications. The equilibrium experiments (Section 4.2.2) provided insight into time-dependent uptake, indicating rapid adsorption within a short timeframe for the used concentrations in this study.

As shown in Figure 4.15a, TiP-I at pH ≈ 3 exhibited fast uptake of Ba^{2+} (35–40%) and La^{3+} (>95%) within 30 minutes. For La^{3+}, this equilibrium was maintained over 48 hours (Figure 4.15b), confirming rapid and sustained uptake. These results supported a surface-controlled ion exchange mechanism (Section 4.3.1), where exposed PO^- groups on the α-TiP surface enabled immediate ion binding without interlayer diffusion [69].

Shao et al. [69] reported similar fast kinetics for α-TiP at 1 mM La^{3+}, which followed a pseudo-second-order model based on measurements within the first 30 minutes. In this study, kinetic modelling was not performed due to the absence of sub-30-minute data. Nevertheless, the observed stabilisation within 30 minutes suggested similar adsorption kinetics over a broader pH range. While fast ion exchange kinetics are favourable for practical application in continuous systems, differences in kinetic behaviour between the lanthanum and barium ions could also be beneficial for optimal separation performance. At the concentrations tested in this study, both La^{3+} and Ba^{2+} appeared to reach adsorption equilibrium within 30 minutes, indicating that fast kinetics were maintained for both ions under conditions relevant to practical radionuclide separations.

4.3.2. Thermodynamics

Thermodynamic analysis of ion exchange in α-TiP clarifies the energetic driving forces behind Ba^{2+} and La^{3+} adsorption, complementing the experimental adsorption data. This section compares the partition coefficients from the adsorption experiments of TiP-I and TiP-III-1:10-ex (Table 4.9) with the calorimetric data from Airoldi and Nunes [72] (Table 4.10) to support the interpretation of the experimental results.

The experimental partition coefficients, visualised in Figure 4.14 for all sorbents and presented in Table 4.9 for TiP-I and TiP-III-1:10-ex revealed a consistent trend. Partition coefficients increased with pH, reflecting enhanced adsorption due to reduced proton competition. Moreover, the ratio between the partition coefficients was consistently larger than 1, supporting a stronger affinity of α-TiP for La^{3+}.

Table 4.9: Partition coefficients (K_D) for La^{3+} and Ba^{2+} ($C_{0,Ba^{2+}}$ = 1.5 mM) for different α-TiP materials at varying pH.

Sorbent	$C_{0,La^{3+}}$	$K_{D,Ba^{2+}}$	$K_{D,La^{3+}}$	**pH** ± σ (n = 3)	K_D **Ratio**
TiP-I	2.5 µM	9.1 ± 0.4	392 ± 12	3.08 ± 0.01	42 ± 2
	2.5 µM	13 ± 1	463 ± 28	3.07 ± 0.01	35 ± 4
	2.5 µM	3.5 ± 0.1	27 ± 1	2.16 ± 0.01	7.8 ± 0.4
	2.5 µM	0.46 ± 0.03	0.8 ± 0.2	1.08 ± 0.01	1.7 ± 0.5
	1.0 mM	5.8 ± 0.4	24 ± 2	3.07 ± 0.01	4.1 ± 0.5
TiP-III-1:10-ex	2.5 µM	13.2 ± 0.3	676 ± 23	2.90 ± 0.01	51 ± 2
	2.5 µM	11 ± 1	604 ± 39	2.94 ± 0.04	54 ± 6
	2.5 µM	4.8 ± 0.2	75.8 ± 0.4	2.17 ± 0.01	15.8 ± 0.8
	2.5 µM	0.50 ± 0.07	1.2 ± 0.1	1.08 ± 0	2.5 ± 0.4
	1.0 mM	5.56 ± 0.02	42.2 ± 0.9	2.92 ± 0.02	7.6 ± 0.2

This observation aligned with the thermodynamic data reported by Airoldi and Nunes [72], which showed a more negative ΔG and higher K_{thermo} for La^{3+} than for Ba^{2+} exchange. The study reported thermodynamic parameters for the individual ion exchange of Ba^{2+} and La^{3+} in α-TiP (denoted in their study as TPH), presented in Table 4.10.

It is important to distinguish between K_D and K_{thermo}, as they represent fundamentally different concepts. The partition coefficient K_D is an experimental parameter that quantifies how ions partition between the solid and liquid phases under specific experimental conditions, such as pH, concentration and the presence of competing ions. In contrast, K_{thermo} is a thermodynamic equilibrium constant derived from the Gibbs free energy change, representing the intrinsic ion exchange favourability under standard-state conditions. Although their absolute values are not directly comparable, the consistent trends confirmed that experimental observations were qualitatively consistent with thermodynamic predictions.

Using the thermodynamic data, the equilibrium constants $K_{thermo,Ba}$ and $K_{thermo,La}$ were calculated from Equation 2.1 to be 2,040 and 617,208, respectively, at ambient temperature (298.15 K). The much larger K_{thermo} for La^{3+} supported its stronger binding affinity to α-TiP, in agreement with the experimental adsorption data.

Table 4.10: Calculated calorimetric data of α-TiP during ion exchange with Ba^{2+} and La^{3+} at 298.15 K [72].

Cation	$\Delta_{exch}H$ **[kJ mol^{-1}]**	$-\Delta G$ **[kJ mol^{-1}]**	ΔS **[J mol^{-1} K^{-1}]**	K_{thermo}
Ba^{2+}	1.51 ± 0.09	18.89 ± 0.05	68 ± 1	2040
La^{3+}	7.0 ± 0.1	33.1 ± 0.3	134 ± 1	617208

The results indicated that both ion exchange processes are endothermic, as shown by the positive values of $\Delta_{exch}H$ (1.51 kJ mol^{-1} for Ba^{2+} and 7.00 kJ mol^{-1} for La^{3+}). This indicates that energy is required to facilitate the binding of the cations to the exchanger, due to the disruption of hydrogen bonding or deprotonation of hydroxyl groups. The higher enthalpy for La^{3+} reflects its stronger bound hydration shell, which demands more energy to break during exchange.

Despite this energetic input, the process is compensated by a significant entropy gain, as reflected in the positive ΔS values (68 and 134 J mol^{-1} K^{-1} for Ba^{2+} and La^{3+} respectively). The positive ΔS values reflect partial dehydration of the ions, with water release increasing disorder. The higher entropy gain for La^{3+} arises from its stronger hydration shell due to its higher charge density.

The Gibbs free energy change (ΔG) for both Ba^{2+} (–18.89 kJ mol^{-1}) and La^{3+} (–33.05 kJ mol^{-1}) is substantially negative, confirming that ion exchange is spontaneous under the studied conditions. The

greater magnitude of ΔG and ΔS for La^{3+} indicates a more favourable, entropy-driven exchange process. Overall, the thermodynamic parameters highlight how the balance between enthalpy and entropy governs the selectivity of α-TiP for La^{3+} over Ba^{2+}.

This thermodynamic preference was further supported by the adsorption results at elevated La^{3+} concentrations (Section 4.2.3). When La^{3+} was present at 1.0 mM, comparable to the 1.5 mM Ba^{2+}, its partition coefficient remained higher, as shown in Table 4.9. This indicated that even under competitive conditions, the intrinsic selectivity of α-TiP for La^{3+} prevails, in line with its lower ΔG and larger K_{thermo}.

4.3.2.1. Validity of reference thermodynamic data

The thermodynamic data reported by Airoldi and Nunes [72] were obtained at 298.15 K using isothermal microcalorimetry. Since the adsorption experiments in this study were also conducted under isothermal ambient conditions, their values were applicable. Minor temperature differences were not expected to introduce significant discrepancies.

The calorimetric parameters were derived from single-ion systems, where only Ba^{2+} or La^{3+} was present. In contrast, this study investigates competitive conditions, with both ions present simultaneously. While the calorimetric data could not predict absolute adsorption behaviour under such conditions, they remained valuable for interpreting relative trends in selectivity, binding strength and thermodynamic driving forces. The substantial differences in ΔG and ΔS between Ba^{2+} and La^{3+} explained the experimentally observed preference for multivalent ion uptake.

The calorimetric titrations were performed over a concentration range of 1.0×10^{-3} to 0.20 mol/L. The Ba^{2+} concentration used in this study (1.5 mM) lay within this range, which made the data directly applicable. Although the La^{3+} concentration (2.5 µM) was below the reported range, the calorimetric results still offer qualitative insight. At very low concentrations, deviations from average thermodynamic behaviour may have occurred due to partial site occupancy or reduced ion-ion interactions. Nonetheless, because the reported parameters represent equilibrium-averaged values across a broad concentration range, they remained valid for comparative purposes.

In a competitive system like the one used in this study, with a high excess of Ba^{2+} (1.5 mM) and a low concentration of La^{3+} (2.5 µM), both ions were expected to compete for the same exchange sites on the TiP surface, as discussed in Section 4.2.4. Despite the lower concentration of La^{3+}, its higher charge and more favourable overall Gibbs free energy of exchange contributed to its selective uptake. While the excess Ba^{2+} could have limited available sites, the thermodynamic preference for La^{3+} appeared strong enough to enable substantial adsorption, as observed experimentally. This reflected a balance between concentration-driven site competition and intrinsic affinity differences between the ions.

It is important to note that the calorimetric data from Airoldi and Nunes [72] were obtained at a different pH (3-4.5), which might not have matched the pH conditions in the adsorption experiments of this study. Since proton concentration directly affects ion exchange equilibria in proton–cation systems, deviations in pH could lead to significant differences in observed adsorption behaviour. While the reported thermodynamic parameters reflect unspecified pH conditions and were useful for indicating general trends in ion affinity, they could not be directly extrapolated across all pH values. Nonetheless, the observed preferential uptake of La^{3+} in this study remained consistent with its more favourable thermodynamic profile.

4.3.3. Langmuir adsorption model

As discussed in Section D.1, Appendix D, and demonstrated by Shao et al. [69], the adsorption of Ba^{2+} and La^{3+} could be described by the Langmuir adsorption model. The dataset obtained in this study for the various TiP materials contained data points for varying pH at a fixed C_0, while for fitting a Langmuir isotherm, results for varying C_0 were needed at a fixed pH. Thus, accurate fitting of Equation D.1 was

not possible. As a result, the Langmuir equilibrium constant (K_{Lang}) for individual ions could not be reliably determined.

Furthermore, the experimental conditions in this study involved a competitive adsorption system, as described in Section D.1.1, in which Ba^{2+}, La^{3+} and H^{+} ions compete for the same binding sites on the sorbent surface. In such systems, the single-component Langmuir model is no longer sufficient. Instead, a multicomponent extension of the Langmuir model is applicable, in which each species has its affinity constant (K_M) and the fractional site occupancy (q_m) depends on the relative concentrations and binding affinities of all ions present.

The fitting of this Langmuir model (Equation D.2) did, in the case of a proton competition system, need experimental data at varying concentrations and pH (to vary H^{+} concentration). Although measurements at elevated La^{3+} concentrations and varying pH were performed, the dataset remained limited. The fitting, therefore, should be interpreted with caution since the system was under-defined due to the limited data points. This means that there were insufficient constraints (data points) to fit a unique set of model parameters (K_M and q_m) outcomes. Consequently, the non-linear system yielded multiple solutions, as multiple parameter sets adequately fit the input data. These non-unique solutions prevented validation of the results and therefore could not be used as quantitative evidence for ion affinity or sorption capacity in this study. The results of the fitting are presented and analysed in Section D.2, Appendix D.

4.4. Comparison with literature

To assess the performance and reproducibility of the synthesised materials, the results of this study were compared to studies by Spruit [38] and Brown [27] in Section 4.4.1 and Section 4.4.2 respectively. These comparisons help to evaluate the performance of TiP against other sorbents.

4.4.1. Comparison with Spruit

The selectivity and adsorption performance of the synthesised TiP materials were compared with results reported by Spruit [38], who studied pH-dependent adsorption of Ba^{2+} and La^{3+} on α-TiP and α-ZrP. A direct comparison of the adsorption results was justified because the experimental conditions used in both studies were nearly identical. Most importantly, both experiments employed the same ion concentrations for the Ba/La mixture and used an equal mass of sorbent (0.05 g). Additionally, the experimental procedures, including contact time and measurement methods using the Wallac gamma counter, were consistently applied. This alignment ensured that any observed differences in adsorption behaviour can be attributed to material properties rather than experimental variability, making the results valid for direct comparison of the selectivity and performance of the TiP materials investigated in this study.

4.4.1.1. α-TiP comparison

Spruit [38] synthesised α-TiP according to method I. The synthesis yielded crystalline, hexagonal, flat crystallites ranging from 1 to 5 µm, consistent with the results in this study. Analysis using Highscore determined a small TiO_2 contamination of 4%, similar to the 6% in this study. The results of the adsorption experiment were plotted in Figure 4.16a, together with the adsorption results for TiP-I and TiP-III-1:10-ex.

The results showed similar performance regarding the adsorption of La^{3+} ions. However, the TiP synthesised by Spruit (referred to as TiP-S) had slightly lower adsorption for Ba^{2+} ions. This suggested the material synthesised by Spruit demonstrated slightly better selectivity at pH ≈ 3 by a greater separation window. Given that the goal of this separation process was to selectively remove La^{3+} while leaving Ba^{2+} in solution, the relative uptake of both ions was a critical factor.

Nonetheless, the observed differences in Ba^{2+} uptake were relatively small and could also be attributed to differences in batch properties between the synthesised TiP materials, influencing the crystallite size.

Considering the close agreement in overall trends and data points, it is reasonable to conclude that the materials exhibit largely comparable adsorption behaviour under the tested conditions. Given the strong agreement, the reproducibility of the synthesis method I and the α-TiP adsorption behaviour across different studies can be confirmed.

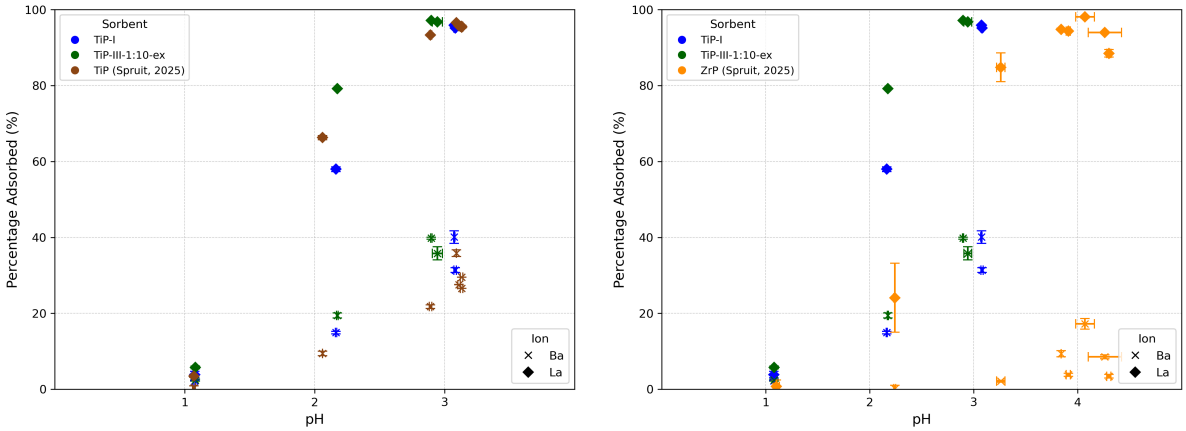

(a) vs. TiP by Spruit [38]

(b) vs. ZrP by Spruit [38]

Figure 4.16: Effect of equilibrium pH on Ba^{2+} (C_0 = 1.5 mM) and La^{3+} (C_0 = 2.5 µM) uptake on TiP-I, TiP-III-1:10-ex and the materials synthesised by Spruit [38] (batch tests, 0.05 g sorbent, 20 °C).

4.4.1.2. α-ZrP comparison

As discussed in Section 2.3.1, α-TiP is isostructural with α-ZrP. Spruit [38] successfully synthesised α-ZrP (from here ZrP-S) according to Alberti and Torracca [110]. This synthesis yielded highly crystalline crystallites in the 10 to 50 µm range, with a measurable thickness between 1 and 5 µm. Since ZrP-S crystallites are larger crystallites with measurable thickness, their surface-to-volume ratio is smaller. This, and to a lesser extent the higher molecular weight of ZrP (301 vs. 258 g/mol), results in significantly fewer accessible hydroxyl groups per sorbent mass.

The results of the adsorption experiment are plotted in Figure 4.16b, together with the adsorption results for TiP-I and TiP-III-1:10-ex of this study. The most notable difference was the different pH behaviour. While the pH in the adsorption experiments of this study shifted toward pH 3, the systems using ZrP-S shifted toward pH 4. In this range, ZrP maintains a high uptake of La^{3+} while exhibiting a remarkably low uptake of Ba^{2+} ions. This distinct adsorption behaviour indicated a significantly better selectivity performance of ZrP-S than both for TiP materials tested in this study. Since separation was the primary objective, the ability of the ZrP-S to strongly favour La^{3+} adsorption while excluding Ba^{2+} is a critical advantage.

However, the advantage may have stemmed from the larger crystallite size and the associated reduction in accessible surface hydroxyl groups. Nonetheless, differences in intrinsic cation affinity or ion exchange kinetics, as Spruit did not confirm equilibrium, between ZrP and TiP could also have contributed to the enhanced selectivity. The shift in pH towards 4 instead of 3 was likely caused by reduced deprotonation, as fewer hydroxyl groups were present on the surface due to a lower surface-to-volume ratio. This suggested that fewer adsorption sites were available.

Supporting this, Spruit [38] conducted a surface saturation experiment using ZrP-S, where the La^{3+} concentrations were elevated from 2.5 µM to 1.0 mM, similarly to the surface saturation experiments in this study. In these experiments, conducted at pH ≈ 4, the Ba^{2+} and La^{3+} uptake was 2.0 ± 0.4% and 9 ± 2% respectively. In the study of Spruit, La^{3+} adsorption remained stable for 48 hours, and Ba^{2+} adsorption was stable for at least 6 hours before becoming unmeasurable due to the short half-life of

^{139}Ba, supporting the assumption that adsorption equilibrium had been reached in the experiment at elevated La^{3+} concentration.

This adsorption is significantly lower than the 54 ± 2% and 67.9 ± 0.2% for La^{3+} and 22 ± 1% and 21.8 ± 0.2% for Ba^{2+} to TiP-I and TiP-III-1:10-ex respectively, as presented in Table 4.6. This low uptake indicated further that the uptake is limited due to less accessible PO^- groups of ZrP-S. Given that α-TiP and α-ZrP are isostructural and possess nearly identical phosphate chemistry, the markedly different uptake behaviour could have stemmed more from morphological differences than from intrinsic chemical affinity.

In summary, although ZrP-S exhibited better separation of Ba^{2+} and La^{3+}, its significantly lower uptake capacity suggested that this advantage was not caused by superior sorbent chemistry, but from a reduced number of accessible surface exchange sites due to its larger particle size and lower surface-to-volume ratio. The lower degree of deprotonation and reduced availability of PO^- groups at the surface were consistent with this interpretation, although further investigation would be required to confirm whether morphology rather than chemistry drives the observed selectivity.

4.4.2. Comparison with Brown

To place the performance of the TiP and ZrP materials in a broader context, results were compared with those reported by Brown [27], who investigated the separation behaviour of metal oxide sorbents using Ba and La as analogues for Ra and Ac. In that study, partition coefficients were determined for alumina, titania and zirconia over a pH range of 3 to 7. While these metal oxides differ structurally from layered phosphates, their reported K_D trends provided a relevant comparison for the separation performance.

To enable a direct qualitative comparison, the results of the present study have also been expressed in terms of the partition coefficient and are plotted alongside data by Brown in Figure 4.17.

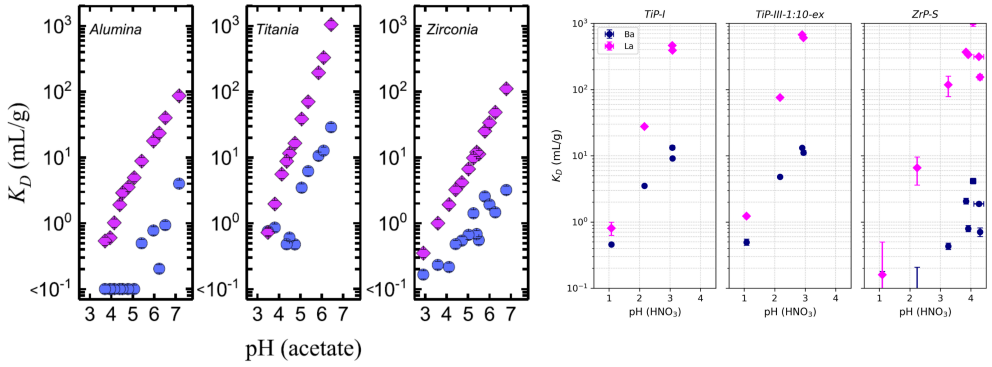

Figure 4.17: Partition coefficients (K_D) for Ba^{2+} (C_0 = 0.9 mM) and La^{3+} (C_0 = 0.5 mM) adsorption on alumina, titania and zirconia as reported by Brown [27] Ba^{2+} (left) and partition coefficients for Ba^{2+} (C_0 = 1.5 mM) and La^{3+} (C_0 = 2.5 µM) adsorption on TiP-I, TiP-III-1:10-ex and ZrP-S at varying equilibrium pH values (right).

Several limitations must be considered when comparing the results of this study with those reported by Brown [27]. First, the experimental conditions varied significantly. This study focuses on highly acidic environments with pH values between 1 and 3, while the experiments by Brown were conducted in neutral to mildly acidic conditions between pH 3 and 7. In that study, mildly acidic conditions were maintained using an acetate buffer system, stabilising the pH. Second, the La^{3+} concentration used by Brown was 0.5 mM, which is substantially higher than the 2.5 µM used in this study. This difference may have shifted the adsorption equilibrium and influenced the kinetics of ion uptake. Third, Brown provided surface area for the sorbents used, which were 205, 100 and 30 m^2/g for alumina, titania and

zirconia, respectively. In contrast, no surface area or site capacity measurements were performed in this study, which limits the ability to assess the density of reactive sites available for ion exchange.

Because site capacity and ion concentration were identified in this study as key factors influencing adsorption, a direct comparison with the results of Brown was not valid. The comparison should therefore be considered qualitative rather than quantitative.

Despite the differences in methodology, both studies presented comparable trends. Both the metal oxides and layered phosphates had a higher affinity with La^{3+} than Ba^{2+} across the entire pH range. Additionally, for both systems, the ions competed with protons. Notably, the pH-dependent adsorption slopes over the pH range were steeper for both Ba^{2+} and La^{3+} on titania and TiP compared to zirconia and ZrP. This suggested that a chemical difference between titanium- and zirconium-based materials influences their ion adsorption behaviour. However, as in this study, the surface-to-volume ratios of the materials investigated by Brown also differed significantly, which complicated direct quantitative comparisons. This made it unclear whether the observed differences were due to chemical properties or to morphological factors such as active surface sites.

Further research under comparable ion concentrations, surface-to-volume ratios, and standardised conditions would be necessary to confirm whether the observed differences in adsorption behaviour are indeed attributable to the chemical nature of titanium versus zirconium, rather than differences in surface area or experimental setup.

4.5. Practical application

This study has provided a detailed characterisation of the ion exchange behaviour of α-TiP. To explore the practical relevance of these findings, this section introduces a clinical scenario involving the separation of medically relevant actinium-225 from radium-226 in Section 4.5.1, followed by an evaluation of the material design criteria required for successful implementation in Section 4.5.2.

4.5.1. Large-scale separation scenarios

As introduced in Chapter 1, this study was initially intended to evaluate whether α-TiP is a suitable material for separating actinium, produced via the $^{226}Ra(p, 2n)^{225}Ac$ reaction, from radium. The experiments were designed to mimic an production scenario in which 10 mg of solid ^{226}Ra is irradiated to approximately 1 Ci (37 GBq) of ^{225}Ac [27], an sufficient amount for 2000-5000 patient doses [111, 112].

In this production route, a cyclotron accelerates protons to 15–20 MeV at a current of 500 µA. These protons are directed onto a thin, actively cooled ^{226}Ra target. After irradiation, the target is dissolved in an acidic solution, releasing both the unconverted ^{226}Ra and the newly formed ^{225}Ac. At the activity level described above, the concentration of ^{225}Ac is in the micromolar range, meaning it is present only in trace amounts compared to the millimolar concentrations of unconverted ^{226}Ra. In this study, the analogue concentrations were set to 2.5 µM La^{3+} and 1.5 mM Ba^{2+}, resulting in a La:Ba ratio of 1:600. The chosen 2.5 µM La^{3+} lies within the low-micromolar range expected for ^{225}Ac in a 10–100 mL dissolution volume and is high enough for reliable detection, while reflecting a realistic Ra/Ac ion-competition environment. The trace amounts of actinium-225 highlight the need for sorbents with high selectivity, rather than high capacity to efficiently isolate ^{225}Ac from a bulk of chemically similar radium ions [113].

The materials investigated in this study showed promising results for the separation of La^{3+} and Ba^{2+}, and are therefore of interest for further investigation as sorbents for the separation of ^{225}Ac from ^{226}Ra in cyclotron-based production routes. Given that ^{225}Ac is present only in trace amounts while ^{226}Ra remains in significant excess, high selectivity is essential. The selectivity of α-TiP was demonstrated by differences in adsorption percentages in both the standard experiments and those using elevated La^{3+} concentrations. The following section discusses the material and system criteria required for effective implementation at clinical scale.

4.5.2. Design criteria

This section outlines the design criteria for separating ^{225}Ac and ^{226}Ra in medical radionuclide production, focusing on the suitability of the materials examined in this study.

4.5.2.1. General material properties

The primary requirement for the separation material is a strong selectivity for ^{225}Ac over ^{226}Ra, achieved through a clear affinity difference. In this study, α-TiP demonstrated such behaviour under acidic conditions, showing high uptake of La^{3+} (a chemical analogue for ^{225}Ac) and significantly lower uptake of Ba^{2+} (representing ^{226}Ra). The ion-specific preference for this ion pair and results from other studies [35, 39, 40] reflected the ability of the material to discriminate between cation valences and is essential for achieving efficient separation.

Equally important is reversibility, the ability to recover ^{225}Ac from the sorbent using an acidic eluent. While this study shows that low pH promotes competition between protons and metal ions, facilitating ion release, the efficiency of ^{225}Ac recovery was not investigated. Future research should quantify recovery rates to determine whether the material enables practical radionuclide isolation for medical applications. The suppressed adsorption of La^{3+} and Ba^{2+} observed at pH ≈ 1 suggests that proton competition at low pH may facilitate desorption, supporting the potential reversibility of the ion exchange process.

For clinical application, the sorbent must maintain structural integrity under high radiation doses and prolonged exposure to acidic media. This study did not evaluate the chemical or radiation stability of the materials. Although previous research reports promising performance under such conditions [30, 37, 38, 39, 91], these findings require validation for the specific case of α-particle irradiation. In contrast to the gamma-emitting isotopes used in this study (^{140}La and ^{139}Ba), both ^{225}Ac and ^{226}Ra emit alpha particles, which are more likely to induce radiolysis and degrade material over time. Experimental testing under alpha-emitting conditions is therefore essential to confirm long-term stability and practical feasibility.

4.5.2.2. System and column design

This study evaluated sorption performance in batch systems using La^{3+} and Ba^{2+} as chemical analogues for ^{225}Ac and ^{226}Ra, respectively. To determine the applicability of these findings to large-scale separations, future work must first verify that ^{225}Ac and ^{226}Ra exhibit comparable adsorption behaviour on the synthesised materials. If this is confirmed, dynamic column experiments are required to evaluate sorbent performance under flow conditions, which better represent large-scale use.

Although both TiP and ZrP exhibited selective ion exchange, achieving the high purity standards required for medical applications likely demands a multi-stage separation process. This study showed that ion concentrations and the number of accessible surface phosphate groups strongly influence separation performance. Therefore, a single sorbent system may not achieve sufficient discrimination under all process conditions. Connecting multiple columns with the same sorbent, but with distinct particle sizes, could exploit the differences in available hydroxyl sites by progressively enhancing purity across stages. To design such a system, broader studies must be conducted to map how concentration-dependent behaviour and surface accessibility influence performance.

This study and literature [69] demonstrated fast ion exchange kinetics for TiP, with equilibrium reached within 30 minutes. Comparable behaviour is reported for ZrP in previous studies [38, 39], supporting their potential suitability for dynamic column systems. If similar kinetic profiles are confirmed for ^{225}Ac and ^{226}Ra, short residence times would still allow effective separation, facilitating higher throughput in dynamic systems. Fast ion exchange kinetics reduce the sensitivity to particle size, allowing the use of larger sorbent particles to lower pressure drop while maintaining acceptable adsorption performance. As discussed in Section 4.4.1, larger particles (10–50 µm) were associated with improved selectivity at

the tested concentrations, although this may vary across the concentration range. The rapid adsorption kinetics observed here suggest minimal kinetic limitations, allowing trade-offs to prioritise selectivity and hydraulic performance.

In this study, it was tried to increase the crystallite size of α-TiP by extending the refluxing time (72 hours and 14 days) and increasing the synthesis temperature (170°C) of the synthesis method II. Prolonged synthesis time, however, did not result in larger crystallites compared to the standard method. Increasing the temperature led to the formation of γ-TiP, having a less ordered morphology, rather than promoting crystallite growth of the desired α-phase. These outcomes highlight the limitations of conventional hydrothermal tuning for size control in this method. Future research into controlled crystallite growth of phase-pure α-TiP would benefit its applicability in column systems.

4.5.2.3. Ion exchange material

Until further research proposed in this section is conducted, the ZrP-S, synthesised and tested by Spruit [38] is the most suitable candidate for the separation of ^{225}Ac and ^{226}Ra, provided that its adsorption behaviour towards actinium and radium mirrors that observed for lanthanum and barium.

This was concluded based on two main findings. First, its high selectivity in the relevant pH window for La^{3+} over Ba^{2+} enables efficient separation of these ions under weakly acidic conditions. This was confirmed by high La^{3+} uptake, while Ba^{2+} uptake remained sub 10% at pH ≈ 4. In a practical separation context, this reduces the number of downstream purification steps or sequential columns required to meet high-purity standards. Under dynamic column conditions, this high selectivity could lead to sharper elution profiles, as Ba^{2+} would elute early with minimal retention, while La^{3+} would be strongly retained and elute in a narrower, well-defined peak. This improves resolution and reduces overlap, enhancing overall process efficiency.

Second, the large crystallite size of ZrP-S (10–50 µm) offers clear advantages for packed column operation. Larger particles reduce the hydraulic resistance of the columns, allowing higher flow rates at lower pressure drops. In this study and in related work [38, 39, 69], ion exchange was shown to be surface-controlled, with fast kinetics and no apparent diffusion limitations. Therefore, using larger particles would not significantly compromise adsorption performance, enabling efficient separation even under short residence times in dynamic column systems.

However, a fair comparison between TiP and ZrP can only be made when both materials are synthesised with similar properties. As demonstrated in this study, ion exchange performance is dominated by surface accessibility and the total number of available phosphate groups. Differences in uptake and selectivity may therefore arise not from the chemical nature of titanium versus zirconium, but from disparities in surface area and active site density. To determine whether intrinsic affinity plays a meaningful role, future studies must disconnect morphological effects from chemical properties through carefully controlled conditions and quantification of site accessibility.

5
Conclusion

This study investigated the suitability of α-Ti$(HPO_4)_2 \cdot H_2O$ (α-TiP) as a selective ion exchanger for the separation of lanthanum and barium as analogues for actinium and radium. Three synthesis methods were developed, and the resulting materials were characterised and evaluated for their separation performance. Batch adsorption experiments were conducted to assess ion uptake behaviour. The experimental results are consistent with the theoretical adsorption mechanism, providing a basis for the observed selectivity and separation efficiency.

The three synthesis methods employed titanium oxide (method I), titanium powder (method II), and titanyl sulfate (method III) as precursors. Method I produced highly crystalline α-TiP with 1–5 µm crystallites but suffered from residual TiO_2 precursor contamination. Method II yielded purer α-TiP with similar crystallite size and morphology. Method III initially formed amorphous titanium phosphate, which crystallised into nanoscale (200–500 nm) α-TiP upon extended refluxing. XRD, SEM and EDS analyses confirmed the crystallinity, morphology and compositional homogeneity of all materials.

Batch adsorption experiments using application-relevant concentrations ($[La^{3+}]$ = 2.5 µM and $[Ba^{2+}]$ = 1.0 mM) revealed that α-TiP preferentially binds La^{3+} over Ba^{2+} across the pH range of 1 to 3. La^{3+} uptake exceeded 95%, while Ba^{2+} uptake remained between 35% and 40% at pH ≈ 3. The selectivity persisted even at elevated La^{3+} concentrations (1.0 mM), confirming that α-TiP can discriminate effectively between trivalent lanthanum and divalent barium cations. Moreover, α-TiP showed fast ion exchange kinetics and reproducible and effective synthesis, validating its potential as a viable candidate for isolating actinium from a radium matrix.

Analysis of the ion exchange mechanism indicated that differences in accessible surface binding sites originating from different surface-to-volume ratios are inherently linked to separation performance.

Comparative analysis with isostructural α-Zr$(HPO_4)_2 \cdot H_2O$ (α-ZrP) showed that ZrP exhibited higher selectivity under similar conditions. However, this difference is likely to be attributed to variations in surface area and particle morphology rather than intrinsic chemical affinity of TiP versus ZrP.

In summary, this study demonstrated that α-TiP can be synthesised with tunable morphologies using different precursors and exhibits strong selectivity toward lanthanum over barium ions in acidic environments. These findings support its use as a potential separation medium for actinium–radium systems. However, further optimisation and experimental validation are necessary to confirm its clinical applicability.

6
Recommendations

Based on the findings and limitations discussed in this study, several recommendations can be made to improve the understanding, validation and practical application of α-TiP as a separation material for radionuclides. The following suggestions aim to guide future research efforts toward optimising material performance, validating selectivity with ^{225}Ac and ^{226}Ra and transitioning from laboratory-scale experiments to clinical implementation.

- To determine whether the differences in selectivity between α-TiP and α-ZrP are due to chemical composition rather than morphology, adsorption experiments should be repeated using samples with a similar amount of accessible surface binding sites and crystallite size. Quantifying site capacities under these controlled conditions will allow a direct comparison of their intrinsic ion exchange properties.

- To accurately determine site capacity and enable proper Langmuir model fitting, further adsorption experiments should be performed across a broader concentration range for both Ba^{2+} and La^{3+} ions.

- Future work should confirm whether the observed selectivity of α-TiP for La^{3+} over Ba^{2+} holds for the actual separation of ^{225}Ac and ^{226}Ra. Experiments with the latter isotopes are necessary to verify that the analogues used in this study provide an accurate representation of separation behaviour.

- Although this study assumes chemical and radiological stability of α-TiP, these properties have not been experimentally validated. The performance of α-TiP should be assessed after exposure to ^{225}Ac and ^{226}Ra, as well as under highly acidic conditions, to evaluate potential degradation or loss in capacity. To test radiochemical stability, α-TiP should be suspended in 1 M HCl and irradiated with 10 MeV electron beams up to 2 MGy, followed by XRD and SEM analysis to identify structural or morphological changes [56]. To test chemical stability, elemental leaching can be quantified by ICP-MS.

- As all experiments in this study were conducted in batch mode, dynamic column experiments are needed to translate the findings into a scalable process. Breakthrough curve analysis should be conducted by continuously flowing a feed solution through a fixed-bed column and monitoring the effluent concentration over time to determine dynamic capacity and selectivity. Flow rate optimisation involves varying the velocity to assess mass transfer limitations and prevent channelling. Multi-stage separation should be simulated using serially connected columns to replicate clinical purification systems and evaluate performance under realistic loading and elution conditions.

- Further optimisation of the synthesis process is advised to control particle morphology and grow crystallites to dimensions suitable for column operation. Lowering precursor concentrations and adjusting pH may reduce nucleation rates, allowing for slower, uniform growth. Potentially producing larger and monodisperse particles.

Bibliography

[1] World Health Organization. *Global Health Estimates 2020: Deaths by Cause, Age, Sex, by Country and by Region, 2000–2019*. Accessed: 2024-12-11. 2020. URL: https://www.who.int/data/gho/data/themes/mortality-and-global-health-estimates/ghe-leading-causes-of-death.

[2] Hyuna Sung et al. "Global Cancer Statistics 2020: GLOBOCAN Estimates of Incidence and Mortality Worldwide for 36 Cancers in 185 Countries". In: *CA A Cancer Journal for Clinicians* 71.3 (Feb. 2021), pp. 209–249. DOI: 10.3322/caac.21660. URL: https://doi.org/10.3322/caac.21660.

[3] Viswanadha Vijaya Padma. "An overview of targeted cancer therapy". In: *Biomedicine* 5.4 (Nov. 2015). DOI: 10.7603/s40681-015-0019-4. URL: https://doi.org/10.7603/s40681-015-0019-4.

[4] David E Gerber. "Targeted therapies: a new generation of cancer treatments". In: *American family physician* 77.3 (2008), pp. 311–319.

[5] A. Urruticoechea et al. "Recent Advances in Cancer therapy: An Overview". In: *Current Pharmaceutical Design* 16.1 (Nov. 2009), pp. 3–10. DOI: 10.2174/138161210789941847. URL: https://doi.org/10.2174/138161210789941847.

[6] Rajamanickam Baskar et al. "Cancer and Radiation Therapy: Current Advances and Future Directions". In: *International Journal of Medical Sciences* 9.3 (Jan. 2012), pp. 193–199. DOI: 10.7150/ijms.3635. URL: https://doi.org/10.7150/ijms.3635.

[7] Jean-Pierre Pouget et al. "Introduction to Radiobiology of Targeted Radionuclide Therapy". In: *Frontiers in Medicine* 2 (Mar. 2015). DOI: 10.3389/fmed.2015.00012. URL: https://doi.org/10.3389/fmed.2015.00012.

[8] Devrim Ersahin, Indukala Doddamane, and David Cheng. "Targeted radionuclide therapy". In: *Cancers* 3.4 (Oct. 2011), pp. 3838–3855. DOI: 10.3390/cancers3043838. URL: https://doi.org/10.3390/cancers3043838.

[9] Adina Elena Stanciu. "Radionuclides in targeted therapy of cancer". In: *Rev Roum Chim* 57.1 (2012), pp. 5–13.

[10] Lawrence E. Williams, Gerald L. DeNardo, and Ruby F. Meredith. "Targeted radionuclide therapy". In: *Medical Physics* 35.7Part1 (June 2008), pp. 3062–3068. DOI: 10.1118/1.2938520. URL: https://doi.org/10.1118/1.2938520.

[11] Maria Hassan et al. "A review of recent advancements in Actinium-225 labeled compounds and biomolecules for therapeutic purposes". In: *Chemical Biology Drug Design* 102.5 (Sept. 2023), pp. 1276–1292. DOI: 10.1111/cbdd.14311. URL: https://doi.org/10.1111/cbdd.14311.

[12] Young-Seung Kim and Martin W Brechbiel. "An overview of targeted alpha therapy". In: *Tumor biology* 33 (2012), pp. 573–590.

[13] Deeksha Dhiman, Rakhee Vatsa, and Ashwani Sood. "Challenges and opportunities in developing Actinium-225 radiopharmaceuticals". In: *Nuclear Medicine Communications* 43.9 (June 2022), pp. 970–977. DOI: 10.1097/mnm.0000000000001594. URL: https://doi.org/10.1097/mnm.0000000000001594.

[14] Firas Mourtada et al. "Actinium-225 targeted agents: Where are we now?" In: *Brachytherapy* 22.6 (Sept. 2023), pp. 697–708. DOI: 10.1016/j.brachy.2023.06.228. URL: https://doi.org/10.1016/j.brachy.2023.06.228.

[15] S. Pommé et al. “Measurement of the 225Ac half-life”. In: *Applied Radiation and Isotopes* 70.11 (July 2012), pp. 2608–2614. DOI: 10.1016/j.apradiso.2012.07.014. URL: https://doi.org/10.1016/j.apradiso.2012.07.014.

[16] Michael R. McDevitt et al. “Tumor Therapy with Targeted Atomic Nanogenerators”. In: *Science* 294.5546 (Nov. 2001), pp. 1537–1540. DOI: 10.1126/science.1064126. URL: https://doi.org/10.1126/science.1064126.

[17] M. W. Geerlings et al. “The feasibility of 225 Ac as a source of alpha-particles in radioimmunotherapy”. In: *Nuclear Medicine Communications* 14.2 (Feb. 1993), pp. 121–125. DOI: 10.1097/00006231-199302000-00009. URL: https://doi.org/10.1097/00006231-199302000-00009.

[18] L. Koch et al. “Production of AC-225 and application of the BI-213 daughter in cancer therapy”. In: *Czechoslovak Journal of Physics* 49.S1 (Jan. 1999), pp. 817–822. DOI: 10.1007/s10582-999-1001-8. URL: https://doi.org/10.1007/s10582-999-1001-8.

[19] Randy Perron, Denise Gendron, and Patrick W. Causey. “Construction of a thorium/actinium generator at the Canadian Nuclear Laboratories”. In: *Applied Radiation and Isotopes* 164 (June 2020), p. 109262. DOI: 10.1016/j.apradiso.2020.109262. URL: https://doi.org/10.1016/j.apradiso.2020.109262.

[20] O. D. Maslov, A. V. Sabel’nikov, and S. N. Dmitriev. “Preparation of 225Ac by 226Ra(γ, n) photonuclear reaction on an electron accelerator, MT-25 microtron”. In: *Radiochemistry* 48.2 (Mar. 2006), pp. 195–197. DOI: 10.1134/s1066362206020184. URL: https://doi.org/10.1134/s1066362206020184.

[21] G. Melville et al. “Production of Ac-225 for cancer therapy by photon-induced transmutation of Ra-226”. In: *Applied Radiation and Isotopes* 65.9 (Apr. 2007), pp. 1014–1022. DOI: 10.1016/j.apradiso.2007.03.018. URL: https://doi.org/10.1016/j.apradiso.2007.03.018.

[22] C. Apostolidis et al. “Cyclotron production of Ac-225 for targeted alpha therapy”. In: *Applied Radiation and Isotopes* 62.3 (Sept. 2004), pp. 383–387. DOI: 10.1016/j.apradiso.2004.06.013. URL: https://doi.org/10.1016/j.apradiso.2004.06.013.

[23] Graeme Melville and Barry J Allen. “Cyclotron and linac production of Ac-225”. In: *Applied Radiation and Isotopes* 67.4 (Dec. 2008), pp. 549–555. DOI: 10.1016/j.apradiso.2008.11.012. URL: https://doi.org/10.1016/j.apradiso.2008.11.012.

[24] R. A. Aliev et al. “Isolation of Medicine-Applicable Actinium-225 from Thorium Targets Irradiated by Medium-Energy Protons”. In: *Solvent Extraction and Ion Exchange* 32.5 (Mar. 2014), pp. 468–477. DOI: 10.1080/07366299.2014.896582. URL: https://doi.org/10.1080/07366299.2014.896582.

[25] Tara Mastren et al. “Simultaneous Separation of Actinium and Radium Isotopes from a Proton Irradiated Thorium Matrix”. In: *Scientific Reports* 7.1 (Aug. 2017). DOI: 10.1038/s41598-017-08506-9. URL: https://doi.org/10.1038/s41598-017-08506-9.

[26] B. Zielinska et al. “An Improved Method for the Production of Ac□225/Bi□213 from Th□229 for Targeted Alpha Therapy”. In: *Solvent Extraction and Ion Exchange* 25.3 (Apr. 2007), pp. 339–349. DOI: 10.1080/07366290701285108. URL: https://doi.org/10.1080/07366290701285108.

[27] M. A. Brown. “Metal Oxide Sorbents for the Separation of Radium and Actinium”. In: *Industrial Engineering Chemistry Research* 59.46 (Nov. 2020), pp. 20472–20477. DOI: 10.1021/acs.iecr.0c04084. URL: https://doi.org/10.1021/acs.iecr.0c04084.

[28] Michael R. McDevitt et al. “An 225Ac/213Bi generator system for therapeutic clinical applications: construction and operation”. In: *Applied Radiation and Isotopes* 50.5 (May 1999), pp. 895–904. DOI: 10.1016/s0969-8043(98)00151-1. URL: https://doi.org/10.1016/s0969-8043(98)00151-1.

[29] Andrew K. H. Robertson et al. “232Th-Spallation-Produced 225Ac with Reduced 227Ac Content”. In: *Inorganic Chemistry* 59.17 (July 2020), pp. 12156–12165. DOI: 10.1021/acs.inorgchem.0c01081. URL: https://doi.org/10.1021/acs.inorgchem.0c01081.

[30] L. Szirtes et al. “Swift heavy ion and gamma-ray irradiation of various double metal phosphates”. In: *Radiation Physics and Chemistry* 73.1 (Sept. 2004), pp. 39–44. DOI: 10.1016/j.radphyschem.2004.06.009. URL: https://doi.org/10.1016/j.radphyschem.2004.06.009.

[31] Jochen Winkler and Stefan Marmé. “Titania as a sorbent in normal-phase liquid chromatography”. In: *Journal of Chromatography A* 888.1-2 (Aug. 2000), pp. 51–62. DOI: 10.1016/s0021-9673(00)00489-1. URL: https://doi.org/10.1016/s0021-9673(00)00489-1.

[32] Abraham Clearfield. “INORGANIC ION EXCHANGERS, PAST, PRESENT, AND FUTURE”. In: *Solvent Extraction and Ion Exchange* 18.4 (July 2000), pp. 655–678. DOI: 10.1080/07366290008934702. URL: https://doi.org/10.1080/07366290008934702.

[33] Lukáš Ondrák et al. “α-Zirconium(IV) Phosphate: Static Study of 225Ac Sorption in an Acidic Environment and Its Kinetic Sorption Study Using natEu as a Model System for 225Ac”. In: *Materials* 16.17 (Aug. 2023), p. 5732. DOI: 10.3390/ma16175732. URL: https://doi.org/10.3390/ma16175732.

[34] Nikki A. Thiele and Justin J. Wilson. “Actinium-225 for Targeted α Therapy: Coordination Chemistry and Current Chelation Approaches”. In: *Cancer Biotherapy and Radiopharmaceuticals* 33.8 (June 2018), pp. 336–348. DOI: 10.1089/cbr.2018.2494. URL: https://doi.org/10.1089/cbr.2018.2494.

[35] Bipini Bihari Sahu and Kulamani Parida. “Cation Exchange and Sorption Properties of Crystalline α-Titanium(IV) Phosphate”. In: *Journal of Colloid and Interface Science* 248.2 (Apr. 2002), pp. 221–230. DOI: 10.1006/jcis.2001.7818. URL: https://doi.org/10.1006/jcis.2001.7818.

[36] Wallace W. Schulz, John W. Koenst, and David R. Tallant. *Application of Inorganic Sorbents in Actinide Separations Processes*. Apr. 1980, pp. 17–32. DOI: 10.1021/bk-1980-0117.ch003. URL: https://doi.org/10.1021/bk-1980-0117.ch003.

[37] S.K Shakshooki et al. “Mixed insoluble acid salts of tetravalent metals”. In: *Reactive Polymers Ion Exchangers Sorbents* 7.2-3 (Jan. 1988), pp. 221–226. DOI: 10.1016/0167-6989(88)90143-2. URL: https://doi.org/10.1016/0167-6989(88)90143-2.

[38] E. Spruit. *Title*. Go/No go work. Unpublished work. 2025.

[39] Chunlei Zhang et al. “Adsorption of rare earth La3+ by α- zirconium phosphate: An experimental and density functional theory study”. In: *Journal of Molecular Liquids* 368 (Oct. 2022), p. 120668. DOI: 10.1016/j.molliq.2022.120668. URL: https://doi.org/10.1016/j.molliq.2022.120668.

[40] Ricardo Llavona et al. “Lamellar inorganic ion exchangers. Alkali metal ion exchange on. alpha.- and. gamma.-titanium phosphate”. In: *Inorganic Chemistry* 28.14 (1989), pp. 2863–2868.

[41] G. Alberti et al. “Crystalline insoluble salts of polybasic metals—I Ion-exchange properties of crystalline titanium phosphate”. In: *Journal of Inorganic and Nuclear Chemistry* 29.2 (Feb. 1967), pp. 571–578. DOI: 10.1016/0022-1902(67)80063-0. URL: https://doi.org/10.1016/0022-1902(67)80063-0.

[42] Marina V. Maslova et al. “Synthesis, Characterization, and Sorption Properties of Amorphous Titanium Phosphate and Silica-Modified Titanium Phosphates”. In: *Inorganic Chemistry* 47.23 (Oct. 2008), pp. 11351–11360. DOI: 10.1021/ic801274z. URL: https://doi.org/10.1021/ic801274z.

[43] R. Llavona et al. “Synthesis of γ-titanium phosphate. study of the solids obtained by using water or acetone as washing agents”. In: *Thermochimica Acta* 86 (Apr. 1985), pp. 281–289. DOI: 10.1016/0040-6031(85)87056-8. URL: https://doi.org/10.1016/0040-6031(85)87056-8.

[44] Zakariae Amghouz, Rafael Mendoza-Meroño, and Alaa Adawy. “Nucleation amp; growth of α-Ti(HPO4)2·H2O single-crystal and its structure determination from X-ray single–crystal data”. In: *Journal of Solid State Chemistry* 327 (Aug. 2023), p. 124251. DOI: 10.1016/j.jssc.2023.124251. URL: https://doi.org/10.1016/j.jssc.2023.124251.

[45] A. Nørlund Christensen et al. “X-Ray Powder Diffraction Study of Layer Compounds. The Crystal Structure of alpha-Ti(HPO4)2.H2O and a Proposed Structure for gamma-Ti(H2PO4)(PO4)).2H2O .” In: *Acta chemica Scandinavica* 44 (Jan. 1990), pp. 865–872. DOI: 10.3891/acta.chem.scand.44-0865. URL: https://doi.org/10.3891/acta.chem.scand.44-0865.

[46] Kurt A Kraus and Harold O Phillips. “Adsorption on inorganic materials. I. Cation exchange properties of zirconium phosphate1”. In: *Journal of the American Chemical Society* 78.3 (1956), pp. 694–694.

[47] H.B. Ortíz-Oliveros et al. “Synthesis of α-Ti(HPO 4) 2 ·H 2 O and sorption of Eu (III)”. In: *Chemical Engineering Journal* 236 (Oct. 2013), pp. 398–405. DOI: 10.1016/j.cej.2013.09.103. URL: https://doi.org/10.1016/j.cej.2013.09.103.

[48] Gregory Choppin et al. *Radiochemistry and Nuclear Chemistry*. 4th. Oxford: Academic Press, 2013.

[49] C. E. Harland. *Ion Exchange: Theory and Practice*. 2nd. Cambridge: Royal Society of Chemistry, 1994.

[50] Karl Heinrich Lieser. *Nuclear and Radiochemistry: Fundamentals and Applications*. 1st. Weinheim: VCH, 1991.

[51] G. D. Robinson. *Radiochemical Processing of Activated Targets*. June 2019, pp. 121–138. DOI: 10.1201/9780429278884-4. URL: https://doi.org/10.1201/9780429278884-4.

[52] Andrew H. Bond, Robin D. Rogers, and Mark L. Dietz. “Nuclear Separations for Radiopharmacy: The Need for Improved Separations To Meet Future Research and Clinical Demands”. In: *Industrial Engineering Chemistry Research* 39.9 (July 2000), pp. 3130–3134. DOI: 10.1021/ie990765j. URL: https://doi.org/10.1021/ie990765j.

[53] International Atomic Energy Agency. *Cyclotron Produced Radionuclides: Principles and Practice*. Technical Reports Series No. 465. Vienna: IAEA, 2009.

[54] Michael R. McDevitt et al. “Design and Development of 225Ac Radioimmunoconjugates”. In: *Journal of Nuclear Medicine* 59.Supplement 1 (2018), p. 12. DOI: 10.2967/jnumed.117.203075.

[55] Gerhart Friedlander et al. *Nuclear and Radiochemistry*. 3rd. New York: Wiley, 1981.

[56] A. N. Vasiliev et al. “Radiation Stability of Sorbents in Medical 225Ac/213Bi Generators”. In: *Solvent Extraction and Ion Exchange* 39.4 (Nov. 2020), pp. 353–372. DOI: 10.1080/07366299.2020.1846892. URL: https://doi.org/10.1080/07366299.2020.1846892.

[57] E. P. Horwitz et al. “Novel Extraction of Chromatographic Resins Based on Tetraalkyldiglycolamides: Characterization and Potential Applications”. In: *Solvent Extraction and Ion Exchange* 23.3 (May 2005), pp. 319–344. DOI: 10.1081/sei-200049898. URL: https://doi.org/10.1081/sei-200049898.

[58] S. Vuchkan et al. “Comprehensive studies of organic and inorganic adsorbents”. In: *RAP Conference Proceedings* (Jan. 2021). DOI: 10.37392/rapproc.2021.05. URL: https://doi.org/10.37392/rapproc.2021.05.

[59] M. Brown, Anna Servis, and Peter Tkac. *Development and Optimization of a Purification Process to Recover 99Mo from Low-enriched Uranium*. Tech. rep. Dec. 2020. DOI: 10.2172/1767121. URL: https://doi.org/10.2172/1767121.

[60] Thomas J. Ruth. “The Uses of Radiotracers in the Life Sciences”. In: *Reports on Progress in Physics* 72.1 (2009), p. 016701. DOI: 10.1088/0034-4885/72/1/016701.

[61] Jan Rydberg et al. *Solvent Extraction Principles and Practice*. 2nd. New York: Marcel Dekker, 2004.

[62] Mark L. Dietz. “Ion Chromatography in Environmental Analysis”. In: *Encyclopedia of Analytical Chemistry* (2006). DOI: 10.1002/9780470027318.a0808.

[63] Rushikesh B. “A Brief Review on Different Chromatographic Techniques”. In: *Open Access Journal of Pharmaceutical Research* 8.1 (Jan. 2024). DOI: 10.23880/oajpr-16000294. URL: https://doi.org/10.23880/oajpr-16000294.

[64] Abraham Clearfield. “Inorganic Ion Exchangers: A Technology Ripe for Development”. In: *Industrial & Engineering Chemistry Research* 34.10 (1995), pp. 2865–2872. DOI: 10.1021/ie00037a001.

[65] Valery Radchenko, Ayagoz Baimukhanova, and Dmitry Filosofov. “Radiochemical aspects in modern radiopharmaceutical trends: a practical guide”. In: *Solvent Extraction and Ion Exchange* 39.7 (Feb. 2021), pp. 714–744. DOI: 10.1080/07366299.2021.1874099. URL: https://doi.org/10.1080/07366299.2021.1874099.

[66] Friedrich Helfferich. *Ion Exchange*. New York: McGraw-Hill, 1962.

[67] Yizhak Marcus. *Ion Solvation*. Chichester: Wiley, 1997.

[68] Mitsuo Abe. *Ion-Exchange Selectivities of Inorganic Ion Exchangers*. June 2021, pp. 381–440. DOI: 10.1201/9781003208846-9. URL: https://doi.org/10.1201/9781003208846-9.

[69] Xiangsen Shao et al. “Selective recovery of La3+ from rare earth mine tailwater by titanium phosphate adsorbents with different crystal forms”. In: *Journal of Water Process Engineering* 61 (Apr. 2024), p. 105354. DOI: 10.1016/j.jwpe.2024.105354. URL: https://doi.org/10.1016/j.jwpe.2024.105354.

[70] R. D. Shannon. “Revised effective ionic radii and systematic studies of interatomic distances in halides and chalcogenides”. In: *Acta Crystallographica Section A* 32.5 (Sept. 1976), pp. 751–767. DOI: 10.1107/s0567739476001551. URL: https://doi.org/10.1107/s0567739476001551.

[71] Steven A. Grant and Philip Fletcher. *Chemical Thermodynamics of Cation Exchange Reactions: Theoretical and Practical Considerations*. Oct. 2017, pp. 1–108. DOI: 10.1201/9780203749753-1. URL: https://doi.org/10.1201/9780203749753-1.

[72] C. Airoldi and L. M. Nunes. “Calorimetric Determinations of Ba2+ and La3+ in the Ion-Exchange Process Involving Pure and Modified α-Titanium Phosphates”. In: *Langmuir* 16.3 (Nov. 1999), pp. 1436–1439. DOI: 10.1021/la9902892. URL: https://doi.org/10.1021/la9902892.

[73] Yizhak Marcus. “Ionic radii in aqueous solutions”. In: *Chemical Reviews* 88.8 (Dec. 1988), pp. 1475–1498. DOI: 10.1021/cr00090a003. URL: https://doi.org/10.1021/cr00090a003.

[74] Si-Yao Guo et al. “Synthesis of shape-controlled mesoporous titanium phosphate nanocrystals: The hexagonal titanium phosphate with enhanced hydrogen generation from water splitting”. In: *International Journal of Hydrogen Energy* 39.6 (Dec. 2013), pp. 2446–2453. DOI: 10.1016/j.ijhydene.2013.12.007. URL: https://doi.org/10.1016/j.ijhydene.2013.12.007.

[75] Kumar Brajesh et al. “Room-temperature structural, magnetic, and dielectric characteristics of La-doped CuO bulk multiferroic”. In: *Journal of the American Ceramic Society* 106.11 (July 2023), pp. 6769–6777. DOI: 10.1111/jace.19306. URL: https://doi.org/10.1111/jace.19306.

[76] Ingmar Persson. “Hydrated metal ions in aqueous solution: How regular are their structures?” In: *Pure and Applied Chemistry* 82.10 (Aug. 2010), pp. 1901–1917. DOI: 10.1351/pac-con-09-10-22. URL: https://doi.org/10.1351/pac-con-09-10-22.

[77] Charles P. Poole et al. *Cuprate crystallographic structures*. Jan. 2007, pp. 195–229. DOI: 10.1016/b978-012088761-3/50030-2. URL: https://doi.org/10.1016/b978-012088761-3/50030-2.

[78] B. Zielińska and A. Bilewicz. “The hydrolysis of actinium”. In: *Journal of Radioanalytical and Nuclear Chemistry* 261.1 (Jan. 2004), pp. 195–198. DOI: 10.1023/b:jrnc.0000030956.61947.c5. URL: https://doi.org/10.1023/b:jrnc.0000030956.61947.c5.

[79] Hengfang Zhang. *Hot-wall MOCVD of N-polar group-III nitride materials*. June 2021. ISBN: 9789179299309. DOI: 10.3384/lic.diva-175502.

[80] Cameron F. Holder and Raymond E. Schaak. “Tutorial on Powder X-ray Diffraction for Characterizing Nanoscale Materials”. In: *ACS Nano* 13.7 (July 2019), pp. 7359–7365. DOI: 10.1021/acsnano.9b05157. URL: https://doi.org/10.1021/acsnano.9b05157.

[81] Sebastian Bruque et al. “Synthesis optimization and crystal structures of layered metal (IV) hydrogen phosphates,. alpha.-M (HPO4) 2. cntdot. H2O (M= Ti, Sn, Pb)”. In: *Inorganic Chemistry* 34.4 (1995), pp. 893–899.

[82] M. Satya Kishore et al. “Electrochemical intercalation of lithium in the titanium hydrogeno phosphate Ti(HPO4)2·H2O”. In: *Journal of Power Sources* 169.2 (Mar. 2007), pp. 355–360. DOI: 10.1016/j.jpowsour.2007.03.051. URL: https://doi.org/10.1016/j.jpowsour.2007.03.051.

[83] Per-Erik Tegehall. “Synthesis of Crystalline Titanium (IV) Phosphates by Direct Precipitation from Ti (III) Solutions and Ion”. In: *Acta Chemica Scandinavica* 40 (1986), pp. 507–514.

[84] Daniela Rusanova-Naydenova et al. “Synthesis and structural characterisation of solid titanium(iv) phosphate materials by means of X-ray absorption and NMR spectroscopy”. In: *Dalton Transactions* 51.21 (Jan. 2022), pp. 8192–8207. DOI: 10.1039/d2dt00902a. URL: https://doi.org/10.1039/d2dt00902a.

[85] Mylène Trublet and Daniela Rusanova. “Complete Column Trials for Water Refinement Using Titanium(IV) Phosphate Sorbents”. In: *ACS Sustainable Chemistry Engineering* 6.5 (Mar. 2018), pp. 6157–6165. DOI: 10.1021/acssuschemeng.7b04823. URL: https://doi.org/10.1021/acssuschemeng.7b04823.

[86] Mylène Trublet, Daniela Rusanova, and Oleg N. Antzutkin. “Revisiting syntheses of Ti(iv)/H2PO4–HPO4 functional ion-exchangers, properties and features”. In: *New Journal of Chemistry* 42.2 (Nov. 2017), pp. 838–845. DOI: 10.1039/c7nj03065g. URL: https://doi.org/10.1039/c7nj03065g.

[87] Colin R. Groom et al. “The Cambridge Structural Database”. In: *Acta Crystallographica Section B Structural Science Crystal Engineering and Materials* 72.2 (Apr. 2016), pp. 171–179. DOI: 10.1107/s2052520616003954. URL: https://doi.org/10.1107/s2052520616003954.

[88] T. Degen et al. “The HighScore suite”. In: *Powder Diffraction* 29.Supplement S2 (Dec. 2014), S13–S18.

[89] S. Kabekkodu, A. Dosen, and T. Blanton. “PDF-5+: a comprehensive Powder Diffraction File™ for materials characterization”. In: *Powder Diffraction* 39.2 (2024), pp. 47–59. DOI: 10.1017/S0885715624000150.

[90] *Neutron irradiation facilities*. URL: https://www.tudelft.nl/tnw/zakelijk/faciliteiten/tu-delft-reactor-institute/diensten-consultancy/neutron-irradiation-facilities.

[91] S.O. Swartjes. *Investigating Optimal pH Conditions for Separation of Barium and Lanthanum with Inorganic Resins*. Bachelor thesis. Unpublished work. 2024.

[92] VI Khitrova, MF Bundule, and ZG Pinsker. “Electron-diffraction study of titanium-dioxide in thin-films”. In: *Kristallografiya* 22.6 (1977), pp. 1253–1258.

[93] Aránzazu Espina et al. “Calorimetric study of amine adsorption on α-and γ-titanium phosphate”. In: *The Journal of Physical Chemistry B* 102.10 (1998), pp. 1713–1716.

[94] Wen-Jing Peng et al. “Embedding Alkyldiamine into Layered α-Titanium Phosphate via Direct-Ion Exchange and its Application in EuIII Removal from Water”. In: *Zeitschrift für anorganische und allgemeine Chemie* 646.8 (Apr. 2020), pp. 399–406. DOI: 10.1002/zaac.201900349. URL: https://doi.org/10.1002/zaac.201900349.

[95] Chao Wang et al. “Bending Nanowire Growth in Solution by Mechanical Disturbance”. In: *Nano Letters* 10.6 (May 2010), pp. 2121–2125. DOI: 10.1021/nl100661v. URL: https://doi.org/10.1021/nl100661v.

[96] Deena Titus, E James Jebaseelan Samuel, and Selvaraj Mohana Roopan. “Nanoparticle characterization techniques”. In: *Green synthesis, characterization and applications of nanoparticles*. Elsevier, 2019, pp. 303–319.

[97] Dale E Newbury and Nicholas WM Ritchie. “Performing elemental microanalysis with high accuracy and high precision by scanning electron microscopy/silicon drift detector energy-dispersive X-ray spectrometry (SEM/SDD-EDS)”. In: *Journal of materials science* 50 (2015), pp. 493–518.

[98] Ron Jenkins. “X-Ray Techniques: Overview”. In: *Encyclopedia of Analytical Chemistry* (Oct. 2000). DOI: 10.1002/9780470027318.a6801. URL: https://doi.org/10.1002/9780470027318.a6801.

[99] W. Pitschke, H. Hermann, and N. Mattern. “The influence of surface roughness on diffracted X-ray intensities in Bragg–Brentano geometry and its effect on the structure determination by means of Rietveld analysis”. In: *Powder Diffraction* 8.2 (June 1993), pp. 74–83. DOI: 10.1017/s0885715600017875. URL: https://doi.org/10.1017/s0885715600017875.

[100] Lars Bannenberg. *Diffraction - II: Advanced Materials Analysis by Radiation Instrumentation*. Course slides CH3765 at TU Delft, Unpublished lecture material. 2025.

[101] A. J. Bourdillon, P. G. Self, and W. M. Stobbs. “Crystallographic orientation effects in energy dispersive X-ray analysis”. In: *Philosophical Magazine A* 44.6 (Dec. 1981), pp. 1335–1350. DOI: 10.1080/01418618108235813. URL: https://doi.org/10.1080/01418618108235813.

[102] K. Kadirvelu and Jyotsna Goel. “Ion Exchange and Inorganic Adsorption”. In: *Water Encyclopedia* (Oct. 2004), pp. 490–496. DOI: 10.1002/047147844x.pc1506. URL: https://doi.org/10.1002/047147844x.pc1506.

[103] Teresia Möller et al. “Separation of lanthanum, hafnium, barium and radiotracers yttrium-88 and barium-133 using crystalline zirconium phosphate and phosphonate compounds as prospective materials for a Ra-223 radioisotope generator”. In: *Applied Radiation and Isotopes* 69.7 (Feb. 2011), pp. 947–954. DOI: 10.1016/j.apradiso.2011.02.033. URL: https://doi.org/10.1016/j.apradiso.2011.02.033.

[104] Falco Reissig, Klaus Kopka, and Constantin Mamat. “The impact of barium isotopes in radiopharmacy and nuclear medicine – From past to presence”. In: *Nuclear Medicine and Biology* 98-99 (May 2021), pp. 59–68. DOI: 10.1016/j.nucmedbio.2021.05.003. URL: https://doi.org/10.1016/j.nucmedbio.2021.05.003.

[105] Timothy A. Sipkens et al. “Tutorial: Guide to error propagation for particle counting measurements”. In: *Journal of Aerosol Science* 167 (Oct. 2022), p. 106091. DOI: 10.1016/j.jaerosci.2022.106091. URL: https://doi.org/10.1016/j.jaerosci.2022.106091.

[106] Sue A Kang et al. “Phosphate uptake by TiO2: Batch studies and NMR spectroscopic evidence for multisite adsorption”. In: *Journal of Colloid and Interface Science* 364.2 (Aug. 2011), pp. 455–461. DOI: 10.1016/j.jcis.2011.07.088. URL: https://doi.org/10.1016/j.jcis.2011.07.088.

[107] Yu. Ya. Yakubovich and V. G. Alekseev. “Hydrolysis constants of tervalent lanthanum and lanthanide ions in 0.1 M KNO3 solution”. In: *Russian Journal of Inorganic Chemistry* 57.6 (June 2012), pp. 911–915. DOI: 10.1134/s0036023612060265. URL: https://doi.org/10.1134/s0036023612060265.

[108] Abraham Clearfield. “Zirconium phosphate”. In: *Inorganic Ion Exchange Materials* (1982), pp. 1–74.

[109] Rajesh Chakraborty, Koustava Bhattacharaya, and Pabitra Chattopadhyay. “Nanostructured zirconium phosphate as ion exchanger: Synthesis, size dependent property and analytical application in radiochemical separation”. In: *Applied Radiation and Isotopes* 85 (Nov. 2013), pp. 34–38. DOI: 10.1016/j.apradiso.2013.10.018. URL: https://doi.org/10.1016/j.apradiso.2013.10.018.

[110] G. Alberti and E. Torracca. “Crystalline insoluble salts of polybasic metals - II. Synthesis of crystalline zirconium or titanium phosphate by direct precipitation”. In: *Journal of Inorganic and Nuclear Chemistry* 30.1 (Jan. 1968), pp. 317–318. DOI: 10.1016/0022-1902(68)80096-x. URL: https://doi.org/10.1016/0022-1902(68)80096-x.

[111] Clemens Kratochwil et al. “Dosing 225Ac-DOTATOC in patients with somatostatin-receptor-positive solid tumors: 5-year follow-up of hematological and renal toxicity”. In: *European Journal of Nuclear Medicine and Molecular Imaging* 49.1 (Aug. 2021), pp. 54–63. DOI: 10.1007/s00259-021-05474-1. URL: https://pmc.ncbi.nlm.nih.gov/articles/PMC8712294.

[112] Madhav Prasad Yadav et al. “Efficacy and safety of 225Ac-PSMA-617 targeted alpha therapy in metastatic castration-resistant Prostate Cancer patients”. In: *Theranostics* 10.20 (Jan. 2020), pp. 9364–9377. DOI: 10.7150/thno.48107. URL: https://www.thno.org/v10p9364.

[113] Andrew K. H. Robertson et al. “Development of 225Ac Radiopharmaceuticals: TRIUMF Perspectives and Experiences”. In: *Current Radiopharmaceuticals* 11.3 (2018), pp. 156–172. DOI: 10.2174/1874471011666180418125818.

[114] C. J. Helmers et al. “Ion exchange kinetics and equilibrium”. In: *Chemical Engineering Progress* 54.6 (1958), pp. 65–72.

[115] Irving Langmuir. “The constitution and fundamental properties of solids and liquids.” In: *Journal of the American Chemical Society* 38.11 (Nov. 1916), pp. 2221–2295. DOI: 10.1021/ja02268a002. URL: https://doi.org/10.1021/ja02268a002.

[116] H. Freundlich. “Über die Adsorption in Lösungen”. In: *Zeitschrift für Physikalische Chemie* 57.1 (1906), pp. 385–470. DOI: 10.1515/zpch-1907-5723.

[117] S. Brunauer, P. H. Emmett, and E. Teller. “Adsorption of gases in multimolecular layers”. In: *Journal of the American Chemical Society* 60.2 (1938), pp. 309–319. DOI: 10.1021/ja01269a023.

A
Supportive results synthesis

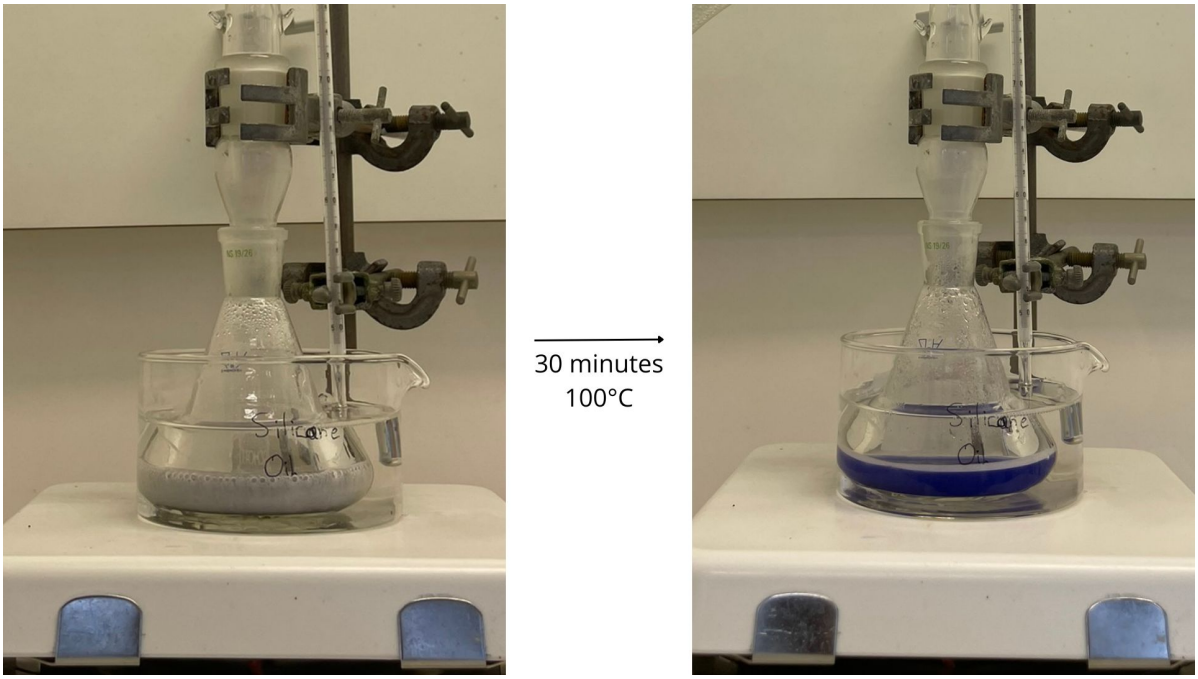

Figure A.1: Color change observed during the dissolution of Ti powder in H_3PO_4. The solution turns purple due to the formation of Ti^{3+} ions, as part of the synthesis of method II.

Table A.1: Quantitative elemental composition of TiP_2O_9.

	TiP_2O_9	
Element	**Mass (%)**	**Atom (%)**
O	57	75
P	24	17
Ti	19	8

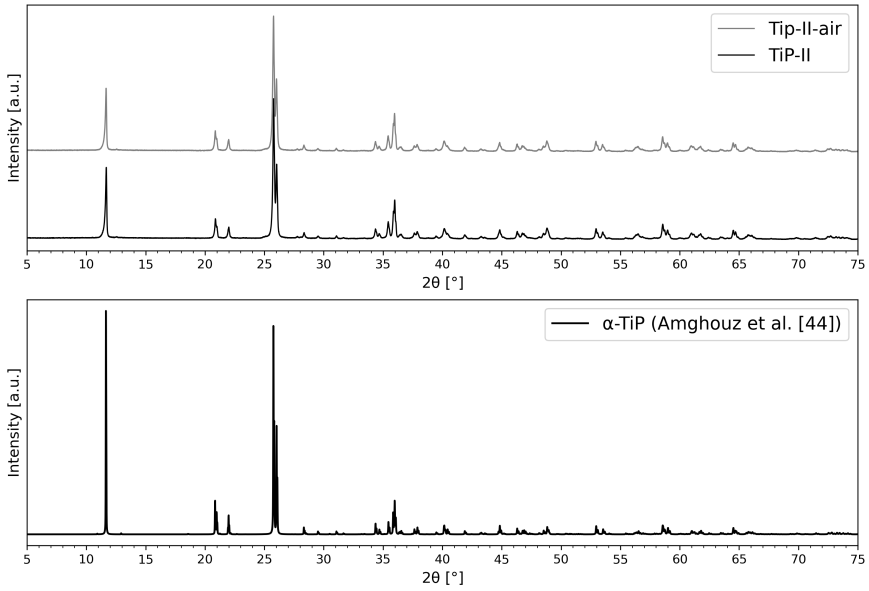

Figure A.2: Powder XRD pattern of TiP-II material, dried in an oven and to air (top), compared to those synthesised by Amghouz et al. [44] (bottom) for comparison.

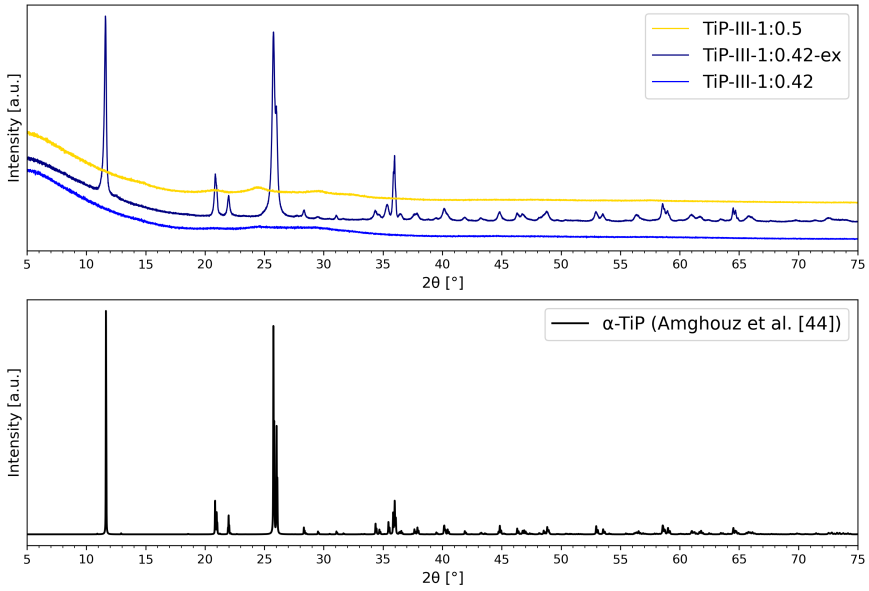

Figure A.3: Powder XRD pattern of TiP-III-1:0.42 and TiP-III-1:0.5 materials using a fixed slit (top) compared to those synthesised by Amghouz et al. [44] (bottom) for comparison.

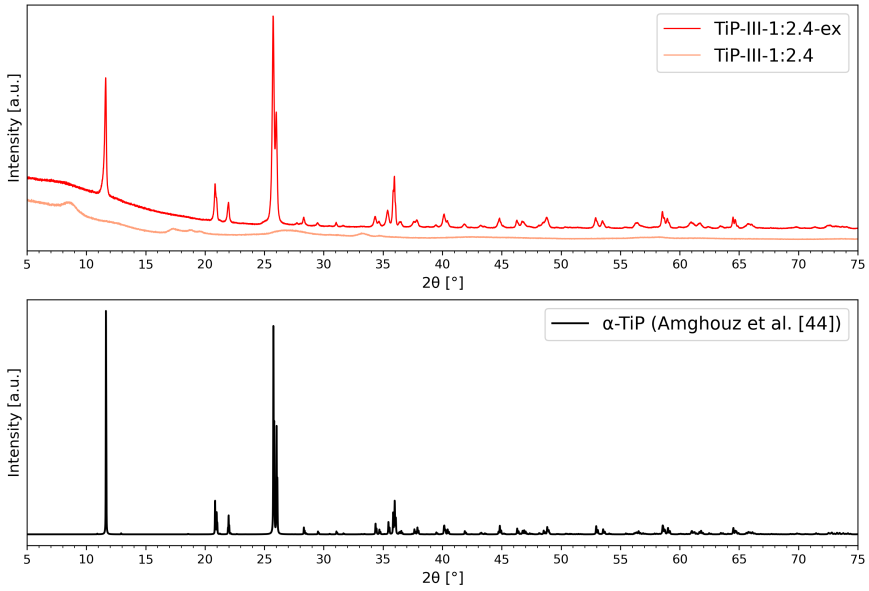

Figure A.4: Powder XRD pattern of TiP-III-1:2.4 materials using a fixed slit (top) compared to those synthesised by Amghouz et al. [44] (bottom) for comparison.

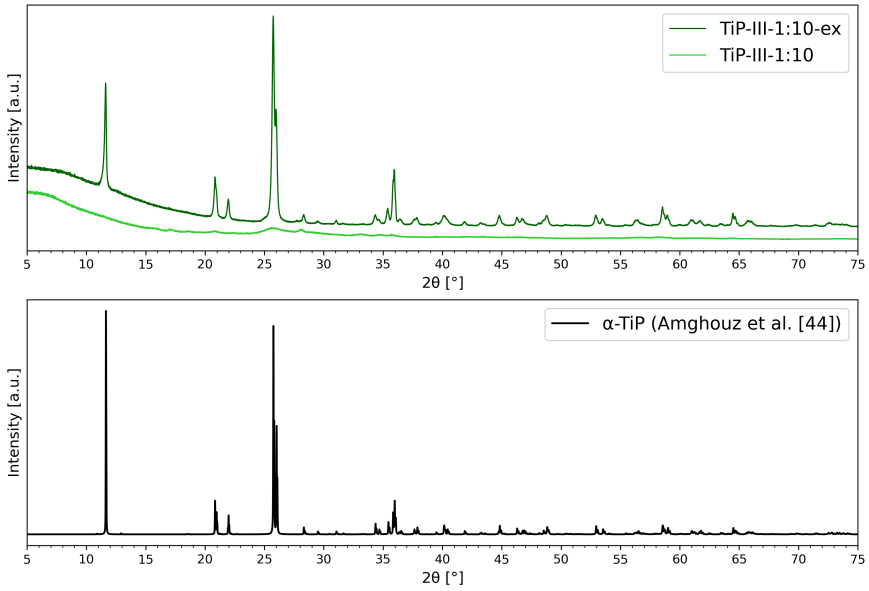

Figure A.5: Powder XRD pattern of TiP-III-1:10 materials using a fixed slit (top) compared to those synthesised by Amghouz et al. [44] (bottom) for comparison.

A.1. Slit experiment

To determine the origin of the X-rays detected at low angles, A slit experiment was designed. A sample of TiP-I was measured using XRD with both variable and fixed slit configurations. The results, presented in Figure A.6, revealed that the use of a variable slit completely eliminates the low-angle X-rays detected with the fixed slit. This confirmed that the low-angle signal was primarily caused by air scattering.

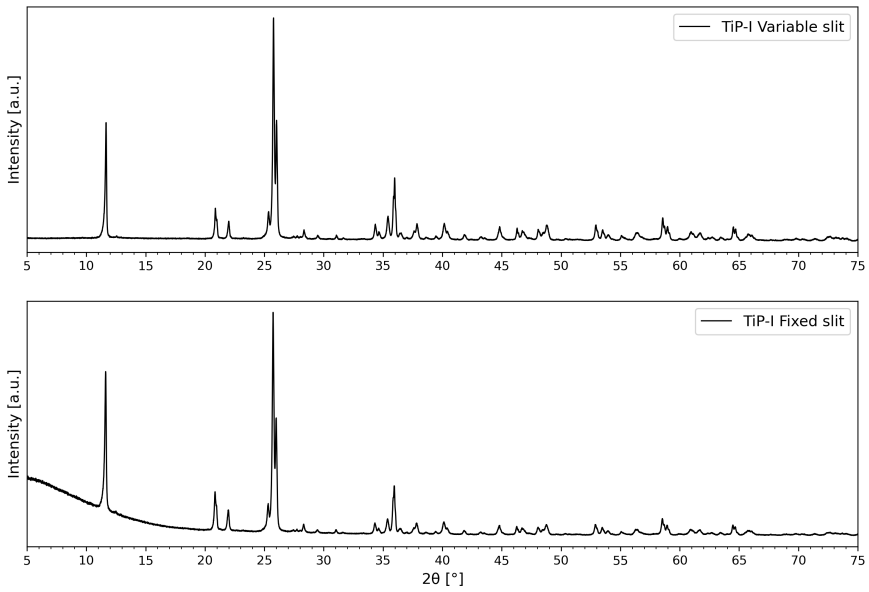

Figure A.6: XRD of TiP-I material using fixed slit (top) and varying slit configuration (bottom).

In X-ray diffraction (XRD) experiments, the choice between a variable slit and a fixed slit configuration has significant implications for the intensity of diffraction peaks across the angular range. A variable slit adjusts its width depending on the angle of incidence. At low angles, the slit is narrow to match the reduced sample surface, minimising air scattering and therefore ensuring higher signal-to-noise ratios. However, at larger angles, the slit opens wider, increasing the sample area exposed to the X-ray beam. This dynamic adjustment leads to relatively higher peak intensities at larger angles compared to those obtained using a fixed slit.

Table A.2: Effect of synthesis conditions on TiP-II crystallite formation.

Description	**Ref. time** (h)	**Temp.** ($^\circ$C)	**Stir. speed** (rpm)	**Specifics**	**Crystallite size** (µm)	**Product**
Original	24	100	200	-	1-5	α-TiP
Repetition	24	100	200	-	1-5	α-TiP
72h	72	100	200	-	1-5	α-TiP
14d	336	100	200	-	1-5	α-TiP
170 $^\circ$C	24	170	200	-	1-5	Mixture of γ-TiP and α-TiP
No stirring	24	100	0	0.02 g Ti powder	-	No precipitate formed

B
SEM analysis and EDS mapping TiP-III

B.1. TiP-III-1:0.42

B.1.0.1. SEM analysis

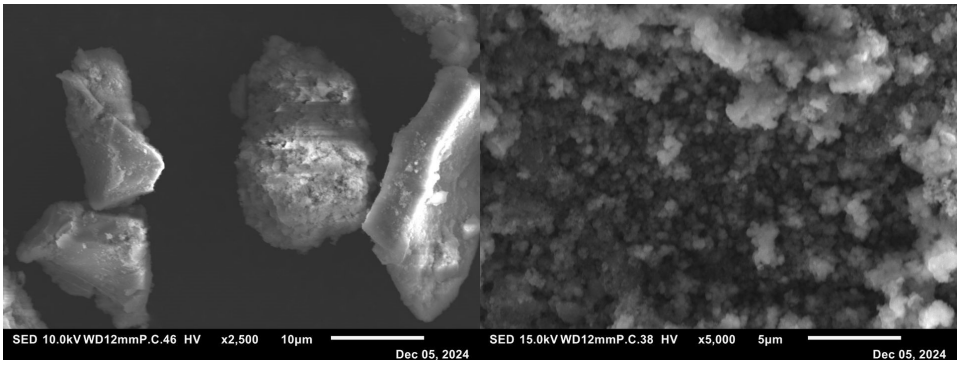

Figure B.1: SEM images of the TiP-III-1:0.42 material, imaged at magnifications of 2,500x (left) and 5,000x (right).

B.1.0.2. EDS mapping

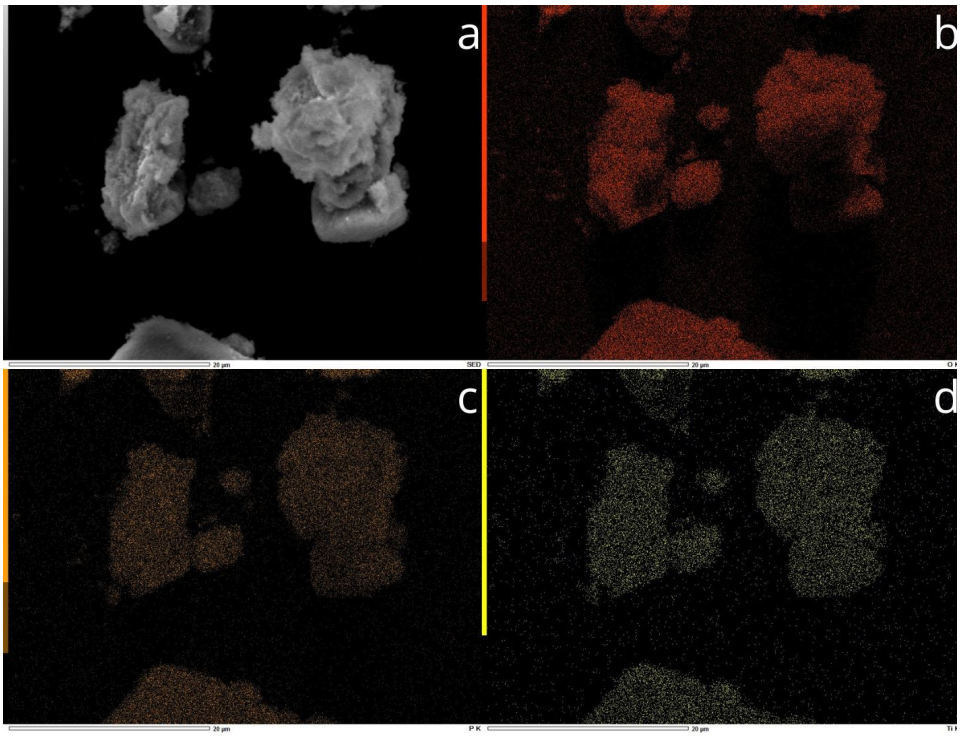

Figure B.2: EDS mapping of the spatial distribution of O (b), P (c) and Ti (d) atoms across the imaged (a) TiP-III-1:0.42 material (2,700x).

B.2. TiP-III-1:0.5

B.2.0.1. SEM analysis

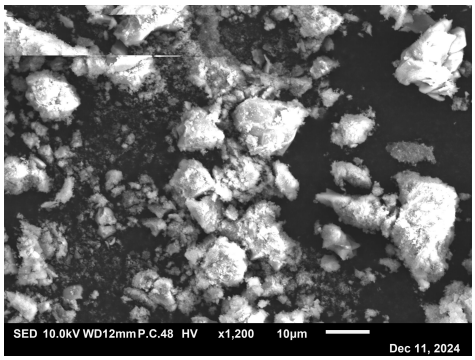

Figure B.3: SEM image of the TiP-III-1:0.5 material, imaged at magnifications of 2,500x.

Table B.1: Quantitative elemental composition of TiP-III-0.5 material.

	TiP-III-1:0.5	
Element	Mass (%)	Atom (%)
O	53	74
P	16	11
S	1.42	0.98
Ti	29	14

B.2.0.2. EDS mapping

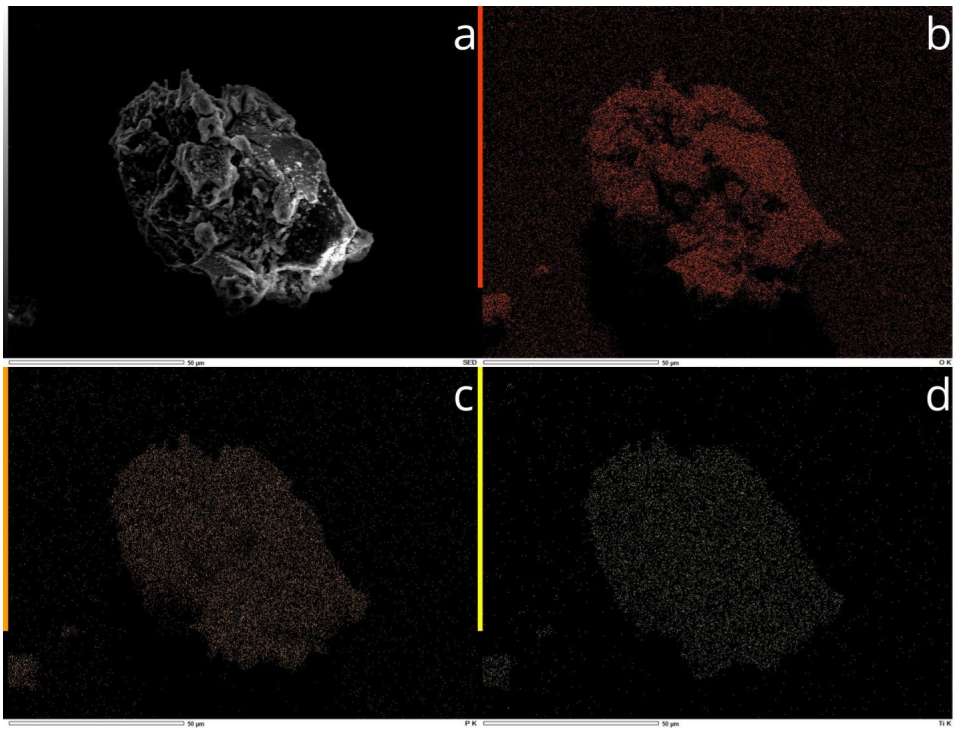

Figure B.4: EDS mapping of the spatial distribution of O (b), P (c) and Ti (d) atoms across the imaged (a) TiP-III-1:0.5 material (3,300x).

B.3. TiP-III-1:2.4

B.3.0.1. SEM analysis

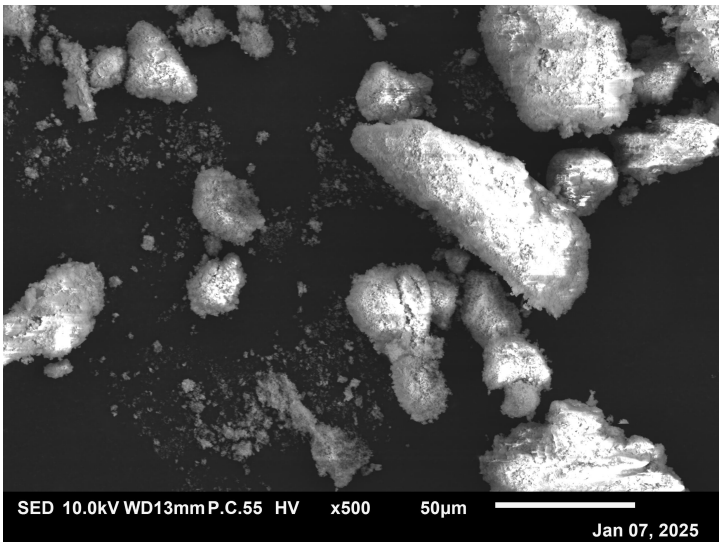

Figure B.5: SEM image of the TiP-III-1:2.4 material, imaged at magnifications of 500x.

B.3.0.2. EDS mapping

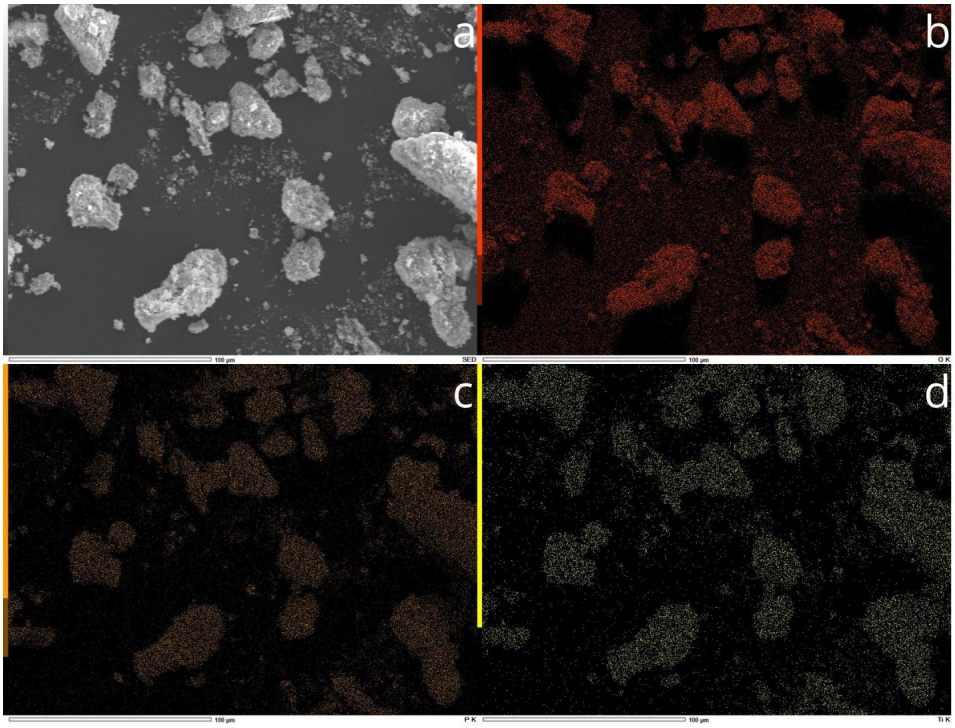

Figure B.6: EDS mapping of the spatial distribution of O (b), P (c) and Ti (d) atoms across the imaged (a) TiP-III-1:2.4 material (3,300x).

B.4. TiP-III-1:10

B.4.0.1. SEM analysis

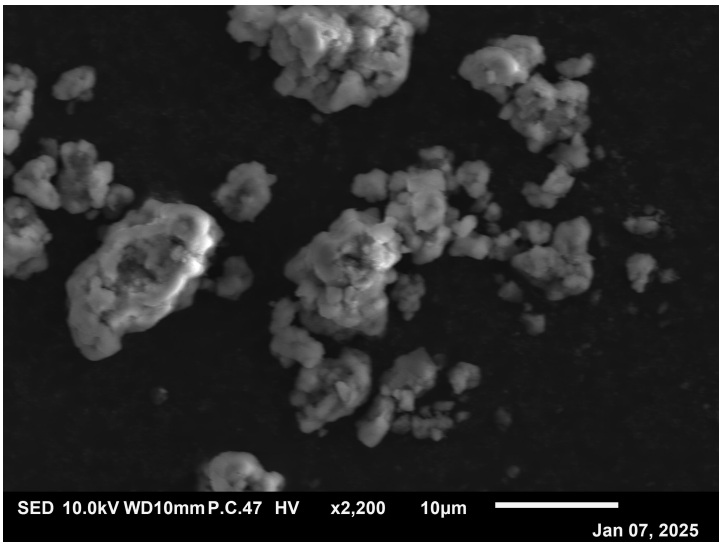

Figure B.7: SEM images of the TiP-III-1:10 material, imaged at magnifications of 2,200x.

B.4.0.2. EDS mapping

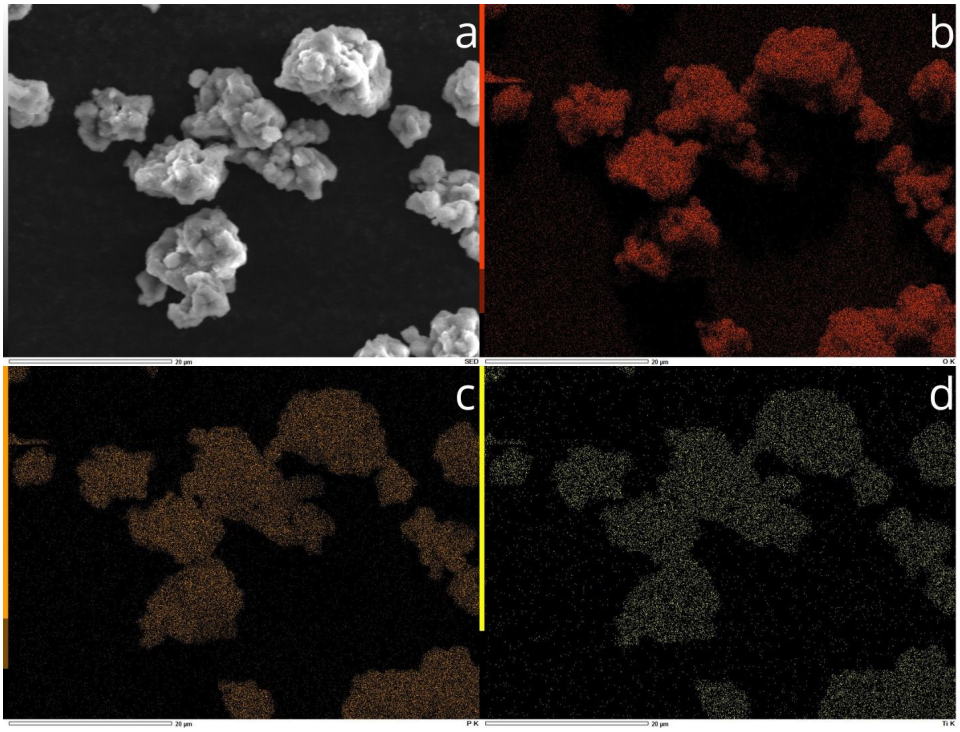

Figure B.8: EDS mapping of the spatial distribution of O (b), P (c) and Ti (d) atoms across the imaged (a) TiP-III-1:10 material (2,200x).

B.5. TiP-III-1:0.42-ex

B.5.0.1. SEM analysis

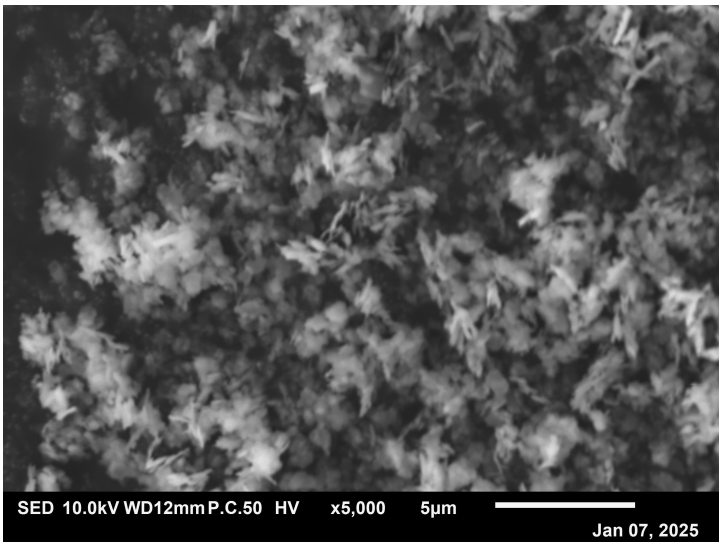

Figure B.9: SEM image of the TiP-III-1:0.42-ex crystallites, imaged at magnifications of 5,000x.

B.5.0.2. EDS mapping

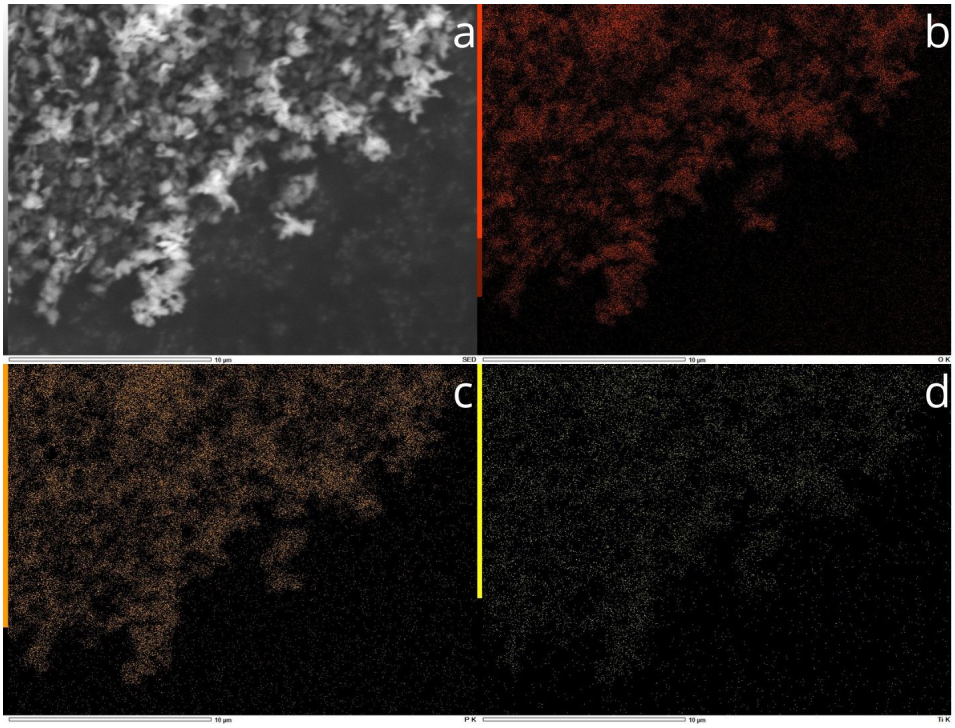

Figure B.10: EDS mapping of the spatial distribution of O (b), P (c) and Ti (d) atoms across the imaged (a) TiP-III-1:0.42-ex crystallites (5,500x).

B.6. TiP-III-1:2.4-ex

B.6.0.1. SEM analysis

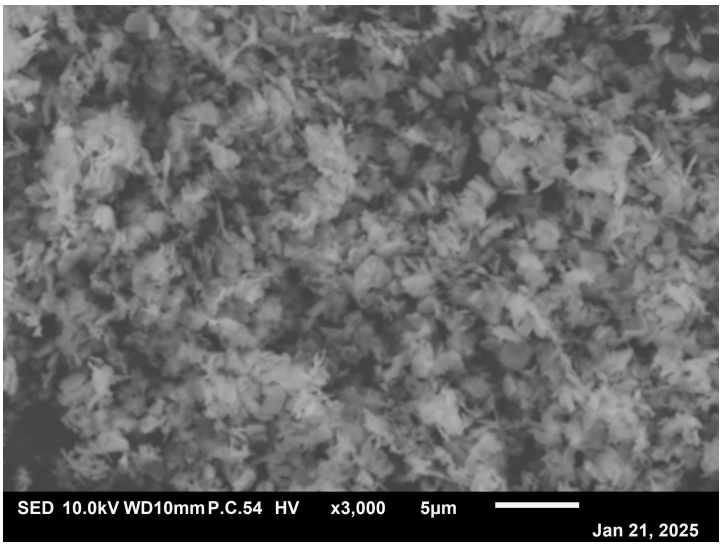

Figure B.11: SEM image of the TiP-III-1:2.4-ex crystallites, imaged at magnifications of 3,000x.

B.6.0.2. EDS mapping

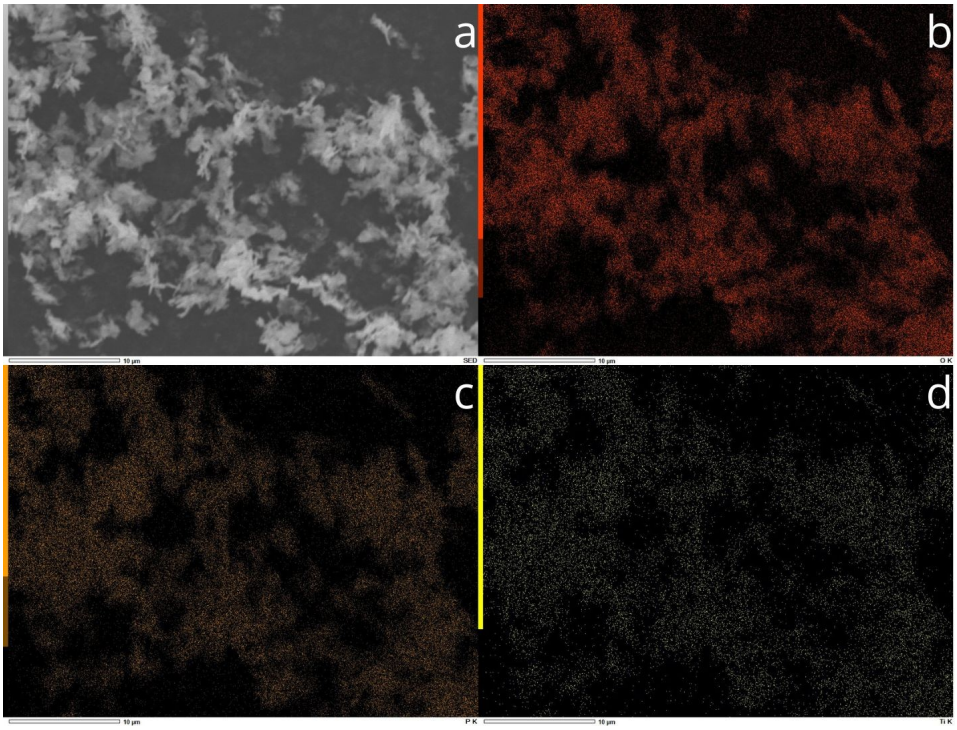

Figure B.12: EDS mapping of the spatial distribution of O (b), P (c) and Ti (d) atoms across the imaged (a) TiP-III-1:2.4-ex crystallites (3,000x).

B.7. TiP-III-1:10-ex

B.7.0.1. SEM analysis

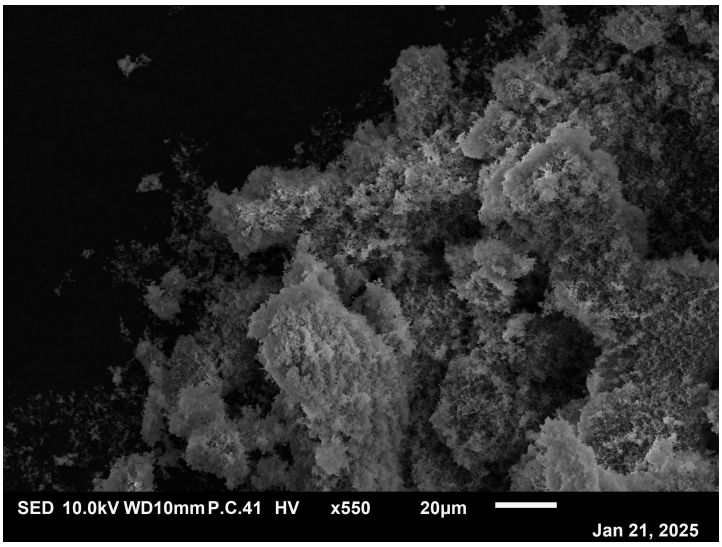

Figure B.13: SEM image of the TiP-III-1:10-ex crystallites, imaged at magnifications of 550x.

B.7.0.2. EDS mapping

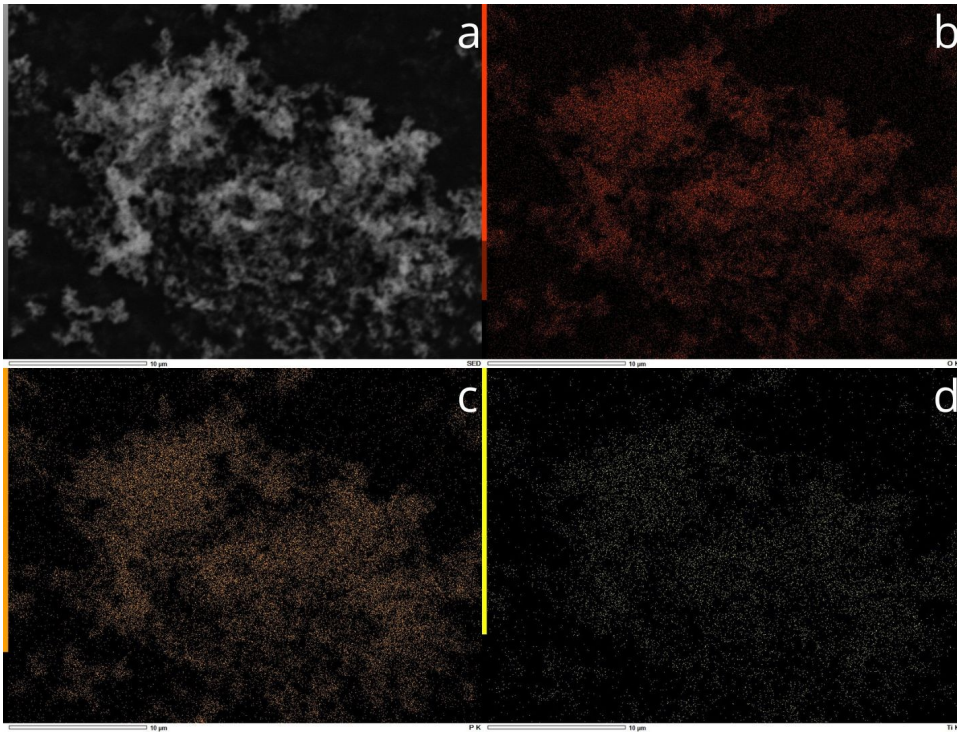

Figure B.14: EDS mapping of the spatial distribution of O (b), P (c) and Ti (d) atoms across the imaged (a) TiP-III-1:2.4-ex crystallites (3,700x).

B.8. Results initial EDS analysis TiP-III-1:0.42

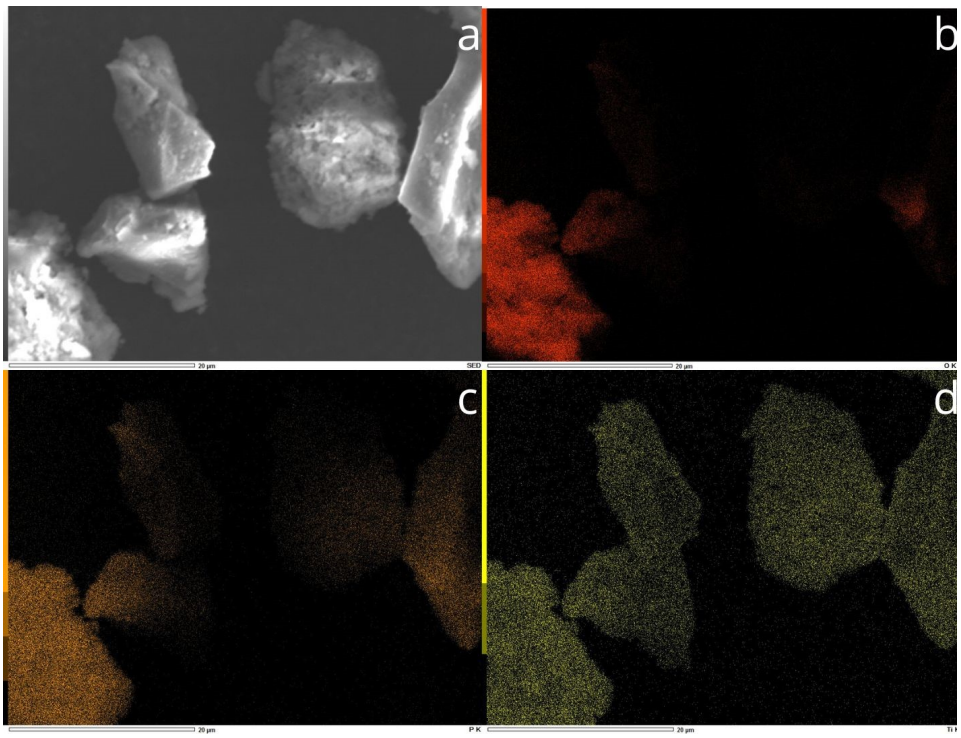

Figure B.15: EDS mapping of the spatial distribution of O (b), P (c) and Ti (d) atoms across the TiP-III-1:0.42 material (2,500x) (initial measurement).

Table B.2: Quantitative elemental composition of TiP-III-0.42 material (initial measurement).

	TiP-III-1:0.42-ex	
Element	Mass (%)	Atom (%)
O	39	63
P	16	13
S	0.24	0.19
Ti	45	24

C
Supportive results adsorption experiments

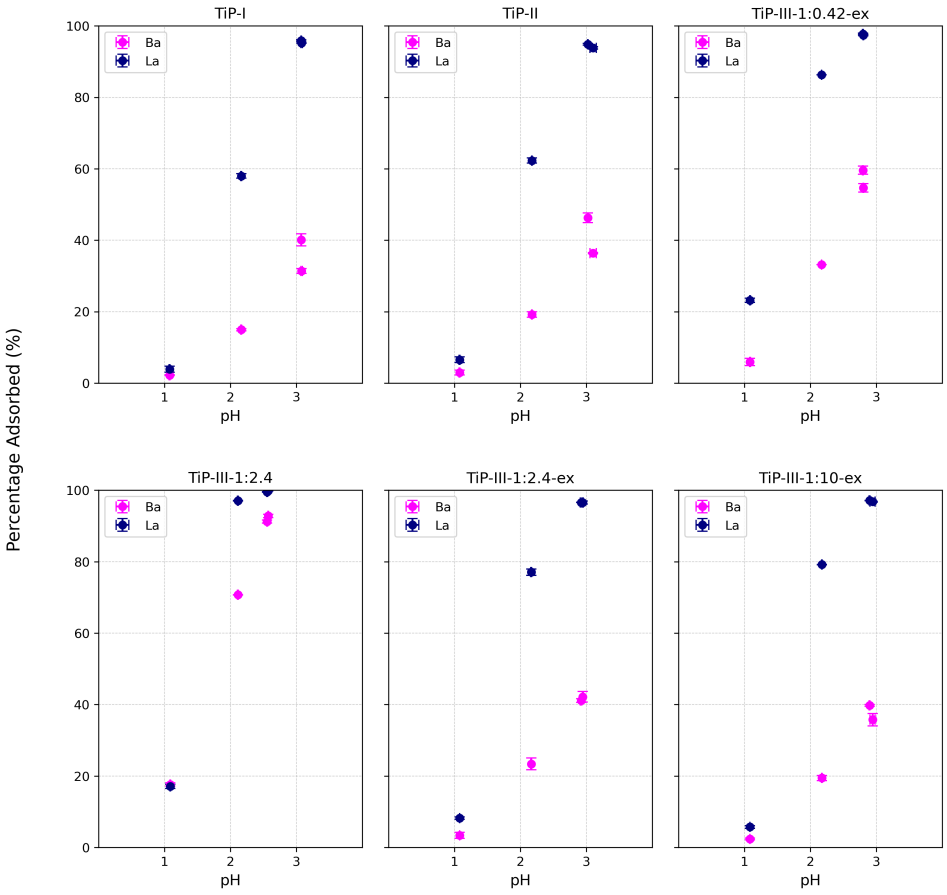

Figure C.1: Adsorption (%) of Ba^{2+} (C_0 = 1.5 mM) and La^{3+} (C_0 = 2.5 µM) for TiP materials at varying equilibrium pH values (batch tests, 0.05 g sorbent, 20 °C).

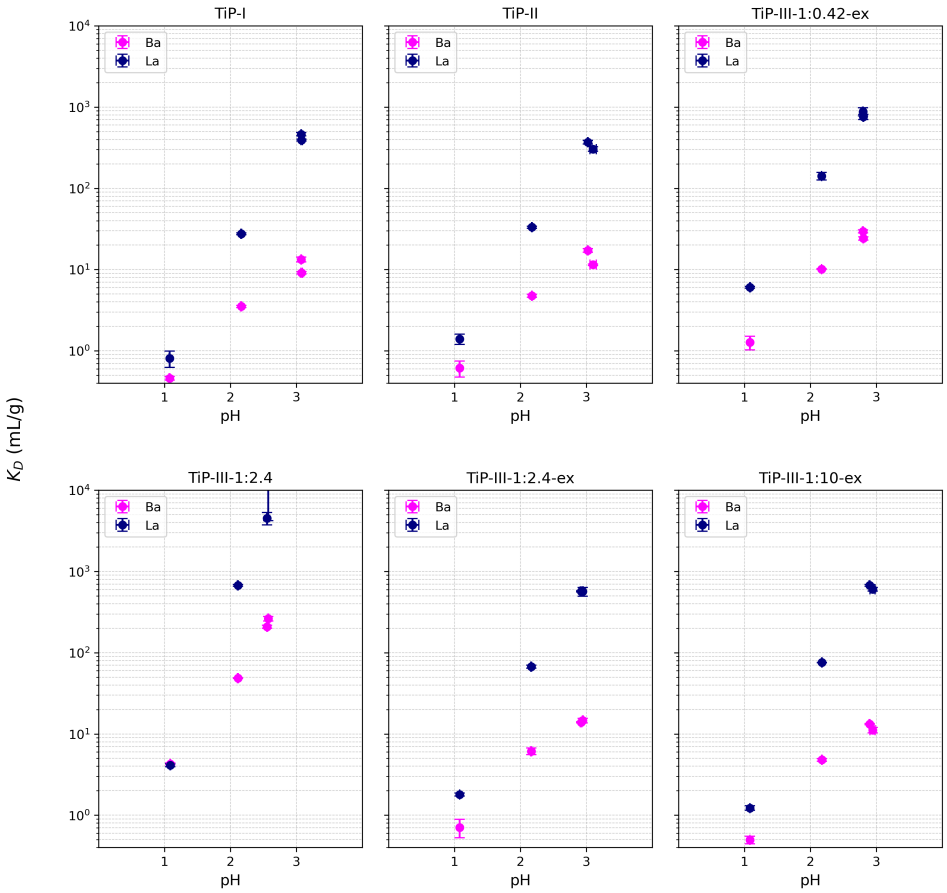

Figure C.2: Partition coefficients (K_D) of Ba^{2+} (C_0 = 1.5 mM) and La^{3+} (C_0 = 2.5 µM) for TiP materials at varying equilibrium pH values(batch tests, 0.05 g sorbent, 20 °C).

C.1. Adsorption experiment specifics

The sample codes in the tables below represent individual samples. The first element of the code indicates the experiment, the second element corresponds to the intended pH and the third element identifies the material used, as shown in Table C.1. The final element, X, Y or Z, distinguishes the triplicates.

Table C.1: Explanation of the third element of sample codes.

Code	Material
1	TiP-I
2	TiP-II
3	TiP-III-1:0.42-ex
4	TiP-III-1:2.4
5	TiP-III-1:2.4-ex
6	TiP-III-1:10-ex

Table C.2: Specifics of Experiment A.

Vial	Ads. Ba^{2+} [%]	Ads. La^{3+} [%]	K_D Ba [mL/g]	K_D La [mL/g]	Ex. time	Weight [g]	pH
A71X	32.05	95.16	9.53	397.33	03:50	0.04948	3.08
A71Y	31.62	95.04	9.14	378.73	03:50	0.05062	3.07
A71Z	30.51	95.28	8.75	402.05	03:50	0.05019	3.09
A72X	36.32	93.42	11.41	283.79	03:30	0.04999	3.08
A72Y	36.66	94.21	11.75	330.38	03:30	0.04923	3.16
A72Z	36.18	93.82	11.19	299.62	03:30	0.05067	3.07
A73X	55.24	97.64	24.69	828.71	03:30	0.05000	2.80
A73Y	55.78	97.44	25.15	760.26	03:30	0.05015	2.80
A73Z	53.05	97.20	22.58	693.25	03:30	0.05005	2.81
A74X	91.64	99.63	217.69	5381.94	03:10	0.05033	2.56
A74Y	90.69	99.42	196.21	3479.97	03:10	0.04967	2.55
A74Z	91.36	99.58	211.63	4736.66	03:10	0.04996	2.56
A75X	41.58	96.61	14.13	565.44	03:10	0.05037	2.93
A75Y	41.46	96.54	14.10	556.39	03:10	0.05022	2.91
A75Z	40.44	96.67	13.62	581.71	03:10	0.04985	2.92
A76X	40.12	97.18	13.34	685.78	03:10	0.05024	2.90
A76Y	39.44	97.04	12.90	650.19	03:10	0.05047	2.90
A76Z	39.83	97.18	13.33	693.41	03:10	0.04967	2.89
AS7X	-	-	-	-	-	-	5.68
AS7Y	-	-	-	-	-	-	5.73
AS7Z	-	-	-	-	-	-	5.73

Table C.3: Specifics of Experiment B.

Vial	Ads. Ba^{2+} [%]	Ads. La^{3+} [%]	K_D Ba [mL/g]	K_D La [mL/g]	Ex. time	Weight [g]	pH
B51X	41.99	95.74	14.41	448.02	05:00	0.05022	3.08
B51Y	40.39	96.16	13.42	496.54	05:00	0.05047	3.07
B51Z	37.92	95.73	12.18	447.03	05:00	0.05018	3.07
B52X	45.59	94.61	16.91	354.35	05:00	0.04955	3.03
B52Y	48.16	95.22	18.52	396.95	05:00	0.05016	3.02
B52Z	45.02	94.76	16.31	360.08	05:00	0.05019	3.02
B53X	58.05	98.02	27.95	1000.32	05:00	0.04952	2.80
B53Y	59.86	97.80	29.69	884.29	05:00	0.05023	2.79
B53Z	60.82	97.44	30.88	758.61	05:00	0.05027	2.80
B54X	92.96	99.85	266.58	13351.12	04:45	0.04950	2.57
B54Y	93.33	99.97	281.25	66144.67	04:45	0.04975	2.58
B54Z	92.22	99.80	239.24	10184.90	04:45	0.04955	2.57
B55X	42.66	95.99	14.95	481.93	04:45	0.04977	2.95
B55Y	40.15	96.60	13.40	567.54	04:45	0.05005	2.95
B55Z	43.78	97.02	15.59	650.92	04:45	0.04995	2.94
B56X	33.67	96.73	10.21	595.40	04:45	0.04973	2.96
B56Y	35.77	96.64	11.05	570.21	04:45	0.05040	2.97
B56Z	37.93	96.99	12.26	647.36	04:45	0.04986	2.90
BS5X	-	-	-	-	-	-	5.32
BS5Y	-	-	-	-	-	-	5.34
BS5Z	-	-	-	-	-	-	5.55

Table C.4: Specifics of Experiment C.

Vial	Ads. Ba^{2+} [%]	Ads. La^{3+} [%]	K_D Ba [mL/g]	K_D La [mL/g]	Ex. time	Weight [g]	pH
C31X	51.60	95.72	21.18	444.42	05:00	0.05033	2.81
C31Y	49.04	95.49	19.29	424.18	05:00	0.04990	2.83
C31Z	47.77	95.74	18.26	448.58	05:00	0.05010	2.83
C32X	54.80	94.75	24.05	357.76	05:00	0.05041	2.81
C32Y	54.19	95.10	23.89	391.75	05:00	0.04952	2.81
C32Z	55.32	95.01	24.79	381.03	05:00	0.04994	2.81
C33X	73.33	98.52	54.72	1320.98	05:00	0.05024	2.64
C33Y	76.20	98.87	63.74	1736.84	05:00	0.05022	2.66
C33Z	76.82	98.88	66.15	1768.43	05:00	0.05011	2.66
C34X	93.66	99.78	298.33	9039.01	04:45	0.04955	2.52
C34Y	-	-	-	-	-	-	-
C34Z	92.36	99.78	242.65	9228.31	04:45	0.04984	2.51
C35X	24.08	95.88	6.33	464.45	04:45	0.05010	2.75
C35Y	50.36	96.37	20.42	534.89	04:45	0.04969	2.76
C35Z	50.16	97.95	20.17	957.53	04:45	0.04974	2.75
C36X	-2.11	80.72	-13.64	84.19	04:45	0.04990	2.72
C36Y	-0.63	94.35	-7.66	332.53	04:45	0.05026	2.70
C36Z	-0.47	95.18	-6.42	394.65	04:45	0.05003	2.70
S3X	-	-	-	-	-	-	3.13
S3Y	-	-	-	-	-	-	3.12
S3Z	-	-	-	-	-	-	3.12

Table C.5: Specifics of Experiment D.

Vial	Ads. Ba^{2+} [%]	Ads. La^{3+} [%]	K_D Ba [mL/g]	K_D La [mL/g]	Ex. time	Weight [g]	pH
D11X	2.38	2.70	0.49	0.55	05:00	0.04997	1.08
D11Y	2.11	4.67	0.43	0.98	05:00	0.05014	1.08
D11Z	2.21	4.21	0.46	0.89	05:00	0.04953	1.07
D12X	3.88	5.53	0.80	1.16	05:00	0.05049	1.07
D12Y	2.39	6.51	0.49	1.39	05:00	0.05017	1.08
D12Z	2.64	7.54	0.55	1.65	05:00	0.04952	1.08
D13X	4.82	24.05	1.00	6.27	05:00	0.05053	1.08
D13Y	7.29	22.69	1.59	5.93	05:00	0.04952	1.09
D13Z	5.70	22.83	1.21	5.93	05:00	0.04988	1.08
D14X	16.98	17.82	4.10	4.35	04:50	0.04986	1.09
D14Y	18.01	16.39	4.39	3.92	04:50	0.05000	1.08
D14Z	17.97	17.05	4.34	4.08	04:50	0.05045	1.09
D15X	2.29	8.21	0.47	1.79	04:50	0.04986	1.08
D15Y	4.29	7.82	0.90	1.71	04:50	0.04952	1.08
D15Z	3.61	8.64	0.75	1.89	04:50	0.05000	1.08
D16X	2.73	5.41	0.56	1.15	04:50	0.04997	1.08
D16Y	2.09	5.59	0.43	1.20	04:50	0.04951	1.08
D16Z	2.44	6.28	0.50	1.33	04:50	0.05037	1.08
DS1X	-	-	-	-	-	-	1.08
DS1Y	-	-	-	-	-	-	1.08
DS1Z	-	-	-	-	-	-	1.08

Table C.6: Specifics of Experiment E.

Vial	Ads. Ba^{2+} [%]	Ads. La^{3+} [%]	K_D Ba [mL/g]	K_D La [mL/g]	Ex. time	Weight [g]	pH
E21X	15.39	58.01	3.67	27.84	05:05	0.04962	2.16
E21Y	14.68	57.17	3.42	26.54	05:05	0.05028	2.16
E21Z	14.72	58.74	3.44	28.39	05:05	0.05013	2.17
E22X	18.14	61.45	4.45	32.03	05:05	0.04976	2.18
E22Y	19.71	63.12	4.93	34.39	05:05	0.04977	2.17
E22Z	19.72	62.37	4.90	33.10	05:05	0.05008	2.17
E23X	33.18	86.28	10.00	126.66	05:05	0.04967	2.17
E23Y	29.50	86.54	10.25	157.54	05:05	0.04081	2.17
E23Z	-	-	-	-	-	-	-
E24X	70.68	97.22	48.36	702.20	04:45	0.04986	2.11
E24Y	70.78	97.06	48.46	660.29	04:45	0.04998	2.11
E24Z	70.79	97.04	48.95	661.94	04:45	0.04951	2.12
E25X	25.49	77.79	6.87	70.34	04:45	0.04981	2.16
E25Y	23.21	77.62	6.00	68.91	04:45	0.05034	2.17
E25Z	21.49	75.81	5.52	63.16	04:45	0.04961	2.16
E26X	19.11	79.27	4.70	76.01	04:45	0.05030	2.17
E26Y	20.39	79.20	5.07	75.39	04:45	0.05050	2.17
E26Z	18.82	79.16	4.64	75.99	04:45	0.05000	2.18
ES2X	-	-	-	-	-	-	2.21
ES2Y	-	-	-	-	-	-	2.22
ES2Z	-	-	-	-	-	-	2.22

Table C.7: Specifics of Experiment F.

Vial	Ads. Ba^{2+} [%]	Ads. La^{3+} [%]	Ex. time	Weight [g]	pH
F7X	36.67	95.66	00:30	0.04981	3.27
F7Y	37.11	95.83	00:30	0.05002	3.26
F7Z	36.63	95.80	00:30	0.05001	3.26
F7X	36.94	96.01	01:00	0.04982	3.24
F7Y	36.94	96.02	01:00	0.04990	3.29
F7Z	36.28	96.26	01:00	0.04993	3.25
F7X	37.81	96.26	01:30	0.05001	3.27
F7Y	37.97	96.09	01:30	0.04983	3.26
F7Z	37.69	96.42	01:30	0.04984	3.25
F7X	37.90	96.60	02:00	0.04983	3.25
F7Y	37.01	96.17	02:00	0.05024	3.24
F7Z	37.51	96.24	02:00	0.05001	3.25
F7X	39.07	96.44	03:00	0.05007	3.26
F7Y	39.42	96.51	03:00	0.05035	3.22
F7Z	38.53	96.64	03:00	0.05009	3.23
F7X	38.04	96.33	04:00	0.05020	3.23
F7Y	39.54	96.77	04:00	0.04984	3.21
F7Z	39.09	96.78	04:00	0.04964	3.21
F7X	39.97	97.03	06:00	0.04987	3.24
F7Y	39.48	97.13	06:00	0.04987	3.23
F7Z	39.11	96.85	06:00	0.04994	3.23
F7X	-	97.42	24:00	0.04995	-
F7Y	-	97.70	24:00	0.04995	-
F7Z	-	97.68	24:00	0.04996	-
F7X	-	97.07	48:00	0.05008	3.17
F7Y	-	97.11	48:00	0.04974	3.18
F7Z	-	97.48	48:00	0.05014	3.17

D
Multicomponent Langmuir fitting

D.1. Theoretical background Langmuir adsorption model

The Langmuir adsorption model offers a fundamental model for describing the adsorption of species onto a solid surface. It was developed to characterise gas adsorption on homogeneous surfaces, but its principles apply to ion exchange by treating the exchange sites on a sorbent as homogeneous with discrete locations where ions from a solution can bind reversibly. In the context of ion exchange, first, the theory assumes that a fixed and therefore finite number of identical exchange sites exist on the ion exchanger, each capable of binding one ion, leading to a monolayer coverage at saturation. Second, the exchange process is reversible, creating a dynamic equilibrium between adsorption and desorption. Third, the binding energy of the ions is constant across all sites and independent of coverage [35, 72, 114, 115].

These assumptions lead to the equation of the Langmuir isotherm (Equation D.1), which quantifies the fractional occupancy of exchange sites as a function of ion concentration in the solution:

$$\theta = \frac{q}{q_m} = \frac{K_{Lang} C_{eq}}{1 + K_{Lang} C_{eq}} \tag{D.1}$$

Where:

- θ is the fractional coverage,
- q is the amount of ion adsorbed [mol/g],
- q_m is the maximum adsorption capacity [mol/g],
- C_{eq} is the equilibrium ion concentration [mol/L],
- K_{Lang} is the Langmuir equilibrium constant [L/mol].

Unlike the Langmuir model, the Freundlich model describes adsorption on heterogeneous surfaces using a power-law relationship. Because it lacks a saturation limit, it is less suitable for systems with a finite number of exchange sites, such as ion exchange processes in this study [116]. The Brunauer-Emmett-Teller (BET) theory, extends the framework of Langmuir to multilayer adsorption, often applied in gas-solid systems, where molecules can stack beyond a monolayer. Such multilayer adsorption is less applicable to liquid-solid ion exchange systems, where site-specific binding dominates [117].

D.1.1. Multicomponent system

This study investigates a competitive multicomponent ion exchange system involving Ba^{2+}, La^{3+} and H^+ ions. Such systems deviate from the assumptions of the standard Langmuir model, which considers single-species adsorption and uniform binding energies. The competition for exchange sites introduces varying affinities driven by charge, ionic size and electrostatic interactions, violating the uniform binding energy assumption. To account for this, a generalised competitive Langmuir isotherm is presented in Equation D.2. This equation quantifies the fractional coverage of the ion of interest (M) as a function of the concentration of all species combined in a solution [72, 73]:

$$\theta_M = \frac{q_M}{q_m} = \frac{K_M C_M}{1 + K_{Ba} C_{Ba} + K_{La} C_{La} + K_H C_H} \tag{D.2}$$

Where:

- θ_M is the fractional coverage of the ion of interest M,
- q_M is the amount of ion M adsorbed [mol/g],
- q_m is the total site capacity [mol/g],
- C_{Ba}, C_{La} and C_H are the equilibrium concentrations of Ba^{2+}, La^{3+} and H^+ [mol/L],
- K_{Ba}, K_{La} and K_H are their specific respective equilibrium constants [L/mol],
- C_M is the equilibrium concentration of ion M [mol/L],
- K_M is the equilibrium constant of ion M [L/mol].

It is important to note that the model assumes independent site occupation, meaning it neglects interactions between adsorbed ions. Therefore, it does not account for cooperative effects such as interactions between ions or structural changes in the sorbent during exchange.

While thermodynamic modelling defines the thermodynamic equilibrium constant K_{thermo} in Equation 2.1 in terms of chemical activities, yielding a dimensionless quantity, the Langmuir binding constant K_{Lang} in Equation D.1, is based on concentrations and therefore carries units mol/L. This reflects the affinity of an ion for the surface of a sorbent. Similarly, K_M in Equation D.2 is the equilibrium constant for a specific ion M, like the K_{Lang}, but in a multi-component system, carrying the same units.

D.2. Multicomponent Langmuir fitting

The competitive Langmuir model was fitted to the experimental adsorption data by minimising the residuals between the measured and predicted adsorbed ions q_M for each species, using non-linear least squares optimisation. The input data were derived from both adsorption and surface saturation experiments. This fitting procedure yields four parameters, the affinity constants K_{La}, K_{Ba} and K_{H}, and the maximum sorption capacity q_m.

To reduce convergence on local minima and improve fit robustness, 100 initial guesses were employed for each material. Only parameter sets that yielded physically meaningful values (positive K_M and q_m values) were presented. The results are reported in Table D.2 and Table D.2.

A consistent trend across the fitted models was the convergence of q_m to approximately $1.0 \cdot 10^{-5}$ mol/g for TiP-I and $1.3 \cdot 10^{-5}$ mol/g for TiP-III-1:10-ex, with minor deviations observed. This convergence suggested that q_m is not a sensitive parameter in the model. The order of magnitude of the values was consistent with reported sorption capacities in literature for α-TiP [69] (4.89e-5 at pH 4.86 for 500 nm crystallites). Furthermore, the slightly bigger surface capacity for TiP-III-1:10-ex was consistent with the results of the adsorption experiments (Section 4.2).

In cases where deviations of q_m occurred (Run 63 for TiP-I and 42, 62, 84 for TiP-III-1:10-ex), the graphical interpretation of the parity plots indicates poor fitting, as could be observed for Run 63 of TiP-I (Figure D.1b) and Run 61 of TiP-III-1:10-ex (Figure D.1d). In contrast, fits such as Run 17 (Figure D.1a) and Run 79 (Figure D.1c) demonstrated accurate and consistent model behaviour.

Furthermore, in all fits that yielded positive K_M and q_m values, the affinity constant K_{La} was at least one order of magnitude higher than K_{Ba}, indicating a significantly higher preference of the sorbent for La^{3+} that Ba^{2+}. This was consistent with the thermodynamic behaviour (Section 4.3.2) and the results of the adsorption experiments (Section 4.2).

Although consistent trends were observed, no definitive conclusions can be drawn from the fitting due to the underdefined nature of the system. Additional data points with varying initial concentrations are required to add more constraints to the model and validate the reliability of the fitted parameters.

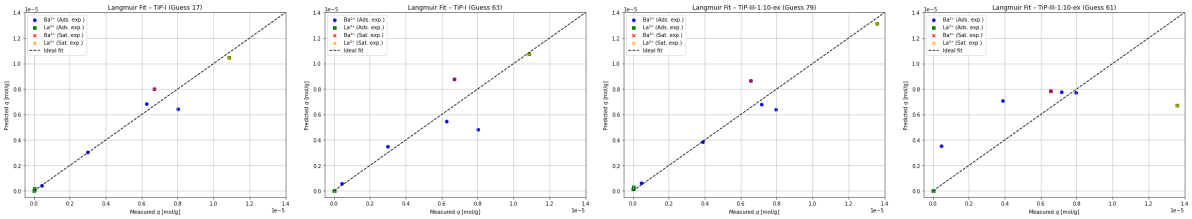

(a) Run 17, TiP-I **(b)** Run 63, TiP-I **(c)** Run 79, TiP-III-1:10-ex **(d)** Run 61, TiP-III-1:10-ex

Figure D.1: Parity plots of measured versus predicted adsorption capacities q_m for Ba^{2+} and La^{3+} on TiP-I and TiP-III-1:10-ex, using the competitive Langmuir model.

Table D.1: Initial guesses and fitted parameters from the competitive Langmuir model for TiP-I.

Run	$K_{\mathrm{Ba},\,0}$	$K_{\mathrm{La},\,0}$	$K_{\mathrm{H},\,0}$	$q_{m,0}$	K_{Ba}	K_{La}	K_{H}	q_m	R^2_{total}	R^2_{Ba}	R^2_{La}
1	1e2	1e8	1e3	1e-04	8.67e3	4.84e5	2.67e3	1.06e-05	0.9692	0.887	0.997
2	1e3	1e9	1e2	5e-05	7.54e3	3.62e5	2.26e3	1.06e-05	0.9693	0.886	0.998
3	1e4	1e7	1e5	5e-04	7.52e3	3.44e5	2.26e3	1.07e-05	0.9693	0.885	0.998
5	1e6	1e5	1e6	1e-05	5.83e4	2.17e6	2.21e4	1.04e-05	0.9672	0.882	0.996
7	1e8	1e3	1e4	1e-04	1.11e7	5.35e8	4.37e6	1.04e-05	0.9668	0.881	0.995
8	1e3	1e8	1e6	5e-05	3.11e6	1.43e8	1.23e6	1.04e-05	0.9668	0.881	0.996
9	1e4	1e9	1e2	5e-04	7.52e3	3.43e5	2.26e3	1.07e-05	0.9693	0.885	0.998
11	1e6	1e6	1e5	1e-05	2.42e4	1.58e6	8.69e3	1.04e-05	0.9679	0.885	0.996
12	1e7	1e5	1e1	2e-04	7.15e3	3.31e5	2.11e3	1.07e-05	0.9693	0.885	0.998
13	1e8	1e4	1e3	1e-04	6.63e3	2.38e5	1.95e3	1.07e-05	0.9691	0.884	0.998
14	1e2	1e9	1e6	5e-05	9.53e6	4.92e8	3.70e6	1.04e-05	0.9668	0.882	0.995
16	1e4	1e6	1e0	1e-03	7.58e3	3.75e5	2.27e3	1.06e-05	0.9693	0.886	0.998
17	1e5	1e5	1e5	1e-05	6.46e3	2.09e5	1.87e3	1.07e-05	0.9690	0.883	0.998
21	1e2	1e8	1e2	5e-04	8.42e3	4.28e5	2.59e3	1.06e-05	0.9693	0.886	0.997
23	1e4	1e7	1e5	1e-05	1.73e5	7.50e6	7.72e4	1.07e-05	0.9662	0.872	0.998
27	1e8	1e3	1e2	5e-04	9.36e2	3.62e3	4.19e2	1.92e-05	0.9373	0.757	0.999
29	1e3	1e8	1e5	1e-05	4.82e5	2.31e7	1.90e5	1.04e-05	0.9669	0.881	0.996
31	1e5	1e6	1e3	1e-04	9.80e3	5.70e5	3.10e3	1.05e-05	0.9691	0.887	0.997
34	1e8	1e3	1e0	1e-03	5.15e6	2.41e8	2.04e6	1.04e-05	0.9668	0.881	0.995
36	1e3	1e9	1e1	2e-04	7.56e3	3.64e5	2.27e3	1.06e-05	0.9693	0.886	0.998
38	1e5	1e6	1e6	5e-05	3.36e5	1.45e6	2.72e5	1.36e-05	0.9425	0.789	0.994
42	1e2	1e9	1e1	2e-04	7.50e3	3.42e5	2.25e3	1.07e-05	0.9693	0.885	0.998
43	1e3	1e8	1e3	1e-04	7.28e3	3.46e5	2.15e3	1.06e-05	0.9693	0.885	0.998
45	1e5	1e6	1e2	5e-04	7.26e3	3.37e5	2.15e3	1.07e-05	0.9693	0.885	0.998
48	1e8	1e3	1e1	2e-04	7.56e3	3.64e5	2.27e3	1.06e-05	0.9693	0.886	0.998
49	1e2	1e9	1e3	1e-04	7.57e3	3.75e5	2.27e3	1.06e-05	0.9693	0.886	0.998
50	1e3	1e8	1e6	5e-05	3.11e6	1.43e8	1.23e6	1.04e-05	0.9668	0.881	0.996
55	1e8	1e3	1e3	1e-04	5.30e3	1.07e5	1.52e3	1.10e-05	0.9680	0.878	0.999
56	1e2	1e9	1e6	5e-05	9.53e6	4.92e8	3.70e6	1.04e-05	0.9668	0.882	0.995
61	1e7	1e4	1e3	1e-04	4.03e3	4.62e4	1.17e3	1.15e-05	0.9655	0.868	0.999
63	1e2	1e9	1e2	5e-04	1.41e2	4.54e2	1.93e2	7.12e-05	0.8958	0.592	1.000
64	1e3	1e8	1e0	1e-03	9.57e4	4.90e6	3.68e4	1.04e-05	0.9672	0.882	0.995
65	1e4	1e7	1e5	1e-05	1.73e5	7.50e6	7.72e4	1.07e-05	0.9662	0.872	0.998
69	1e8	1e3	1e2	5e-04	9.36e2	3.62e3	4.19e2	1.92e-05	0.9373	0.757	0.999

71	1e3	1e8	1e5	1e-05	4.82e5	2.31e7	1.90e5	1.04e-05	0.9669	0.881	0.996	
73	1e5	1e6	1e3	1e-04	9.80e3	5.70e5	3.10e3	1.05e-05	0.9691	0.887	0.997	
76	1e8	1e3	1e0	1e-03	5.15e6	2.41e8	2.04e6	1.04e-05	0.9668	0.881	0.995	
77	1e2	1e9	1e5	1e-05	8.59e3	3.10e5	2.66e3	1.06e-05	0.9691	0.885	0.997	
78	1e3	1e8	1e1	2e-04	1.60e4	1.15e6	5.38e3	1.04e-05	0.9683	0.888	0.995	
80	1e5	1e6	1e6	5e-05	3.36e5	1.45e6	2.72e5	1.36e-05	0.9425	0.789	0.994	
84	1e2	1e9	1e1	2e-04	7.50e3	3.42e5	2.25e3	1.07e-05	0.9693	0.885	0.998	
85	1e3	1e8	1e3	1e-04	7.28e3	3.46e5	2.15e3	1.06e-05	0.9693	0.885	0.998	
87	1e5	1e6	1e2	5e-04	7.26e3	3.37e5	2.15e3	1.07e-05	0.9693	0.885	0.998	
90	1e8	1e3	1e1	2e-04	7.56e3	3.64e5	2.27e3	1.06e-05	0.9693	0.886	0.998	
91	1e2	1e9	1e3	1e-04	7.57e3	3.75e5	2.27e3	1.06e-05	0.9693	0.886	0.998	
92	1e3	1e8	1e6	5e-05	3.11e6	1.43e8	1.23e6	1.04e-05	0.9668	0.881	0.996	
97	1e8	1e3	1e3	1e-04	5.30e3	1.07e5	1.52e3	1.10e-05	0.9680	0.878	0.999	
98	1e2	1e9	1e6	5e-05	9.53e6	4.92e8	3.70e6	1.04e-05	0.9668	0.882	0.995	

Table D.2: Initial guesses and fitted parameters from the competitive Langmuir model for TiP-III-1:10-ex.

Run	$K_{\mathrm{Ba},\,0}$	$K_{\mathrm{La},\,0}$	$K_{\mathrm{H},\,0}$	$q_{m,0}$	K_{Ba}	K_{La}	K_{H}	q_m	R^2_{total}	R^2_{Ba}	R^2_{La}
1	1e2	1e8	1e3	1e-04	5.65e3	8.57e5	1.84e3	1.31e-05	0.9598	0.804	0.995
2	1e3	1e9	1e2	5e-05	1.47e3	2.14e4	3.31e2	1.59e-05	0.9533	0.754	0.999
3	1e4	1e7	1e5	5e-04	2.87e3	2.62e5	7.04e2	1.34e-05	0.9628	0.809	0.998
5	1e6	1e5	1e6	1e-05	6.73e5	1.97e6	4.32e5	1.72e-05	0.8272	0.533	0.884
11	1e6	1e6	1e5	1e-05	4.05e4	1.50e6	1.54e4	1.28e-05	0.9504	0.778	0.989
14	1e2	1e9	1e6	5e-05	6.43e6	7.66e8	2.92e6	1.30e-05	0.9536	0.769	0.996
16	1e4	1e6	1e0	1e-03	4.82e3	9.46e5	1.50e3	1.31e-05	0.9598	0.807	0.994
17	1e5	1e5	1e5	1e-05	2.83e3	2.49e5	6.88e2	1.34e-05	0.9628	0.809	0.998
20	1e8	1e2	1e6	5e-05	4.80e6	5.36e8	2.18e6	1.30e-05	0.9535	0.769	0.996
23	1e4	1e7	1e5	1e-05	5.60e4	7.23e6	2.46e4	1.30e-05	0.9543	0.773	0.995
29	1e3	1e8	1e5	1e-05	2.11e5	2.49e7	9.47e4	1.30e-05	0.9537	0.770	0.996
33	1e7	1e4	1e2	5e-04	2.12e3	9.70e4	4.01e2	1.37e-05	0.9605	0.795	0.998
35	1e2	1e8	1e5	1e-05	3.86e5	5.00e7	1.74e5	1.30e-05	0.9536	0.770	0.995
36	1e3	1e9	1e1	2e-04	2.86e3	2.72e5	7.00e2	1.34e-05	0.9628	0.810	0.998
37	1e4	1e7	1e3	1e-04	2.85e3	2.57e5	6.98e2	1.34e-05	0.9628	0.809	0.998
38	1e5	1e6	1e6	5e-05	6.79e4	1.53e6	3.24e4	1.36e-05	0.9482	0.748	0.994
40	1e7	1e4	1e0	1e-03	4.00e5	4.89e7	1.80e5	1.30e-05	0.9536	0.770	0.995
41	1e8	1e3	1e5	1e-05	1.15e7	4.09e8	5.49e6	1.34e-05	0.9507	0.755	0.995
42	1e2	1e9	1e1	2e-04	5.22e2	3.61e3	2.13e2	2.77e-05	0.9281	0.617	1.000
45	1e5	1e6	1e2	5e-04	4.79e3	9.27e5	1.48e3	1.31e-05	0.9599	0.808	0.994
48	1e8	1e3	1e1	2e-04	2.87e3	2.63e5	7.05e2	1.34e-05	0.9628	0.809	0.998
49	1e2	1e9	1e3	1e-04	2.82e3	2.49e5	6.88e2	1.34e-05	0.9628	0.809	0.998
56	1e2	1e9	1e6	5e-05	6.43e6	7.66e8	2.92e6	1.30e-05	0.9536	0.769	0.996
59	1e5	1e6	1e5	1e-05	4.88e3	9.50e5	1.52e3	1.31e-05	0.9598	0.807	0.994
61	1e7	1e4	1e3	1e-04	3.88e7	1.17e7	5.78e5	7.95e-06	0.6559	0.424	0.679
62	1e8	1e3	1e6	5e-05	5.20e6	5.74e8	2.36e6	1.30e-05	0.9535	0.769	0.996
63	1e2	1e9	1e2	5e-04	2.85e3	2.59e5	6.97e2	1.34e-05	0.9628	0.809	0.998
64	1e3	1e8	1e0	1e-03	5.91e4	7.60e6	2.59e4	1.30e-05	0.9542	0.773	0.995
65	1e4	1e7	1e5	1e-05	5.60e4	7.23e6	2.46e4	1.30e-05	0.9543	0.773	0.995
71	1e3	1e8	1e5	1e-05	2.11e5	2.49e7	9.47e4	1.30e-05	0.9537	0.770	0.996
75	1e7	1e4	1e2	5e-04	2.12e3	9.70e4	4.01e2	1.37e-05	0.9605	0.795	0.998
77	1e2	1e9	1e5	1e-05	1.03e6	1.25e8	4.68e5	1.30e-05	0.9536	0.770	0.995
78	1e3	1e8	1e1	2e-04	2.11e4	2.84e6	8.74e3	1.30e-05	0.9555	0.780	0.995
79	1e4	1e7	1e3	1e-04	2.85e3	2.57e5	6.98e2	1.34e-05	0.9628	0.809	0.998

80	1e5	1e6	1e6	5e-05	6.79e4	1.53e6	3.24e4	1.36e-05	0.9482	0.748	0.994
82	1e7	1e4	1e0	1e-03	4.00e5	4.89e7	1.80e5	1.30e-05	0.9536	0.770	0.995
83	1e8	1e3	1e5	1e-05	1.15e7	4.09e8	5.49e6	1.34e-05	0.9507	0.755	0.995
84	1e2	1e9	1e1	2e-04	5.22e2	3.61e3	2.13e2	2.77e-05	0.9281	0.617	1.000
87	1e5	1e6	1e2	5e-04	4.79e3	9.27e5	1.48e3	1.31e-05	0.9599	0.808	0.994
90	1e8	1e3	1e1	2e-04	2.87e3	2.63e5	7.05e2	1.34e-05	0.9628	0.809	0.998
91	1e2	1e9	1e3	1e-04	2.82e3	2.49e5	6.88e2	1.34e-05	0.9628	0.809	0.998
98	1e2	1e9	1e6	5e-05	6.43e6	7.66e8	2.92e6	1.30e-05	0.9536	0.769	0.996